PROTON CONDUCTING CERATE CERAMICS

G. W. Coffey, L. R. Pederson, T. R. Armstrong, J. L. Bates and W. J. Weber

Pacific Northwest Laboratory[1]
P. O. Box 999
Richland, Washington 99352 USA

ABSTRACT

Cerate perovskites of the general formula $AM_xCe_{1-x}O_{3-\delta}$, where A = Sr or Ba and where M = Gd, Nd, Y, Yb or other rare earth dopant, are known to conduct a protonic current. Such materials may be useful as the electrolyte in a solid oxide fuel cell operating at intermediate temperatures, as an electrochemical hydrogen separation membrane, or as a hydrogen sensor. Conduction mechanisms in these materials were evaluated using dc cyclic voltammetry and mass spectrometry, allowing currents and activation energies for proton, electron, and oxygen ion contributions to the total current to be determined. For $SrYb_{0.05}Ce_{0.95}O_{3-\delta}$, one of the best and most environmentally stable compositions, proton conduction followed two different mechanisms: a low temperature process, characterized by an activation energy of 0.42±0.04 eV, and a high temperature process, characterized by an activation energy of 1.38±0.13 eV. It is believed that the low temperature process is dominated by grain boundary conduction while bulk conduction is responsible for the high temperature process. The activation energy for oxygen ion conduction (0.97±0.10 eV) agrees well with other oxygen conductors, while that for electronic conduction, 0.90±0.09 eV, is affected by a temperature-dependent electron carrier concentration. Evaluated by direct measurement of mass flux through a dense ceramic with an applied dc field, oxygen ions were determined to be the majority charge carrier except at the lowest temperatures, followed by electrons and then protons.

INTRODUCTION

Certain perovskite-type oxides are known to conduct a protonic current through a fully densified structure.[1-3] The best proton-conducting oxides, ytterbium-doped strontium cerate and neodymium-doped barium cerate, have proton conductivities of approximately 0.01 S/cm at 800°C. These compositions are potentially useful as solid electrolytes in solid oxide fuel cells, as hydrogen sensors, as hydrogen pumps, and as steam electrolyzers to produce hydrogen from water.[3, 4]

Because these perovskite-type metal oxides often contain several types of point defects, they support conduction by multiple charge carriers.[2] At low temperatures, proton

---

[1]Operated by Battelle Memorial Institute for the U. S. Department of Energy under Contract DE-AC06-76RLO 1830.

hopping between oxide ions is believed to be the dominant conduction mechanism,[3] whereas electronic and oxygen ion contributions to the overall current become important at high temperatures.[5] Conduction mechanisms are not well established in these materials, partially the result of a practical difficulty in achieving electrolytes without interconnected porosity. For example, it has been proposed that hydrogen is carried by negatively charged hydroxyl ions rather than by protons.[6] A good understanding of the relative importance of each charge carrier is essential if these materials are to be utilized in a practical device.

EXPERIMENTAL PROCEDURES

Homogeneous $AM_xCe_{1-x}O_{3-\delta}$ powders, where A = Sr or Ba and where M = Gd, Nd, or Yb, were prepared by calcination of combustion-derived precursors.[7,8] This material was then calcined at temperatures <950°C for several hours and uniaxially and isostatically pressed into discs and bars. Most compositions sintered to greater than 98% of full density at 1500°C for 12 hours.

Discs of $AM_xCe_{1-x}O_{3-\delta}$, 2 to 3 mm thick and approximately 25 mm in diameter, were sealed in an alumina cell with gold gaskets. Porous platinum electrodes were previously applied to each surface. The seals were verified to be helium leak-tight using quadrupole mass spectrometry. Pt-Pt,10%Rh thermocouples provided local temperature measurements on each side of the samples as well as electrical leads for cyclic voltammetry and emf measurements. Cyclic voltammetry measurements were performed on these concentration cells, with either hydrogen, oxygen, or nitrogen gas flows on the source side of the cell and either nitrogen or oxygen flows on the collection side of the electrolyte. Gas fluxes (hydrogen, oxygen, or water) were monitored by mass spectrometry, using a stainless steel capillary tube to sample the gas stream. Oxygen fluxes were additionally determined using zirconia oxygen sensors.

RESULTS AND DISCUSSION

Cyclic voltammetry measurements performed with different choices of gas streams on each side of cerate perovskite sample in an electrochemical concentration cell allowed an estimate of currents carried by electrons, protons, and oxygen ions to be made over a range of temperatures. Simultaneous mass spectrometry measurements provided an independent

means to determine mass fluxes through the sample as a function of applied voltage, temperature, and environment, in a configuration very similar to that required in a solid oxide fuel cell, electrochemical hydrogen separation membrane, or related device. In general, the agreement between mass fluxes determined by mass spectrometry and those calculated from current/voltage responses was very good.

Electron contributions to conduction in the cerate perovskites were calculated from the slope of current versus voltage responses when nitrogen streams were applied to both sides of the sample. For $SrYb_{0.05}Ce_{0.95}O_{3-\delta}$, linear responses were obtained in the voltage range of ±0.5 volts in at 900°C, as shown in Figure 1. Water electrolysis was apparent outside that voltage range at the highest temperatures, leading to transport of hydrogen or oxygen ions in addition to the electronic current, depending on the sign of the voltage. Concurrent fluxes of hydrogen or oxygen were observed by mass spectrometry. The presence of water is essential for these perovskites to conduct a protonic current. Water will react with oxygen vacancies to create protonic carrier sites; the exact nature of the lattice defect is not well understood.[1-4]

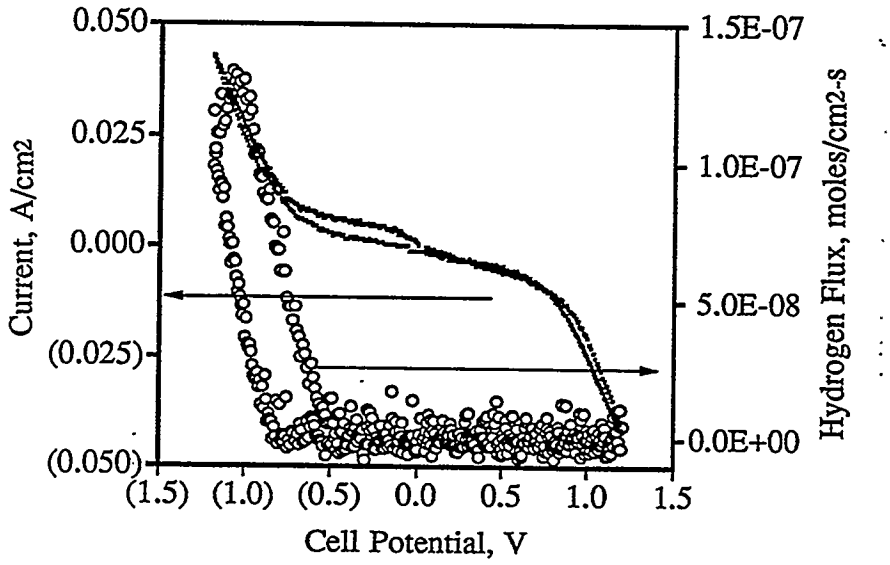

Figure 1. Cyclic voltammogram for $SrYb_{0.05}Ce_{0.95}O_{3-\delta}$ at 900°C for wet nitrogen versus nitrogen. Water electrolysis was apparent for -0.5V>cell potential>0.5V.

Proton currents were determined from current/voltage responses where a stream of 4% hydrogen in argon was applied on one side of the ceramic and a nitrogen stream was applied to the other side. Similarly, oxygen currents were determined using an air stream on one side and nitrogen on the other. Results for 4% hydrogen versus nitrogen and for air versus nitrogen are given in Figures 2 and 3, respectively. Electronic currents were subtracted from the overall current versus voltage curves in both cases. Asymmetric responses were obtained, as expected. Higher currents were found when a negative dc bias (collection side relative to the source side of the electrolyte) was applied with hydrogen on the source side; a positive dc bias gave higher currents with oxygen on the source side. This behavior is as expected for protonic and oxygen ion currents in addition to an electron current. With 4% hydrogen on the source side and air on the opposite side, the cerate supported proton, oxygen ion, and electron currents simultaneously. This arrangement is similar to that used in a solid oxide fuel cell.[10]

Activation energies were calculated for electron, oxygen ion, and proton transport as a function of temperature from cyclic voltammetry and mass spectrometry data. These results are given in Figures 4 and 5 for oxygen ion and proton transport, respectively. The activation energy for electronic transport was found to be 0.90±0.09 eV. From electron hole transport in $BaSm_{0.1}Ce_{0.9}O_{3-\delta}$ reported by Iwahara et al.,[4] an apparent activation energy of 1.1 eV can be calculated, similar to present results. Such higher than expected activation energies for electronic conduction probably reflect the creation of additional carriers (Ce^{4+}/Ce^{3+} equilibrium) with increased temperature as well as increased mobility. The activation energy for oxygen ion conduction was found to be 0.97±0.10 eV, in good agreement with results for cerates[4] and other oxygen conductors such as yttria-stabilized zirconia.[11] Currents calculated from oxygen fluxes determined by mass spectrometry were in good agreement with those determined from current/voltage curves. Activation energies for oxygen ion conduction determined from the two methods likewise were in good agreement.

Results for hydrogen conduction (see Figure 5) show two different regimes. At low temperatures (300 to 600°C), an activation energy of 0.42±0.04 eV was obtained from current/voltage responses, whereas at higher temperatures (600 to 900°C), an activation energy of 1.38±0.13 eV was found. Hydrogen fluxes determined by mass spectrometry were in fairly good agreement with those calculated from current/voltage curves. It is believed that proton currents at low temperatures are dominated by grain boundaries, while

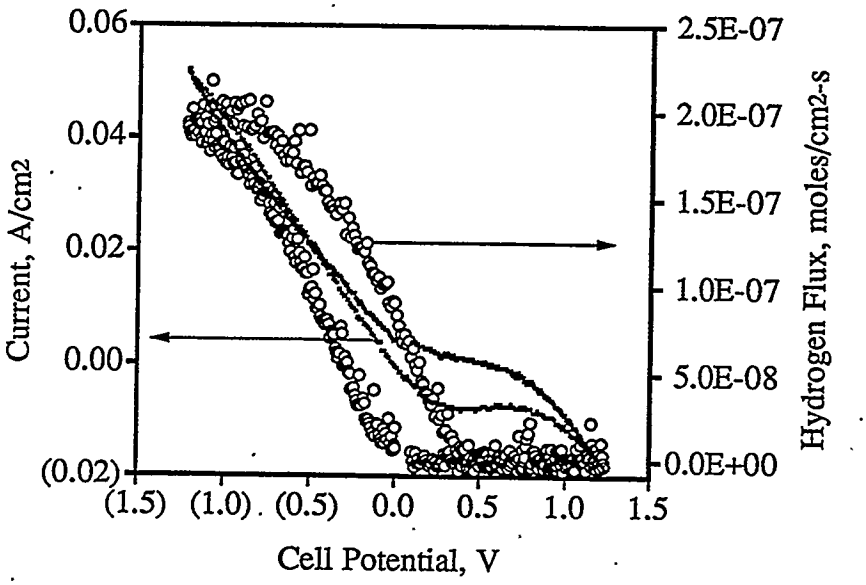

Figure 2. Cyclic voltammogram for $SrYb_{0.05}Ce_{0.95}O_{3-\delta}$ at 900°C for 4% hydrogen in argon versus nitrogen. Cathodic potentials led to hydrogen transport through the electrolyte.

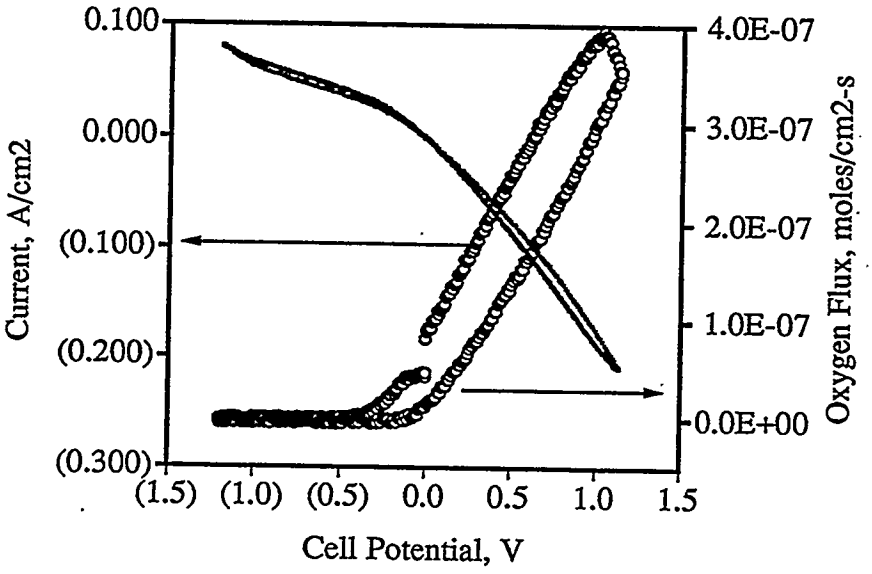

Figure 3. Cyclic voltammogram for $SrYb_{0.05}Ce_{0.95}O_{3-\delta}$ at 900°C for wet air versus nitrogen. Anodic potentials led to oxygen transport throught the electrolyte.

those at high temperatures are due to bulk conduction. A grain boundary component in proton currents in barium cerate compositions has been previously reported, attributed to a separate grain boundary phase.[12] In the strontium ytterbium cerates, however, no microscopic evidence for a grain boundary phase or segregation could be found.

From the ion and electron currents determined by cyclic voltammetry and mass transport (Figures 4 and 5), transference numbers for each charge-conducting species can be determined, as shown in Figure 6 for $SrYb_{0.05}Ce_{0.95}O_{3-\delta}$. The protonic contribution was the least important of the three, falling at first with increasing temperature to approximately 500°C (grain boundary contribution) and then rising with temperature (bulk contribution). For temperatures at which a practical electrochemical device could be operated, oxygen ions clearly were the most important charge carrier.

The kinetics of water uptake by $SrYb_{0.05}Ce_{0.95}O_{3-\delta}$ was evaluated by thermogravimetry and found to follow a two-stage process. The first, rapid uptake stage is attributed to hydration of the grain boundaries and near surface regions, whereas the much slower, long-term hydration is attributed to hydration of the bulk grains. Below approximately 700°C, times required to reach full hydration any of the bulk cerates were prohibitively long (>days). In previous studies of water uptake by similar compositions, complete hydration of the bulk was reported to be reached within a few hours even for temperatures below 600°C.[9] To fully remove water from the sample following each hydration experiment in the present study, it was necessary to heat to 1300°C in dry, flowing air for at least 24 hours. Activation energies were determined for both stages of water uptake by the perovskite. For the early stage of water uptake, which is attributed to grain boundary and near surface hydration, an activation energy of 0.39±0.09 eV was found. The second stage of hydration yielded a much higher activation energy: 2.8±0.4 eV, which is attributed to bulk hydration. Clearly, two substantially different processes contribute to the overall hydration of this material.

Environmental stability, in particular the reaction of strontium or barium cerates to form strontium or barium carbonate, may ultimately limit the applicability of these unique materials in fuel cells and other such devices. Barium cerates are particularly susceptible to decomposition to barium carbonate plus metal oxides and hydroxides. Sintered barium cerate samples will revert to a powder when exposed to the ambient atmosphere for a few days; strontium cerates, however, appear stable. From thermodynamic considerations,

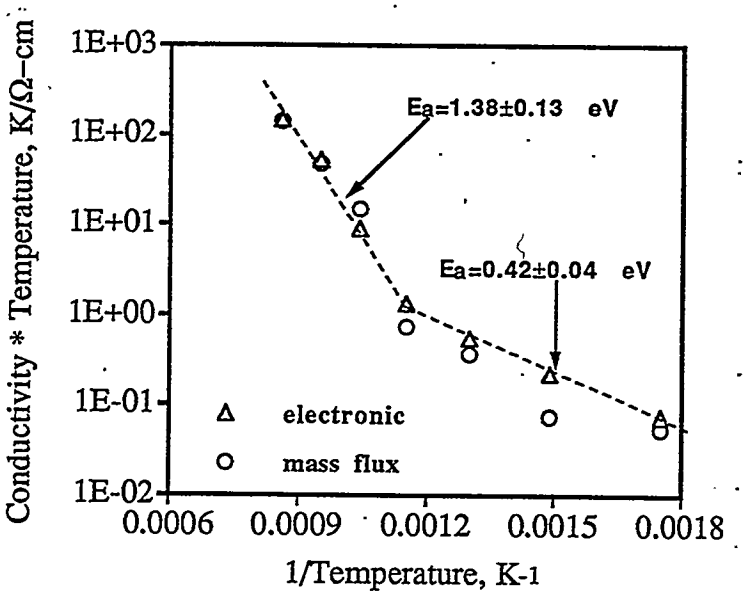

Figure 4. Proton conductivity-temperature product versus reciprocal temperature for $SrYb_{0.05}Ce_{0.95}O_{3-\delta}$. Low temperature conduction is dominated by grain boundary processes, while bulk processes are responsible for high temperature proton conduction.

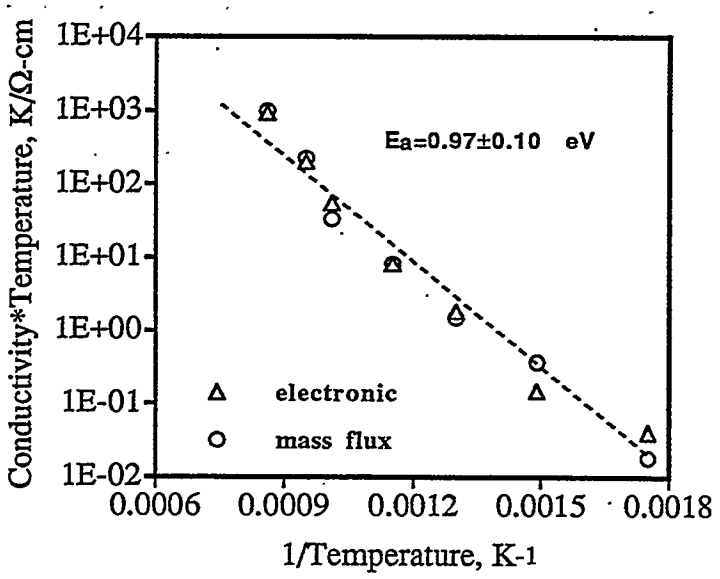

Figure 5. Oxygen ion conductivity-temperature product versus reciprocal temperature for $SrYb_{0.05}Ce_{0.95}O_{3-\delta}$.

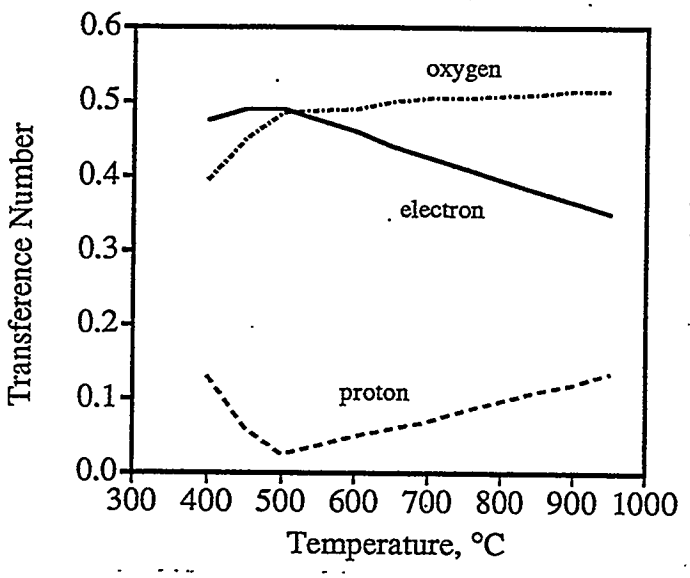

Figure 6. Transference numbers for protons, oxygen ions, and electrons in $SrYb_{0.05}Ce_{0.95}O_{3-\delta}$ as a function of temperature.

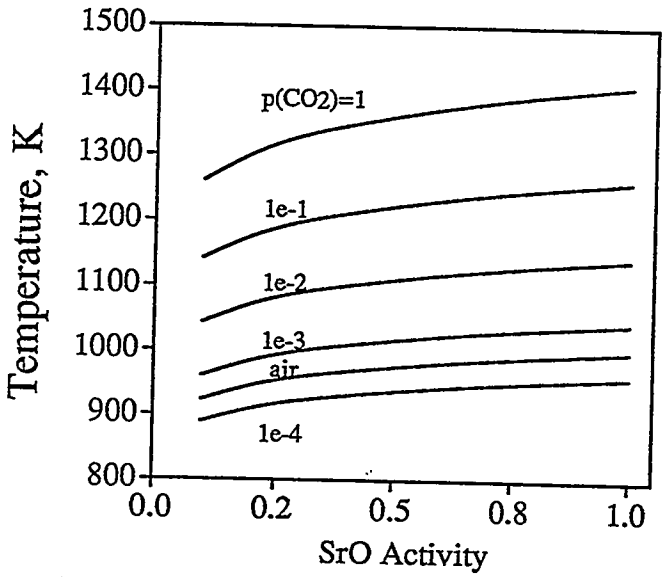

Figure 7. Calculated maximum temperature of stability of strontium carbonate as a function of SrO activity for several carbon dioxide partial pressures.

alkaline earth carbonates are expected to be stable to relatively high temperatures, as shown for strontium carbonate in Figure 6 for various carbon dioxide partial pressures. Assuming a(SrO)=0.5 (equal to its mole fraction in the cerate), strontium carbonate formation is expected in pure carbon dioxide up to approximately 1050°C. In air, strontium carbonate should decompose above ≈700°C. Barium carbonate is more stable than strontium carbonate, and should persist to even higher temperatures. Although predicted from thermodynamic data, carbonate formation in a pure carbon dioxide environment has not been observed to date above 800°C for either the strontium or barium cerates.

SUMMARY

Contributions to electrical conductivity in substituted cerate perovskites have been evaluated by cyclic voltammetry and mass transport, under conditions similar to those required for a practical electrochemical device. Measurements were facilitated by the development of synthesis and sintering methodologies to prepare fully dense ceramics, free of interconnected porosity. Protonic conduction followed two different mechanisms: a low temperature, grain boundary process having a small activation energy, and a high temperature, bulk process having a relatively high activation energy. Oxygen was the primary charge carrier over temperatures at which a practical electrochemical device could operate. Conductivities in the cerate perovskites were sufficiently high to be useful as the electrolyte in a fuel cell operating at intermediate temperatures, despite the fact that an electronic contribution to the overall current was apparent, which would lessen the efficiency of the fuel cell.

ACKNOWLEDGEMENTS

The authors gratefully acknowledge R. W. Stephens for technical assistance in performing transport measurements, D. E. McCready for performing x-ray diffraction analyses, N. T. Saenz for preparing specimens for microscopy, and J. E. Coleman for SEM analyses. Research was supported by the Advanced Research and Technology Development Materials Program, Office of Fossil Energy, U. S. Department of Energy.

REFERENCES

1. T. Norby, Solid State Ionics 40/41, p. 857 (1990).

2. N. Bonanos, Solid State Ionics 53-56, p. 967 (1992).

3. H. Iwahara, Solid State Ionics 28-30, p. 573 (1988).

4. H. Iwahara, T. Yajima, T. Hibino, and H. Ushida, J. Electrochem. Soc. 140 [6], p. 1687 (1993).

5. T. Yajima, H. Iwahara, and H. Uchida, Solid State Ionics 47, p. 117 (1991).

6. R. L. Cook and A. F. Sammells, Solid State Ionics 45, p. 311 (1991).

7. L. A. Chick, L. R. Pederson, G. D. Maupin, J. L. Bates, L. E. Thomas, and G. J. Exarhos, Materials Letters 10, p. 6 (1990).

8. T. R. Armstrong, J. L. Bates, G. W. Coffey, J. J. Kingsley, L. R. Pederson, J. W. Stevenson, W. J. Weber, and G. E. Youngblood, Proc. 8th Annual Conf. on Fossil Energy Materials, CONF-9405143, Oak Ridge National Laboratory, Oak Ridge, Tennessee, p. 89 (1994).

9. H. Iwahara, Solid State Ionics 52, p. 99 (1992).

10. H. Iwahara, T. Yajima, T. Hibino, and H. Ushida, J. Electrochem. Soc. 140 [6], p. 1687 (1993).

11. H. L. Tuller, in Ceramic Materials for Electronics, ed. R. C. Buchanon, Marcel Dekker, New York p. 425 (1986).

12. K. D. Kreuer, E. Schonherr, and J. Maier, Proc. 14th Int. Symp. Materials Science, eds. F. W. Poulson, J. J. Bentzen, T. Jacobsen, E. Skou, and M. L. J. Ostergard, Riso National Laboratory, Roskilde, Denmark p. 297 (1993).

SYNTHESIS OF SILICON NITRIDE POWDERS IN PULSED RF PLASMAS

R. J. Buss, S. V. Babu* and P. Ho

Sandia National Laboratories
Albuquerque, NM 87185-0367

ABSTRACT

Nanometer size silicon nitride particles are synthesized using a pulsed radio frequency plasma technique. The plasma is modulated with a square-wave on/off cycle of varying period to control size and morphology and to deduce the growth kinetics. *In situ* laser light scattering and *ex situ* particle analysis are used to study the nucleation and growth. For SiH_4/Ar plasmas which nucleate silicon particles, an extremely rapid initial growth phase is followed by a slower growth rate, approaching the rate of thin film deposition on adjacent flat surfaces. In SiH_4/NH_3 plasmas, silicon nitride particle size can be tightly controlled by adjusting the plasma-on time. The size dispersion of the particles is large and is consistent with a process of continual nucleation during the plasma-on period. Our observed polydispersity differs dramatically from that reported from other laboratories.

INTRODUCTION

It has been recognized for many years that silicon nitride has excellent high temperature structural properties such as high strength and low weight which would make it ideal for many applications such as engine parts. Unfortunately, the low temperature properties of hardness and brittleness make manufacturing processes difficult. It is known that materials formed from nanometer size subunits can exhibit improved macroscopic properties such as enhanced ductility or superplasticity. Also, in order to obtain the optimum properties, it is important to achieve microstructural and chemical homogeneity with minimal defects in a nearly fully dense ceramic. This is facilitated by starting with fine-particle-size powders that have low impurity content.

* Dept. of Chemical Engineering, Clarkson University, Potsdam, New York

Obtaining the ultrafine powders that are needed for exploratory research as well as manufacture has proven to be a problem. A variety of techniques are currently used to produce commercial silicon nitride powders[1]. These include direct nitridation of silicon, carbothermic reduction of silica and gas-phase reaction of $SiCl_4$ and NH_3. Several other gas-phase processes have been reported including the thermal pyrolysis of silane and ammonia[2] and laser pyrolysis of gaseous reactants[3]. Each of these processes has limitations in the morphology, size distribution, and chemical purity of the product.

In 1988, Buss and Ho patented a process[4] for synthesizing ultrafine particles of silicon nitride and other materials in a radio frequency (rf) plasma. The method involves flowing gaseous precursors at low pressure through a glow discharge. Electron-molecule collisions in the plasma result in fragmentation of the starting gases into reactive free radicals which undergo complex gas-phase chemistry leading to particle nucleation. Particles leaving the plasma are collected by filtering the gases pumped from the reactor. The technique is capable of generating gram quantities of silicon nitride powder in a few hours of operation in a laboratory reactor. Properties of the powder were well characterized by a variety of techniques[5].

During the past decade, particle formation and transport in plasmas has become an area of intense interest and activity[6]. It has developed that these particles, occurring in the plasmas used to manufacture microelectronic devices, can result in serious loss of wafer yield. Stimulated by this economic urgency, many laboratories worldwide have begun investigating the mechanisms governing particle nucleation, growth, trapping and agglomeration.

One particularly important achievement was reported by Boufendi and coworkers[7] in France in 1992. They studied formation of silicon particles in a silane/argon plasma by pulsing the plasma on for a short time and collecting the particles for electron microscopy. Remarkably, they found a linear rate of particle growth to the 40 nm size with a very narrow size dispersion. They postulated an initial stage of the plasma in which nucleation occurs, producing a high density of 5 nm size

particles followed by a no-nucleation stage in which these smaller particulates associated into the observed clusters.

We report here experiments aimed at applying this pulsed plasma approach to the synthesis of nano-size silicon nitride powders. Part of the work entails reproducing experiments of the French group with silane/argon to confirm the technique. Some striking differences in particle growth rates and size dispersion are reported. Applying the pulsed plasma technique to the silicon nitride system, we have demonstrated control of average particle size but with persistent size dispersion and agglomeration.

EXPERIMENTAL

A diagram of the apparatus is shown in Fig. 1. The plasma

Figure 1

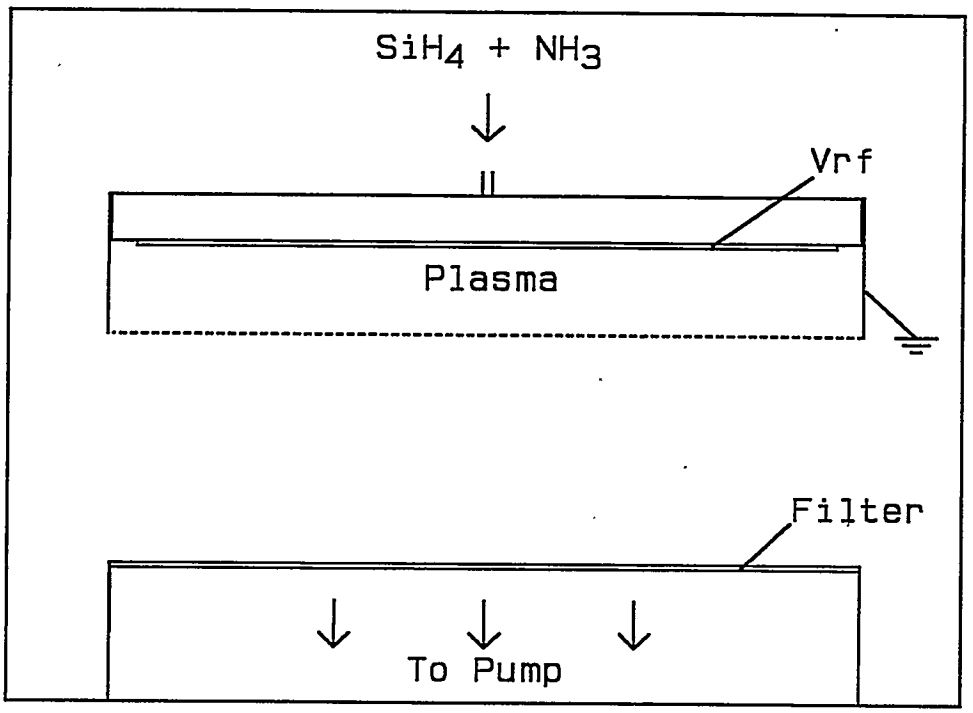

Fig. 1. Diagram of pulsed rf plasma apparatus.

electrode assembly consists of a 15 cm diameter powered electrode, perforated with holes to allow gas flow in a showerhead configuration. The plasma region is enclosed by a grounded aluminum sheet with a grounded high transmission screen across the bottom. The pumping port is located 4 cm beneath the electrode assembly, and is fitted with a single sheet of Whatman #1 filter paper. In order to study the size and morphology of the particles generated, transmission electron microscopy (TEM) was employed *ex situ*. To obtain samples, a TEM sample grid was placed beneath the plasma assembly on the filter paper.

A 10 mWatt helium-neon laser passed through the region beneath the plasma (or through holes in the electrode assembly wall). Laser light scattering from particles was observed by eye as a qualitative characterization of the process.

In a typical experiment, gas flow was first established (eg. 2 sccm SiH_4, 12 sccm NH_3, at 200 mTorr pressure); then the plasma was pulsed with a square wave on/off cycle for 100 periods. The TEM grid was then removed and analyzed. In order to obtain large quantities of powder for bulk analysis, the plasma was pulsed for several hours and the filter with accumulated powder was removed.

RESULTS AND DISCUSSION

Silicon

In a study aimed at duplicating the experimental conditions of Boufendi et al, we investigated the formation of silicon particles in a silane/argon plasma. We find that the growth kinetics differ very markedly from those of the French group. In Fig. 2 is shown the measured size distribution for silicon particles as a function of plasma-on time with the upper and lower solid line giving one standard deviation. Shown for comparison are dashed lines depicting the distribution obtained under apparently similar conditions by Boufendi et al. We observe an initial rapid growth in particle diameter which, for longer plasma on-periods, decreases to a slow growth rate. In addition,

the size dispersion is very large, in fact, with all sizes from zero to approximately twice the average diameter represented. We are unable at this time to resolve the discrepancy between our particle growth

Figure 2

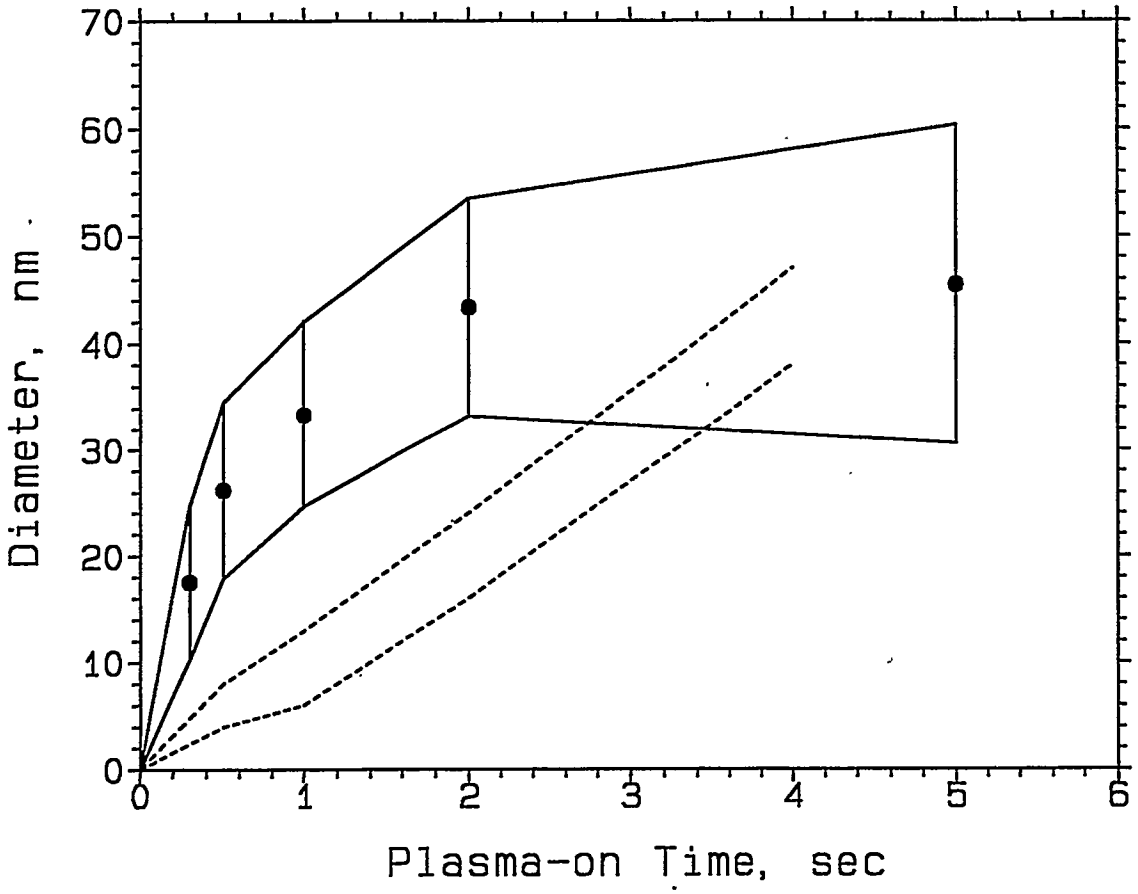

Fig. 2. Silicon particle size distributions obtained from a pulsed silane/argon plasma. Dashed lines show the data of Ref. 7.

dynamics and those of Boufendi et al. Great effort was expended to match conditions of geometry, linear flow velocities, pressure and power. Plasmas are, however, notoriously difficult to reproduce quantitatively in different laboratories. We are not actually able to confirm, at this time, that the plasma density, spatial uniformity, or temperature truly coincide with those of Boufendi et al.

Silicon Nitride

Pulsed rf plasmas of silane/ammonia gas mixtures successfully generated nano-size particles. The chemistry of the particles appears consistent with our earlier observations using a continuous rf plasma[5]. Fourier transform infrared spectra (FTIR) show strong SiH (2100 cm^{-1}) and NH absorptions (3400 cm^{-1}), confirming that the powder has a high hydrogen content. The powders formed in a pulsed plasma have a color associated with a stoichiometric ratio of Si/N, but elemental analysis has not yet been performed. Fig 3. is a TEM picture of silicon nitride particles formed with 100 cycles of a 0.25 sec-on discharge. The average particle size determined from analysis of many TEM photos is

Figure 3

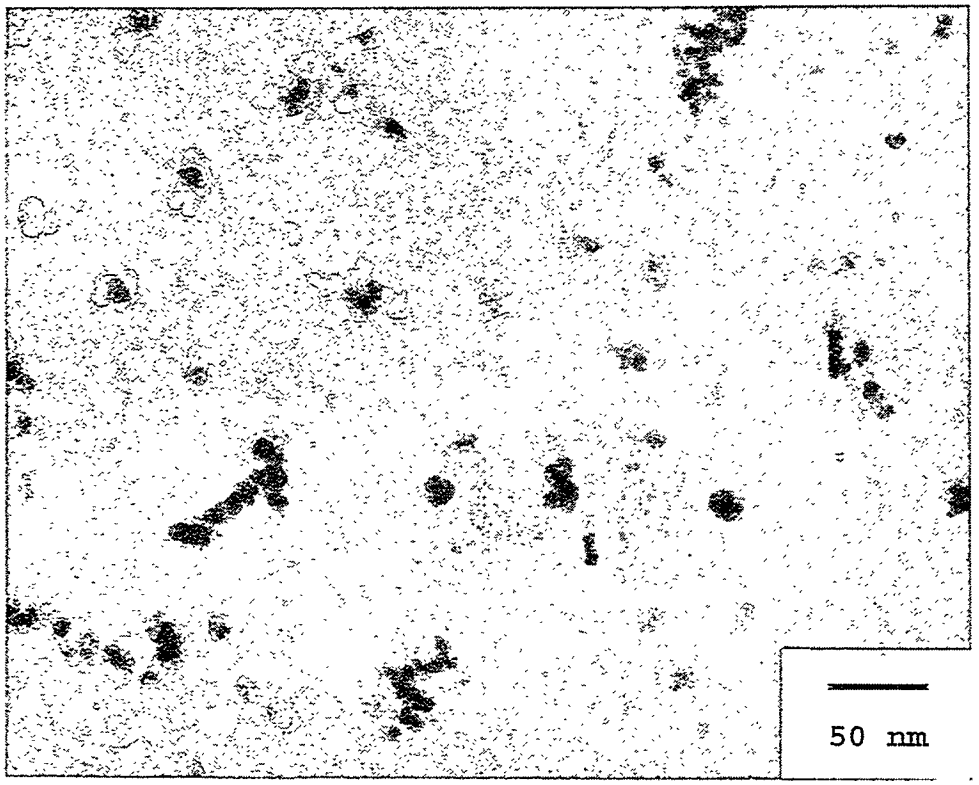

Fig. 3. TEM of particles synthesized in a SiH_4/NH_3 plasma pulsed on for 0.25 sec, off for 2.0 sec.

15 nm diameter. It is clear that many particles have agglomerated into clusters or chains and that the size dispersion is large. Similar pictures were analyzed for different plasma on-times and a sample of the results is shown in Fig. 4. The average diameter is shown with a solid dot and is seen to increase fairly linearly in time. A point has been graphed for each measured particle to show the distribution of sizes. Clusters and agglomerates were not included. It is apparent that

Figure 4

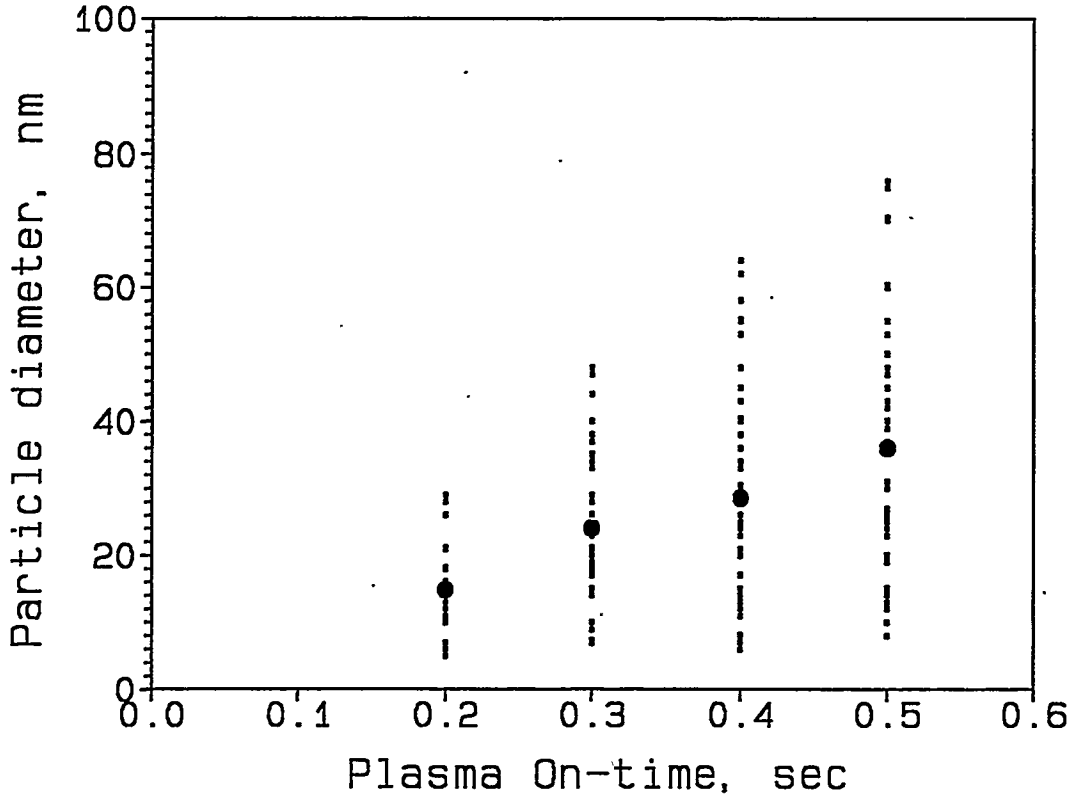

Fig. 4. Particle size distributions from a SiH_4/NH_3 plasma, large dot is the mean diameter.

particle nucleation is an ongoing phenomenon during the plasma-on period. All sizes of particles are approximately equally represented

and the simplest model is that a particle may nucleate at any time and it then grows at a constant rate until the plasma is extinguished.

The observed agglomeration of particles is potentially detrimental to the ultimate goal of producing high density ceramic material. It is generally expected that hard agglomeration into complex shapes will seriously degrade the ability to obtain close packing. It is important to establish the physical mechanisms leading to agglomeration. An isolated body suspended in a plasma acquires a negative potential relative to the plasma because the electron velocity greatly exceeds that of the positive ions. We would expect that the negatively charged particulates should repel each other and remain separated. This would only break down when the particle mass becomes very large. When the plasma is extinguished, though, the particles may be neutralized by the residual ions and could agglomerate through collisions.

Close inspection of the agglomerates seen in TEM photographs reveals that some are very strongly fuzed as if significant material growth has occurred after association of the particles. This would seem to point to a mechanism of agglomeration in the plasma itself at least for some particles. The smooth appearance of the particle surface might suggest melting and neck-formation by mass transport. The temperature of the gas and ions in the plasma is, however, very low, probably less than 50 C. The particle is presumably nucleating and growing by highly exothermic reaction of radicals which might heat the growing particle faster than it can radiate. If the particle were to exceed 1000 C, however, it would desorb the bound hydrogen, in conflict with the post-plasma FTIR results. Thus, particle melting should be discounted.

One additional observation is relevent. When laser light scattering was monitored either in the bulk of the plasma, or beneath the electrode assembly (with and without the lower screen), no particles were observed during the on-cycle. A sudden appearance of light scattering occurred only in the instant after the plasma was extinguished. The individual particles below 100 nm do not scatter enough laser light to be visible by this technique, thus it appears that a burst of agglomeration occurs after the plasma is turned off.

CONCLUSIONS

The pulsed rf plasma technique is capable of generating silicon nitride powder with controlled average size in the 10 nm size regime. Large size dispersion and some degree of agglomeration are always observed. Compaction and sintering studies will be needed to evaluate these particles as precursor candidates for superior silicon nitride ceramics.

ACKNOWLEDGEMENTS

The authors gratefully acknowledge the valuable assistance of Charles Hills for obtaining the TEMs. Also this work was supported by the United States Department of Energy under Contract DE-AC04-94AL85000.

REFERENCES

1. D. L. Segal, Br. Ceram. Trans. J. **85**, 184(1986).

2. S. Prochazka and C. Greskovich, Amer. Ceram. Soc. Bull. **57**, 579(1978).

3. J. S. Haggerty and W. R. Cannon, in *Laser-Induced Chemical Processes*, edited by J. I. Steinfeld (Plenum Press, New York, 1981), p. 165.

4. R. J. Buss and P. Ho, US Patent No. 4,769,064.

5. P. Ho, R. J. Buss, and R. E. Loehman, J. Mater. Res., **4**, 873(1989).

6. see for example, Plasma Sources. Sci. Technol., **3** (1994). Entire volume devoted to the topic.

7. L. Boufendi, A. Plain, J. Ph. Blondeau, A. Bouchoule, C. Laure, and M. Toogood, Appl. Phys. Lett. **60**, 169 (1992).

MECHANICALLY RELIABLE SURFACE OXIDES FOR HIGH-TEMPERATURE CORROSION RESISTANCE*

K. Natesan, B. W. Veal, M. Grimsditch, D. Renusch, and A. P. Paulikas
Argonne National Laboratory
Argonne, IL 60439

ABSTRACT

Corrosion is widely recognized as being of profound technological importance, but an understanding of the underlying phenomena (in order to characteriz material performance) involves factors such as the chemistry and physics of the early stages of oxidation, chemistry and bonding at the substrate/oxide interface, role of segregants on the strength of that bond, transport processes through scale, mechanisms of residual stress generation and relief, and fracture behavior at the oxide/substrate interface. Because of this complexity and the need for a wide range of different techniques, a multilaboratory program has been initiated under the auspices of the DOE Center of Excellence for the Synthesis and Processing of Advanced Materials, with strong interactions and cross-leveraging with DOE Fossil Energy and U.S. industry. The ultimate objective is to systematically generate the knowledge required to establish a scientific basis for designing and synthesizing improved protective oxide scales/coatings (slow-growing, adherent, sound) on high-temperature materials without compromising the requisite properties of the bulk materials. The objectives of program work at Argonne National Laboratory are to (1) correlate actual corrosion performance with stresses, voids, segregants, interface roughness, initial stages of oxidation, and microstructures; (2) study such behavior in growing or as-grown films; and (3) define prescriptive design and synthesis routes to mechanically reliable surface oxides. Several techniques, such as Auger electron spectroscopy, X-ray diffraction, X-ray grazing incidence reflectance, grazing-angle X-ray fluorescence, optical fluorescence, and Raman spectroscopy, are used in the studies. The project has selected Fe-25 wt.% Cr-20 wt.% Ni and Fe-Cr-Al alloys, which are chromia- and alumina-formers respectively, for the studies. This paper will present some of the results on early stages of oxidation and on surface segregation of trace elements.

INTRODUCTION

Protection from corrosion and environmental effects arising from reactions with gases and condensed products is required in order to fully exploit the potential of advanced high-temperature materials designed to improve energy efficiency and minimize deleterious environmental impact. This protection is best afforded by either formation of stable surface oxides that are slow growing, sound, and adherent to the substrate or deposition of coatings that contain or develop oxides with similar characteristics. The benefits of certain alloying additions on the growth and adherence of protective oxide scales on metallic substrates are well known, but there remains the need for a detailed understanding of the mechanisms by which scale properties and coating integrity are improved by compositional, microstructural, and processing modifications.

---

*Work supported by the U.S. Department of Energy, Office of Fossil Energy, Advanced Research and Technology Development Materials Program, Work Breakdown Structure Element ANL–4A and Basic Energy Sciences Materials Program, under Contract W–31–109–Eng–38.

The ultimate objective of this program is to systematically generate a scientific basis for designing and syntheszing of improved protective oxide scales/coatings (slow-growing, adherent, sound) on high-temperature materials without compromising the requisite properties of the bulk materials. Specific objectives are to (1) systematically investigate the relationships among substrate composition and properties and scale/coating adherence, damage tolerance, and micromechanical properties; (2) use such information to predict scale/coating failure; and (3) identify conditions leading to more damage-tolerant coatings and scales that are amenable to legitimate synthesis routes. The initial thrust is on alumina scales and coatings, but chromia-formers are used for comparative analysis. The emphasis is on materials systems with direct relevance to application suggested by the Electric Power Research Institute (EPRI) and DOE's Fossil Energy Program. The objectives of the ANL program are to (1) correlate actual corrosion performance with stresses, voids, segregants, interface roughness, initial stages of oxidation, and microstructures; (2) study such behavior in growing or as-grown films; and (3) define prescriptive design and synthesis routes to mechanically reliable surface oxides. Several techniques, are used in the studies, including Auger electron spectroscopy, X-ray diffraction, X-ray grazing incidence reflectance, grazing-angle X-ray fluorescence, optical fluorescence, and Raman spectroscopy. The project has selected Fe-25 wt.% Cr-20 wt.% Ni and Fe-Cr-Al alloys, which are chromia- and alumina-formers, respectively, for the studies. This paper presents selected results on early stages of oxidation and on surface segregation of trace elements in alumina-forming alloys.

EXPERIMENTAL PROCEDURE

The experimental study has focused on Fe-25 wt.%Cr-20 wt.%Ni and Fe aluminide alloys, both of which are of interest in fossil energy applications. The former is a chromia-former and its composition is the basis for one of the commercial austenitic stainless steels. The latter alloys, which are alumina-formers, are in various stages of development under the sponsorship of DOE Fossil Energy. These alloys can be used as either structural material or as a cladding to protect the structural material against corrosion. Sheets of several Fe_3Al-based alloys were procured from Oak Ridge National Laboratory. Table 1 lists the compositions of the alloys used in the study. Coupon specimens were cut from the sheet material for thermogravimetric experiments and for spectroscopic studies.

Several types of experiments were initiated to examine the oxidation behavior of these alloys, with emphasis on early stages of scaling, microstructural changes in scales, trace-element segregation on the free

Table 1. Nominal chemical composition (wt.%) of alloys used in corrosion tests

Material	Cr	Al	Fe[a]	Other
FA 61	-	15.9	Bal.	-
FA 71	5.5	15.9	Bal.	-
FA 81	2.2	15.9	Bal.	B 0.01
FA 129	5.5	15.9	Bal.	Nb 1.0, C 0.05
FAX	5.5	15.9	Bal.	Nb 1.0, Mo 1.0, Zr 0.15, B 0.04
FAL	5.5	15.9	Bal.	Zr 0.1, B 0.05
FAS	2.2	15.9	Bal.	B 0.05

[a]Bal. = balance.

surface and scale/alloy interface, and scale spallation characteristics. Thermogravimetric experiments were performed at 1000°C with an electrobalance having a sensitivity of 0.1 μg, to establish the effect of alloy composition on long-term oxidation characteristics and scaling kinetics. Specimens were suspended from the balance in a vertical furnace and held for the desired exposure period. Ultrahigh-purity air, further purified by passing over a hot bed of Zr chips, was used in these experiments. Upon completion of the oxidation test, the furnace was opened and the specimen was rapidly cooled in high-purity air. Following thermogravimetric measurement of oxidation, scale surfaces and cross sections of specimens were examined with a scanning electron microscope equipped with an energy-dispersive X-ray (EDX) analyzer.

For the segregation studies, specimens of FA 71 alloy were exposed at 1000°C to high-purity argon for times of 10 min, 1, 5, and 10 h. Subsequently, the specimens were analyzed using Auger electron spectroscopy (AES), along with sputtering, to obtain AES spectra and depth profile analysis for Fe, Cr, Al, O, and S. For Raman and fluorescence spectroscopy studies, specimens of FA 71 and FAL alloys were used to examine the scale composition during scale development and evaluate the effect of exposure temperature on scale adhesion and spallation.

Raman spectroscopy studies were used to identify and monitor the evolution of Fe_2O_3 and Al_2O_3 in scales grown on FA 71 and FAL after sequential treatments in air at temperatures ranging from 300 to 1300°C. These sesquioxides can be readily identified from Raman spectra using the measurements as a "fingerprint" technique. Evidence of additional oxide phases in the scales is present from the spectra, but their identification is not straightforward. Further, some line broadening and spectral line shifts appear (possibly because of strains or impurity effects) but these are not considered in this paper.

The FA 71 and FAL alloys are alumina formers. However, the alumina scales that develop on these alloys after high-temperature oxidation contain a small amount of dissolved Cr. When Cr 3d electrons, from atoms substituting on Al sites, are excited, they de-excite by producing a sharp fluorescence doublet with a wavelength near 7000 Å. (The red gemstone ruby is a Cr-doped alumina; the red coloration comes from the Cr fluorescence.) As alumina scales form on the iron aluminides, the Cr fluorescence doublet becomes very prominent. Depending on scale-growth conditions, the doublet shifts and broadens, apparently as a consequence of varying strains in the alumina scale. The shifts provide a sensitive measure of strain accumulation in the scales and clearly indicate when strain relief occurs.

RESULTS AND DISCUSSION

Figure 1 shows the oxidation data for several of the alumina-forming alloys at 1000°C in air. Oxygen uptake for the alloys is fairly rapid in the initial 10 h, after which the rate of weight change was greatly reduced. Some of the alloys, such as FA 61 and FA 71, exhibited extensive spallation when cooled to room temperature. On the other hand, alloys such as FAL and FA 129 exhibited fairly adherent oxide scales in similar experiments. Figures 2 and 3 show SEM photomicrographs of surfaces of different alloys exposed to air at 1000°C. The ternary alloy FA 71 exhibited severe spallation of the scale, while alloys such as FA 129, FAX, and FAL exhibited adherent alumina scales with several locally spalled regions on the alloy surface. The mode of scale cracking was different in each alloy, indicating that alloy composition

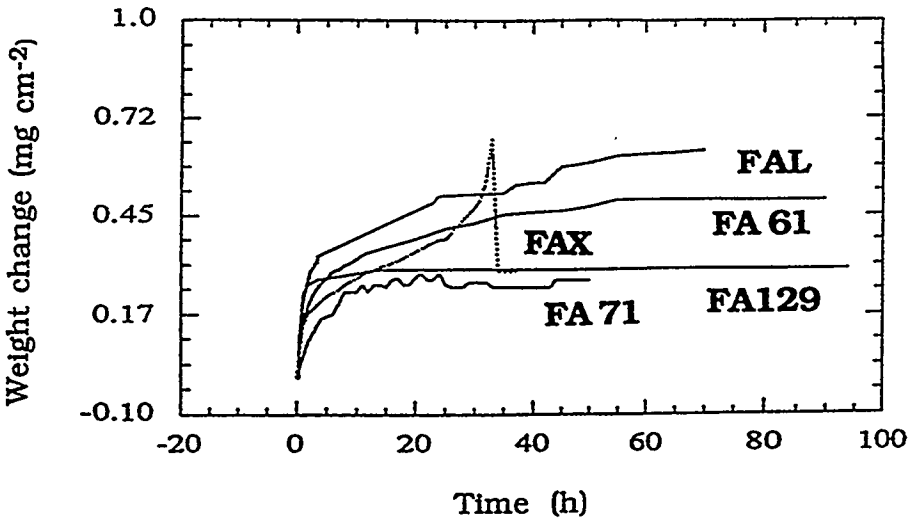

Fig. 1. Weight change data for several Fe aluminide alloys tested in air at 1000°C.

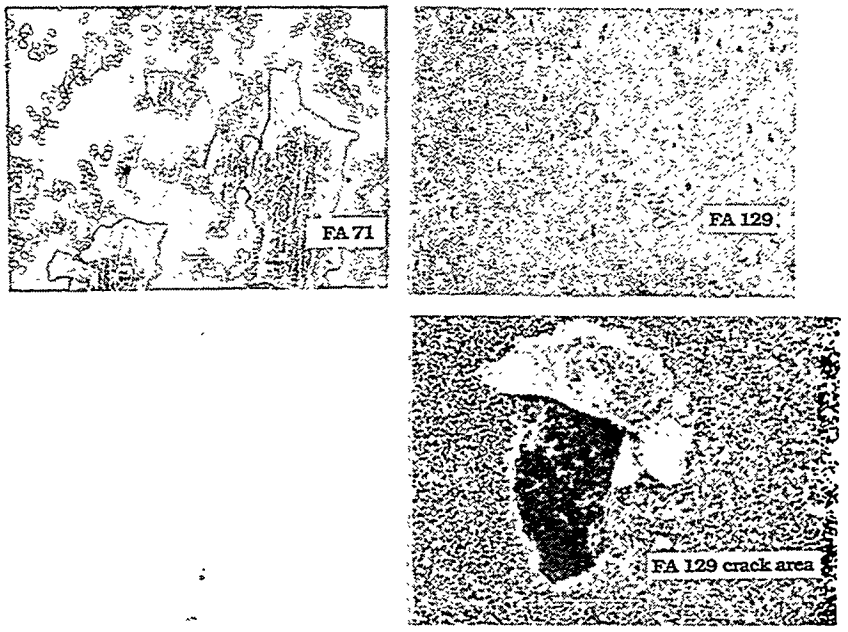

Fig. 2. Scanning electron photomicrographs of surfaces of FA 71 and FA 129 alloys tested in air at 1000°C.

may play a significant role in scale development and subsequent spallation. Figure 4 contains cross-sectional SEM pictures that display the thickness and morphology of scales developed in the alloys after 100 h of exposure at 1000°C.

Figure 5 shows the AES spectra for specimens of FA 71 in the initial condition and after 10 min, 1, 5, and 10 h ofexposure to high-purity argon at 1000°C. The argon contains sufficient oxygen to permit

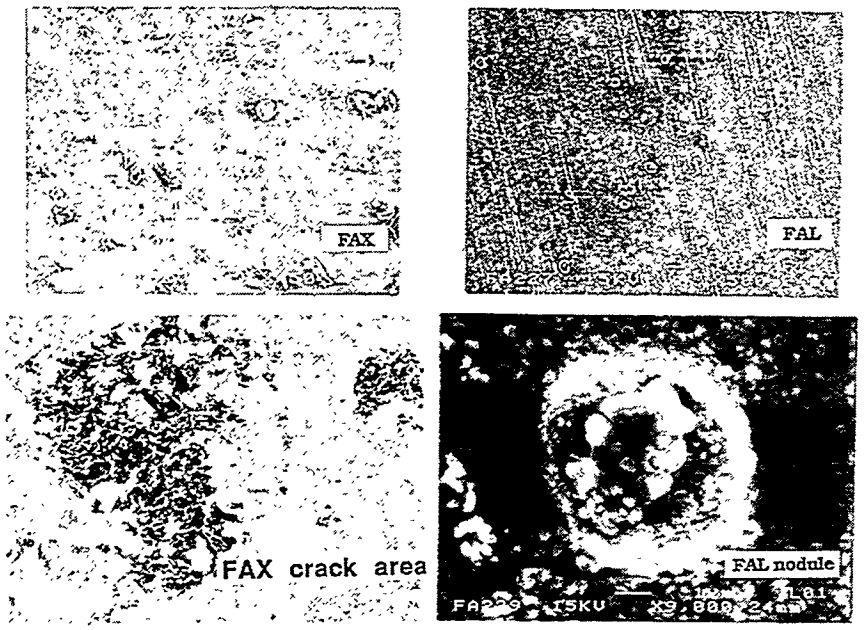

Fig. 3. Scanning electron photomicrographs of surfaces of FAX and FAL alloys tested in air at 1000°C.

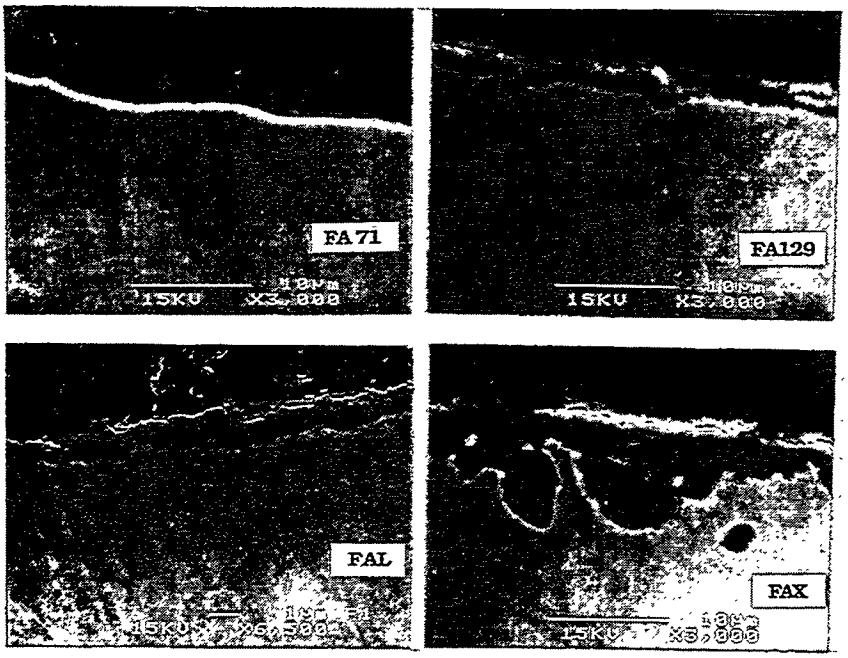

Fig. 4. Scanning electron photomicrographs of cross sections of several Fe aluminide alloys tested in air at 1000°C.

sustained scale growth. It is evident that the surface of the untreated specimen reveals S and that the peak height for S decreases exposure time increased from 0 to 1 h. Although S is absent in the specimen exposed for 5 h, a significant S peak can be observed in the specimen exposed for 10 h. Figure 6 shows the elemental depth profiles obtained by AES analysis for several of the specimens. It is evident that after 10

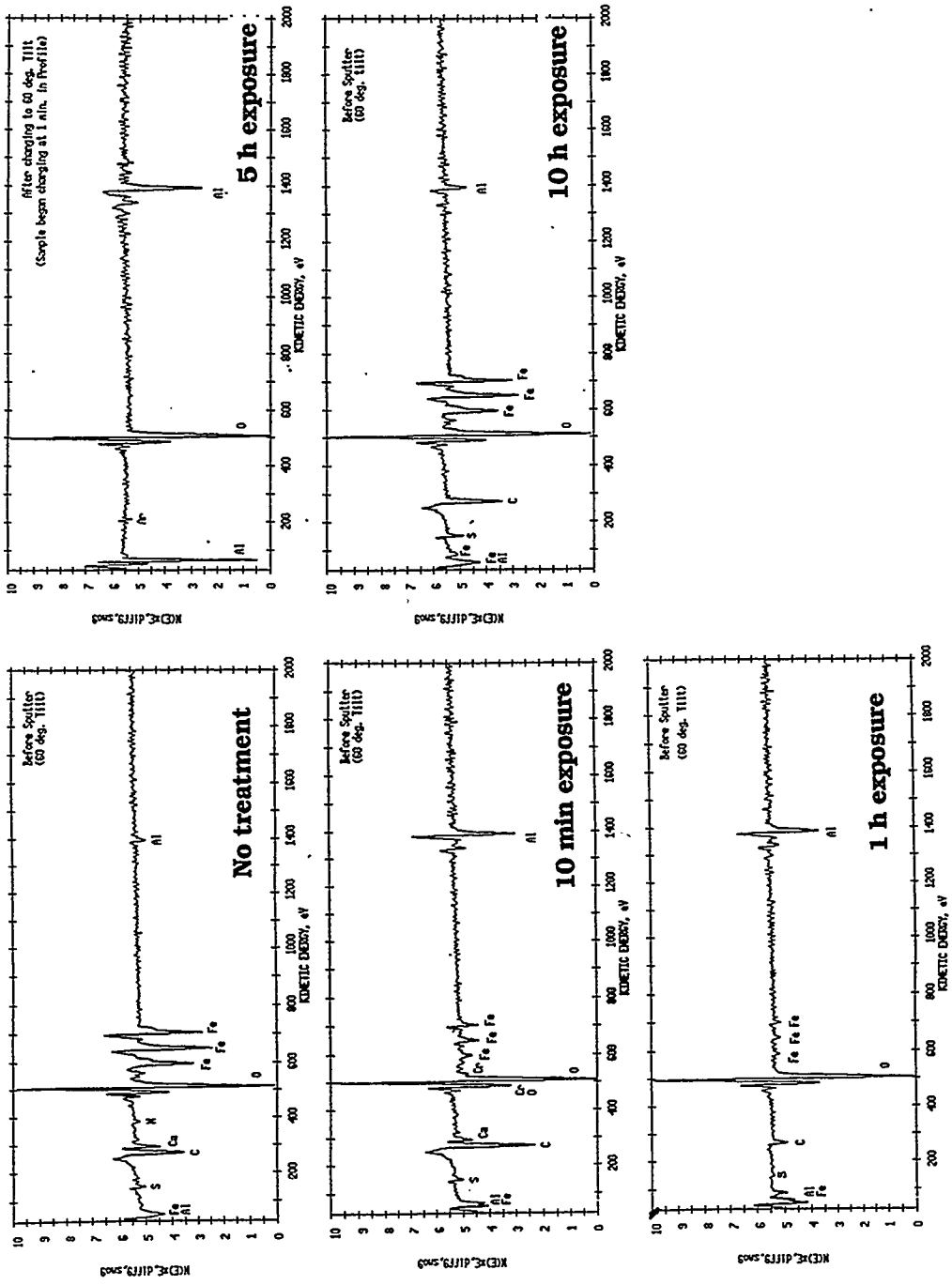

Fig. 5. Auger electron spectroscopy spectra for FA 71 alloy in as-received condition and after exposure in air at 1000°C for several time periods.

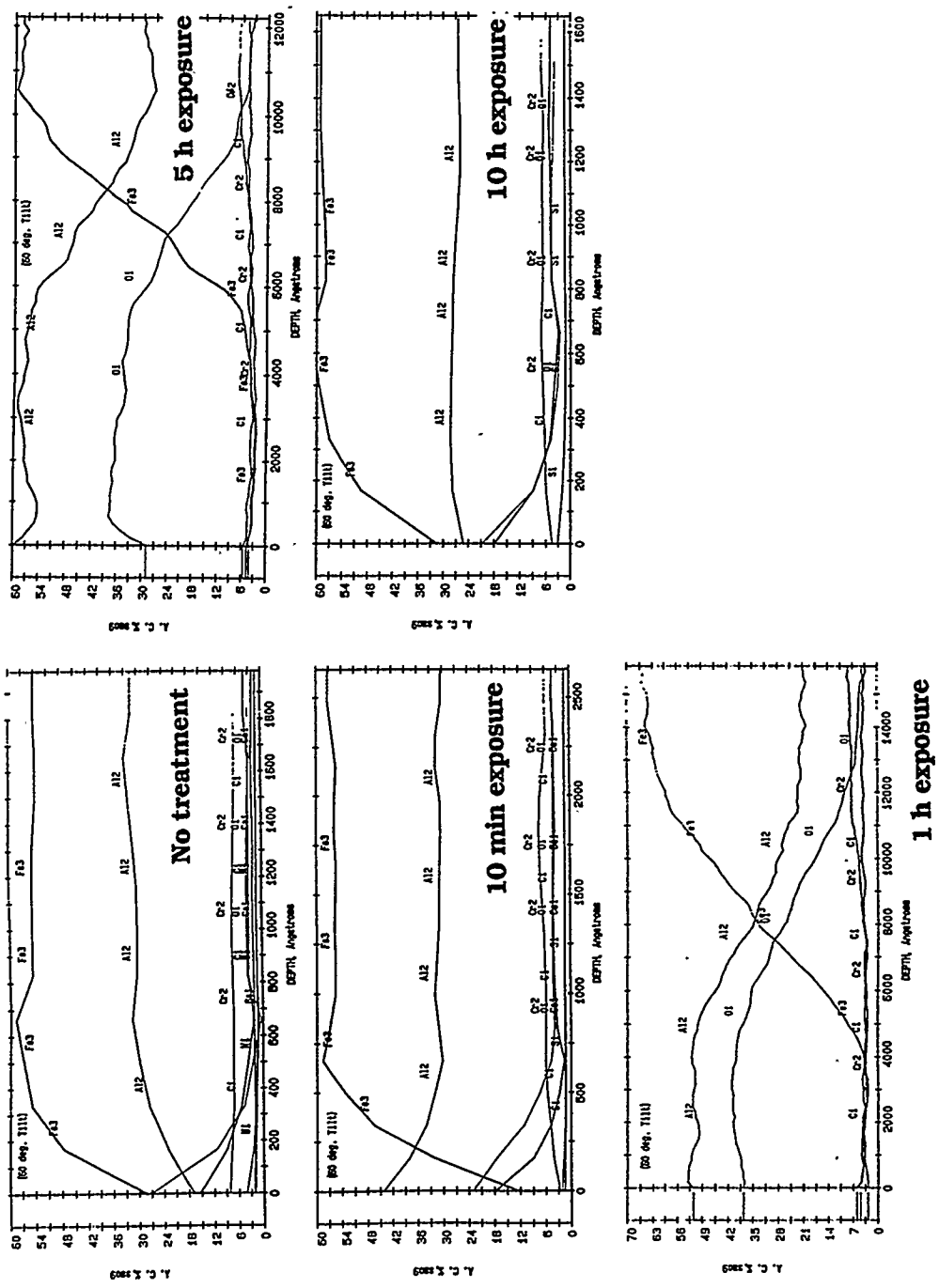

Fig. 6. Auger electron spectroscopy depth profiles for FA 71 alloy in as-received condition and after exposure in air at 1000°C for several time periods.

min of exposure the scale contained significant Fe but that the Al and O concentrations increased to a depth of ≈500 Å. After 1 h of exposure in argon, Fe content in the scale decreased significantly to a depth of ≈4000 Å. Further increase in exposure time to 5 h resulted in almost pure alumina scale of ≈5000 Å thickness. Exposure time of 10 h resulted in destruction of the pure alumina scale, and the elemental depth profiles were similar to those obtained after 10 min exposure of the virgin alloy. These preliminary results indicate that there may be a critical oxide thickness in alumina-forming alloys that can lead to spallation after cycling to room temperature, and that this thickness may be achieved with exposure times of 5-10 h at 1000°C. The observed behavior of scaling and spallation may also be due to segregation of S, initially at the alloy surface, to the scale/alloy interface, which can lead to debonding of the scale.

Figure 7 shows elemental concentrations for Fe, Al, O, and S in the surface of argon-exposed specimens as a function of exposure time. Figures 8 shows the surfaces of FA 71 specimens after 10 min, 1 h, and 5 h of exposure to argon at 1000°C. In 10 min, the alloy shows the grain boundaries of the original material and little or no scaling. In 1 h, the scale is fragmented but analysis showed it to be predominantly alumina. After 5 h of exposure, the oxide exhibited significant texturing, probably dictated by the original polishing lines of the specimen. The scale exhibited a number of transverse cracks (i.e., between the parallel grinding lines) and some spallation. However, the scale composition was predominantly alumina. Figure 9 shows photomicrographs of specimens exposed for (a) 10 h, (b) 10 h followed by polishing and further exposure of 5 h, and (c) 10 h plus polishing and 5 h of exposure repeated twice. It is evident that the scale is very friable and that spallation is expected. This also confirms the

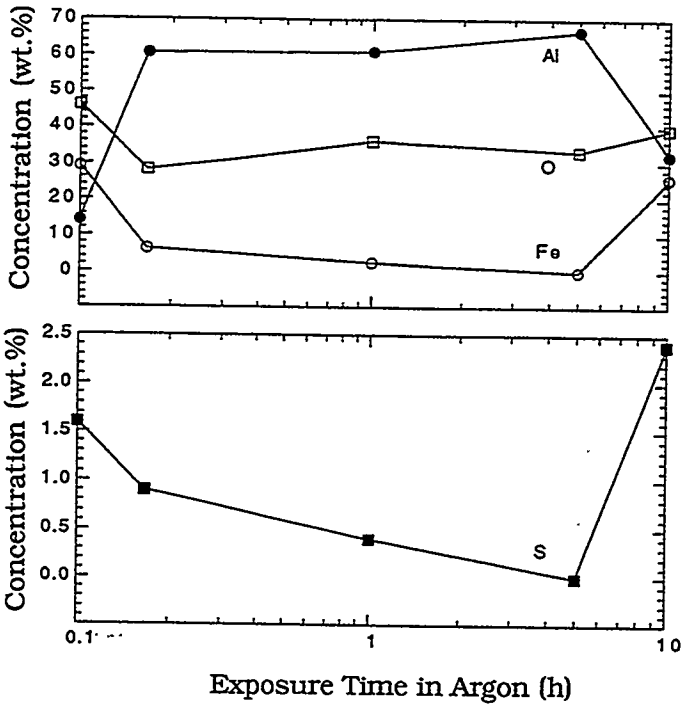

Fig. 7. Variation in concentration of Fe, Al, O, and S on the surfaces of an FA 71 alloy as a function of exposure time in air at 1000°C.

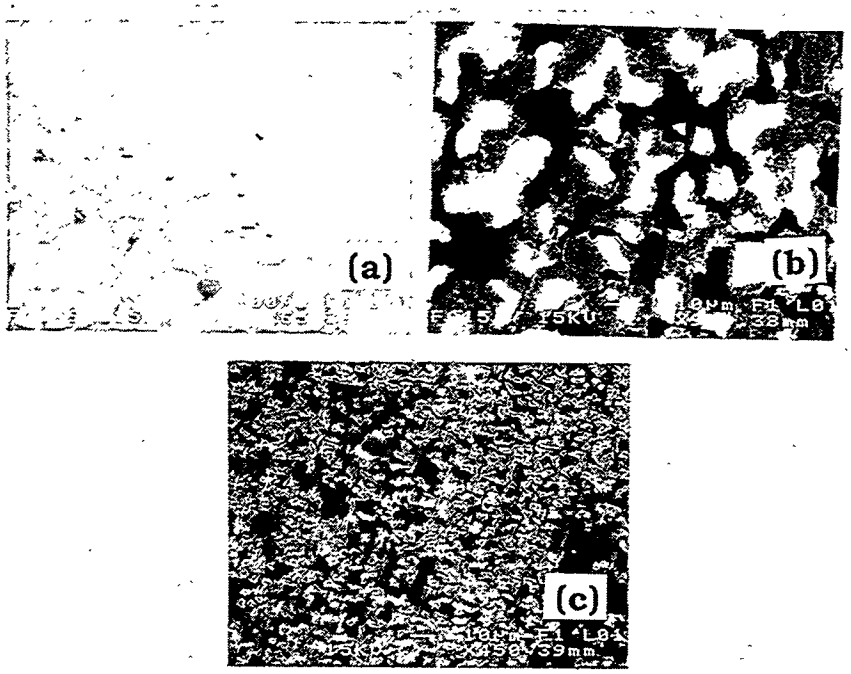

Fig. 8. Scanning electron photomicrographs of surfaces of FA 71 exposed in air at 1000°C for (a) 10 min, (b) 1 h, and (c) 5 h.

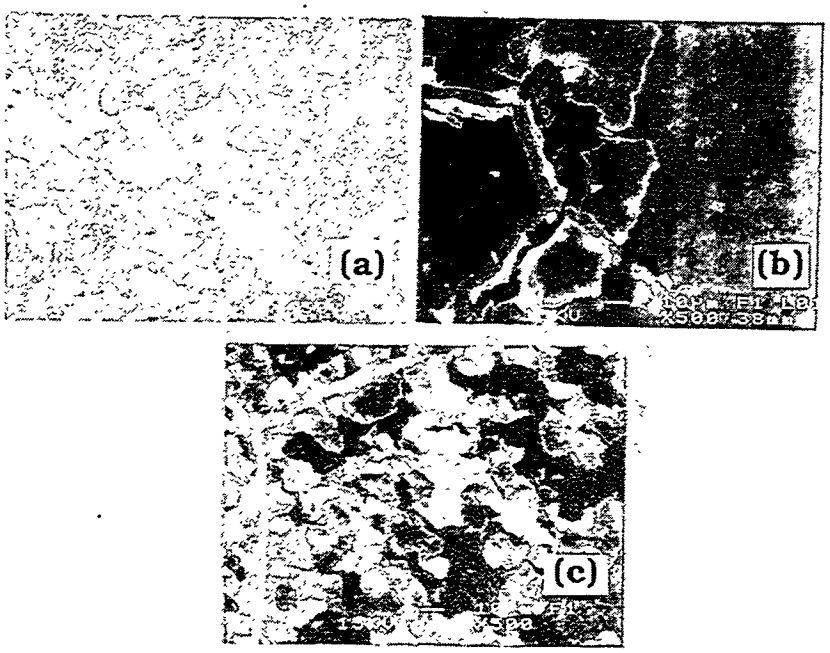

Fig. 9. Scanning electron photomicrographs of surfaces of FA 71 exposed in air at 1000°C for (a) 10 h, (b) 10 h plus polished and re-exposed for 5 h, and (c) 10 h plus re exposure step in b repeated twice.

AES results that scale composition changes from pure alumina to Fe-containing alumina as exposure time increases from 5 to 10 h. Additional experiments are in progress to examine this aspect of scaling and spallation, as well as toevaluate the role of other alloying elements in the scaling/spallation process.

Figure 10 (left panel) shows a series of Raman spectroscopy measurements for the FA 71 alloy. The top spectrum contains data taken at room temperature before oxidation. The spectrum is featureless because the underlying metal provides no Raman sensitivity in this spectral range. Beginning at 300°C, the samples were then oxidized for 1 h, and a Raman spectrum was taken at room temperature. One-hour oxidation treatments, followed by room-temperature measurements, were repeated at 100°C intervals to a final temperature of 1300°C. The data in Fig. 10 indicate that by 500°C, Fe_2O_3 appears prominently in the scale and is replaced by Al_2O_3 at T > 1000°C. Also shown in Fig. 10 (right panel) are room-temperature "ruby line" fluorescence measurements from FA 71 scales after heat treatments of 1 h beginning at 750°C, with sequential oxidation at 50°C intervals. The fluorescence signal first appears at T ≈750°C and grows rapidly in intensity with subsequent oxidation. At temperatures below 950°C, the peak position displays a red shift when samples are oxidized at increasingly elevated temperatures. This shift indicates that an increasing compressive strain is developing in the scale. (We note that the red shift of the ruby doublet is used for measurement and calibration of hydrostatic pressure in diamond-anvil pressure cells.) Strain relief (at room temperature) clearly occurs when reaction temperatures exceed ≈950°C, probably because of crack

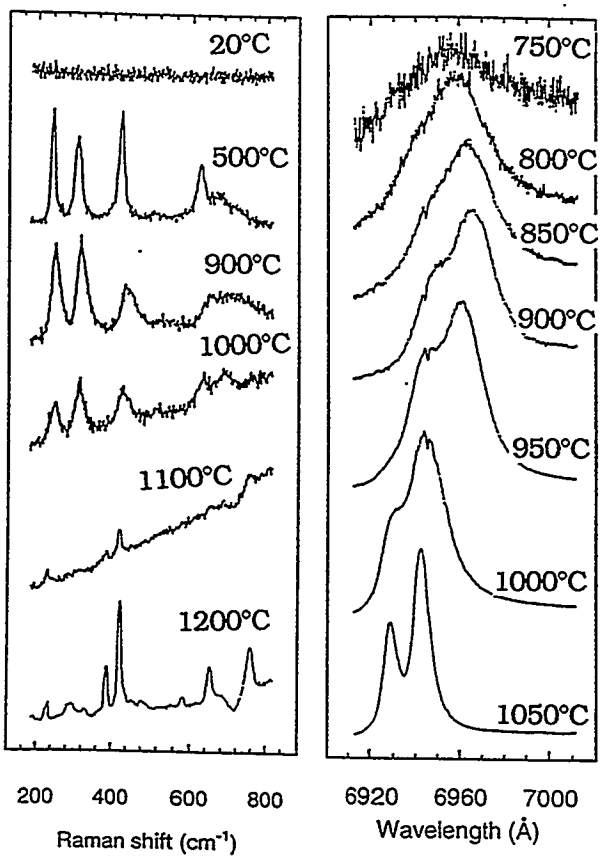

Fig. 10. Raman spectroscopy data obtained for FA 71 alloy after oxidation at several temperatures.

formation in the scales, thus signaling the onset of spallation. The 1050°C spectrum in Fig. 10 is very similar to that of natural unstrained ruby; apparently this spectrum identifies scale delamination.

Figure 11 shows intensity measurements of the Raman signal for Fe_2O_3 and of the ruby fluorescence (data in Fig. 10) plotted vs oxidation temperature. (Raman spectroscopy is not ideal for precise intensity measurements, but dramatic changes occur with oxidation and thus observed trends are clearly meaningful.) The presence of iron oxide in the scale is dominant for temperatures up to ≈750°C. At this temperature, Al_2O_3 first appears and, for subsequent treatments, dominates the scale. Figure 11 shows scale evolution through a transient region heavily influenced by Fe_2O_3 to the formation of the protective Al_2O_3. Curve (a) in Fig. 11, showing a rapid increase in intensity for T > 1000°C, is based on data from sample FA 71. Curve (b) is from sample FAL, which contains the reactive element Zr that is known to provide increased scale adhesion. The rapid growth of scale (a) relative to scale (b) is probably due to increased spallation failure with rapid oxidation of exposed substrate.

Figure 12 shows measurements of the ruby line peak shift vs. oxidation temperature (data in Fig. 10) for samples FA 71 (open circles) and FAL (solid squares). For temperatures below 900°C, the scales are adherent and the ruby lines show a continuous shift to the red as strain buildup increases. At 950°C, an abrupt blue shift (apparent in both FA 71 and in FAL) was observed. We are exploring the possibility that this effect might be associated with the θ-to-α phase transition that occurs near 950°C. With further oxidation at T > 950°C, the FAL scale can acquire increased strain without catastrophic failure. The solid line in Fig. 12 denotes the maximum red shift and hence maximum strain sustained by the scale. It appears that the maximum sustainable strains occur in FAL at T ≈1050°C. Using published values of spectral shift vs. hydrostatic pressure for ruby, and obtaining strain from bulk modulus data, we estimate that the linear strain in the scales processed at 900°C is about 0.8%.

For FA 71, scale failure is evident after 1 h of oxidation at 1000°C (preceded by oxidation at lower temperatures, as discussed above). An abrupt blue spectral shift occurring at 1000°C indicates catastrophic failure of the FA 71 scale. For oxidation temperatures greater than ≈1000°C, the spectra are comparable to those of conventional ruby, suggesting that the scale has completely debonded. At T > 950°C, multiple (shifted) doublets are observed at different points on the oxide scale, indicating varying degrees of scale adhesion. Multiple spectral peaks appearing at T > 950°C are plotted in Fig. 12.

These studies of the Cr fluorescence line in alumina scales provide the first application of Cr fluorescence spectroscopy for determining of strains and strain gradients in thermally grown scales. Further studies are underway to obtain the needed information to quantify both the magnitudes and the gradients of the strains that occur in the oxide scales.

SUMMARY

A multilaboratory program has been initiated by DOE to develop mechanically reliable oxide scales for high temperature corrosion resistance. Work at Argonne National Laboratory has focused on alumina-forming

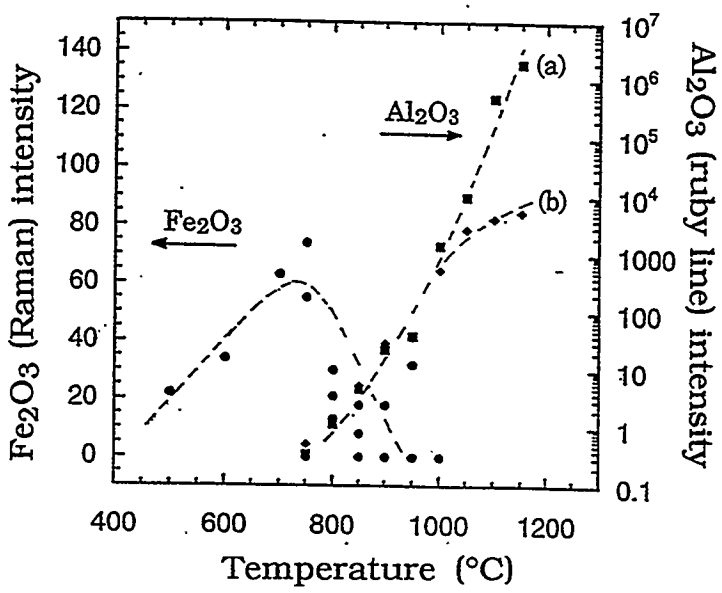

Fig. 11. Raman intensity data for Fe_2O_3 and ruby fluorescence data for FA 71 alloy as a function of oxidation temperature.

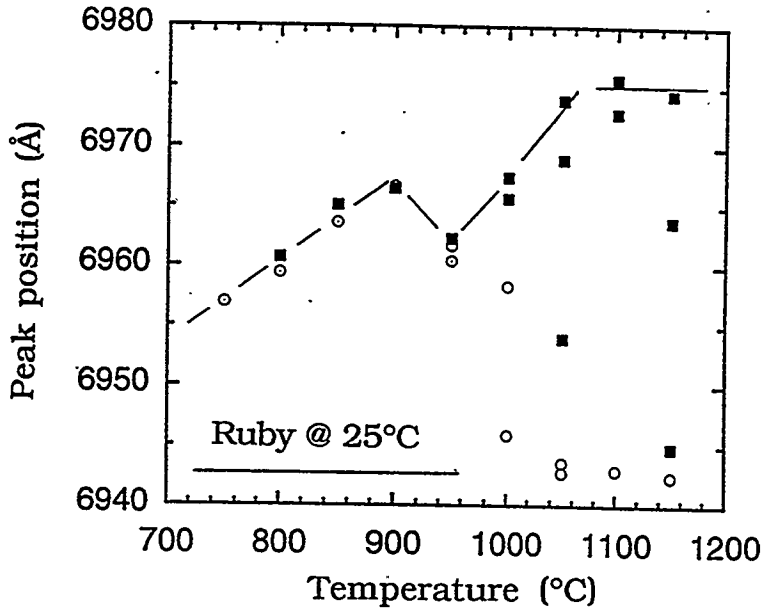

Fig. 12. Data on ruby line peak shift vs. oxidation temperature for FA 71 (open circles) and FAL (solid squares) alloys

alloyswith emphasis on examining the early stages of oxidation of several Fe-Cr-Al alloys and also evaluating the segregation behavior of trace elements in the alloy and their role in the scaling and spallation

processes that occur in oxidation of these alloys. Preliminary results are presented on the segregation data obtained by Auger electron spectroscopy and on scaling/spallation data from Raman spectroscopy.

ACKNOWLEDGMENTS

The authors thank V. Sikka and P. Tortorelli of Oak Ridge National Laboratory for supplying several of the alloys.

PLASMA SYNTHESIS OF ALUMINA FILMS ON METAL & CERAMIC SUBSTRATES

Ian Brown and Zhi Wang

Lawrence Berkeley Laboratory
University of California
Berkeley, CA 94720

ABSTRACT

We are exploring the feasibility of the plasma synthesis of highly-adherent films of alumina and chromia on SiC and FeAl substrates. A magnetically-filtered cathodic arc plasma deposition technique is used in which a high density metal plasma (Al or Cr) is formed and deposited on the substrate in the presence of a low pressure gaseous oxygen background. The substrate is simultaneously repetitively pulse biased, providing a means of controlling the incident ion energy. In the early stages of the process the ion energy is held in the keV range so as to produce atomic mixing at the film-substrate interface (ion stitching), and in the latter stages of deposition the energy is reduced to ~200 eV (IBAD range) to provide a means of controlling the film structure and morphology. Films that are dense and highly adherent can be formed in this way. We have produced near-stoichiometric films of alumina and chromia on small SiC and FeAl substrates and characterized the films in a number of ways, including RBS, X-ray diffraction and adhesion, and we've also done some preliminary temperature cycling experiments. The alumina films are of thickness from 0.2 to 1.5 μ, amorphous prior to heat treatment, and show an α-alumina phase after heat treating at 1000°C for up to 16 hours. The film substrate adhesion is typically greater than ~70 MPa prior to heating, and initial results indicate that the films maintain their adhesion after repetitive cycling in temperature between ambient and 1000°C. Here we describe the plasma processing method and outline the experimental results obtained to-date.

INTRODUCTION

Vacuum arc plasma discharges are intense sources of highly ionized, dense metal plasmas. Plasma generators based on this kind of discharge can be used to deposit thin films of various kinds including metals and alloys, and if the source is operated in a gaseous background then compounds including ceramic oxides can also be formed. We have developed techniques that combine plasma deposition with ion bombardment to create a powerful and adaptable new technology that is environmentally friendly, highly efficient, can be scaled up to large size, and can synthesize films of a range of materials[1-4]. The films can be atomically mixed to the substrate by the ion bombardment phase of the process to produce excellent film/substrate bonding at the atomic level.

A metal plasma of the required species is formed by a vacuum arc plasma gun and directed toward the substrate with a moderate streaming energy, typically of order 100 eV. At the same time, the substrate is

repetitively pulse biased to a moderate negative voltage (typically a few hundred to a few tens of kilovolts), thereby accelerating a fraction of the incident ion flux and energetically bombarding the ions into the substrate and the previously-deposited film. This technique provides a means for precise control of the energy of the depositing plasma ions. We use an early-time high ion energy so as to atomically mix the film into the substrate, and a lower (but optimized) ion energy during the bulk of the film growth so as to add an 'ion assist' to the deposition (similar to an ion beam assisted deposition, or IBAD, process). In this way the film is ion stitched to the substrate and has very strong adhesion, and it is also of high density (void-free), good structure (eg, not columnar), and good morphology (eg, close to atomically smooth).

In the work described here we've used this plasma materials synthesis technique to form films of Al_2O_3 and Cr_2O_3 on SiC and FeAl substrates. The films have been characterized, both before and after 1000°C heat treating, for composition and phase using Rutherford backscattering spectrometry (RBS) and X-ray diffraction analysis, and the film-substrate adhesion has been measured using a Sebastian-type pull tester. In the following we firstly outline the plasma and ion beam processing set-up, the substrate preparation, and the characterization methods used. The experimental results of the program to-date are then presented. Finally, we summarize and comment on the suitability of the method for this field of application.

EXPERIMENTAL PROCEDURE

Plasma Processing

We've made a number of different kinds of vacuum arc plasma guns, from small pulsed versions to a large dc embodiment. The sources can be operated either in a repetitively pulsed mode with pulse duration between 50 μs and 5 ms, or with long pulses (tens or hundreds of milliseconds), or d.c.; arc current is typically in the range 100 - 250 A. The guns are UHV-compatible and the cryogenically-pumped vacuum system base pressure is typically about 1×10^{-6} Torr. For the alumina and chromia films produced in this work, we used a "minigun" (Fig. 1) with arc pulses of 5 ms duration and a repetition rate of about 1 pulse per second. The cathode is a central cylindrical rod of the desired metal plasma species surrounded coaxially by a cylindrical anode. The arc pulses are initiated by a short (~10 μs) high voltage (~10 kV) trigger spark to the cathode. The plasma is created on the cathode surface and leaves the source as a directed plume through the annular anode. It is a fundamental characteristic of this kind of plasma discharge[5,6] that along with the plasma formation, a small fraction of 'macroparticles' is also produced – small particles of metallic cathode debris of dimension in the range 0.1 - 10 μ. If macroparticle filtering is desired, as for the

present purpose, a magnetic duct of suitable size is attached so that the plasma streams directly from the plasma gun into the filter[7]. With optimum magnetic field configuration[8,9] and optimum bias of the filter wall, about 25% of the ions produced in the arc discharge can be transported through the filter. Figure 2 shows plasma flowing through the magnetic filter used in the present work. The overall plasma deposition system thus consists of the repetitively pulsed plasma gun in conjunction with the 90° bent magnetic filter. Plasma exits the filter and deposits onto the appropriately positioned substrate.

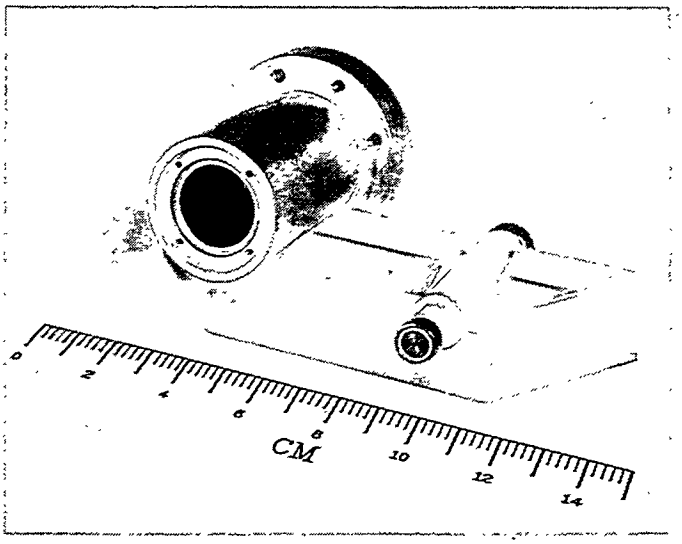

Figure 1. Partially disassembled vacuum arc plasma gun of the kind used here. The cathode assembly is shown removed from the anode.

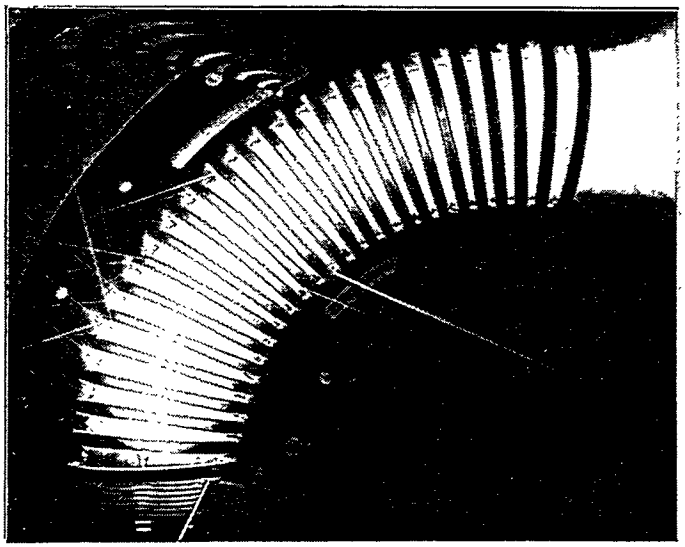

Figure 2. Magnetic filter, showing plasma injected from the gun at the lower left streaming through it and exiting at the upper right.

Films of metallic oxides can be formed simply by carrying out the plasma deposition not in a high vacuum environment, but in a somewhat higher pressure ambient of oxygen gas[10,11]. We have found empirically that a pressure in the range 1 - 100 mTorr is suitable for most metal oxides. Here the oxygen background pressure was 10 to 15 mTorr. The oxygen is both entrained in the plasma stream, ionized, and deposited in the plasma state, as well as reacting at the freshly-deposited metallic surface to form aluminum oxide. The net result is that, for the optimal oxygen pressure, a stoichiometric film of alumina is formed.

Ion energy of the depositing plasma flux is controlled by repetitively pulse biasing the substrate. Typically the pulse duration might be ~10 μs and the duty cycle ~10 - 50%. Pulsing of the bias voltage is necessary (for all but the lowest bias voltages) because a high voltage dc bias would cause an electrical discharge between the substrate and the vessel or the plasma gun; the plasma would be grossly perturbed (because the plasma sheath would expand from the substrate to large distances) and the ions would not be accelerated. The solution is to switch off the bias before such major perturbation can occur (to limit the sheath expansion to modest distances), let the plasma recover, and then repeat the process; ie, to do the biasing in a repetitively pulsed mode. For the early stages of the deposition process the pulse bias is held at a relatively high voltage of 2.2 kV. The mean aluminum ion energy is then 3.75 keV, because the mean ion charge state of the aluminum plasma is 1.7 (ref. 12) and $E_i = QV$. This energy results in implantation into the substrate to a depth of up to ~100 Å and intermixing of the Al film that is deposited during the pulse-off part of the pulse biasing. The aluminum film thus grows on the SiC substrate from a highly mixed interface. When an oxide is to be formed, the oxygen is also intermixed both by direct implantation of ionized oxygen as well as by recoil implantation of oxygen in the surface film. When a film thickness of just a few tens of angstroms has accumulated, the pulse bias voltage is reduced, since intermixing with the substrate is no longer a factor and the higher ion energy would sputter away the already-deposited film. Moreover, it is known from a large body of work on ion assisted deposition that a modest ion energy can be highly advantageous for controlling such characteristics as the density, morphology and structure of the film. For the bulk of the plasma deposition process the pulse amplitude is kept at 200 volts.

Substrate Preparation

The substrates were small coupons of silicon carbide and iron aluminide. The SiC was CVD-produced and was purchased from Morton Advanced Materials; the polished coupons were 0.5" x 0.5" square and 0.1" thick. The FeAl was supplied by ORNL and was in the form of polished 1 cm x 2 cm coupons approx. 1 mm thick.

Characterization

Analysis of film composition was done with Rutherford backscattering spectrometry (RBS) using 1.8 MeV He^+ ions, and X-Ray diffraction analysis was used to determine the crystallographic phase. Film adhesion was measured with a Sebastian-type pull tester using Sebastian studs epoxied to the samples and pulled normal to the substrate by known weights; the epoxy failure limit was typically ~70 MPa, and this thus determined the instrumental limit.

Procedure

Substrate samples were cleaned with alcohol and positioned within the vacuum chamber for the plasma deposition and ion bombardment processing. The oil-free system was cryogenically pumped down to a base pressure of about 1×10^{-6} Torr or better before commencing the plasma process. Oxygen gas was admitted to a pressure of typically 10 to 15 mTorr, and the plasma deposition and ion bombardment processing carried out as described above; the time required for film growth was usually a few tens of minutes. Note that in this plasma processing the energy added to the sample is small and they are not heated significantly. The samples were then removed from the chamber for characterization and testing. Heating was done in air in an oven which could be heated to 1100°C. The samples could be inserted into and removed from the hot oven quickly, and the sample heat-up and cool-down time was thus just a few minutes, determined by the thermal capacity of the small coupons. In the experiments conducted, the samples were maintained at full temperature at times varying between 15 minutes and 16 hours.

EXPERIMENTAL RESULTS

A number of different samples were prepared and studied, of both alumina and chromia and on both silicon carbide and iron aluminide. Several different thicknesses of films were formed, between about 0.2 μ and 1.5 μ. Issues that we considered important to address were:

- Stoichiometry of the plasma deposited film, both pre- and post-heat treatment;
- Crystallographic phase of the film produced, pre- and post-heat treatment;
- Adhesion of the film to the substrate, pre- and post-heat treatment;
- Adhesion of the film to the substrate following thermal cycling of the sample through a number of repeated high temperature excursions.

Stoichiometry

RBS analysis showed that the as-prepared samples were usually slightly oxygen-rich, with composition such as for example $Al_2O_{3.3}$ for an oxygen pressure of 12 mTorr. When the oxygen pressure was too high, for example 26 mTorr as in our early work, the films were significantly oxygen rich, with an Al_2O_5 composition. The post-heating films were, not surprisingly, of good Al_2O_3 stoichiometry.

Crystallography

The as-deposited alumina was typically amorphous with a small amount of κ-Al_2O_3, but for optimized plasma and ion beam processing conditions and oxygen gas pressure, we could form material containing largely α- and κ-Al_2O_3 (Fig. 3). The post-heating films were always largely α-Al_2O_3 (Fig. 4).

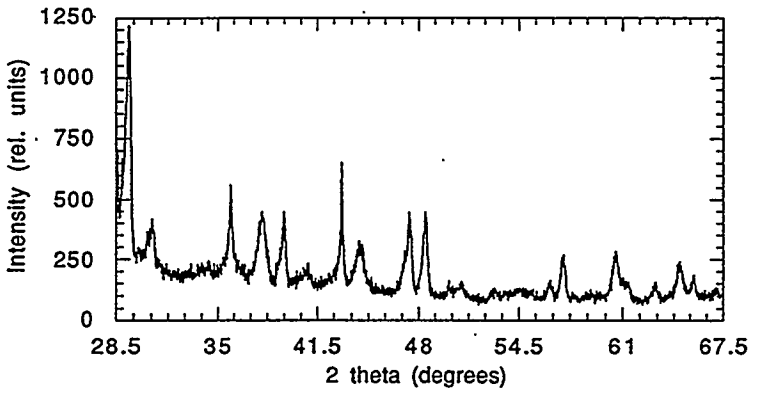

Figure 3. X-ray diffraction spectrum for an alumina film, as-deposited (pre-heating) at optimal conditions, indicating mostly α- and κ-Al_2O_3 phases. Film thickness 0.5 μ; on FeAl.

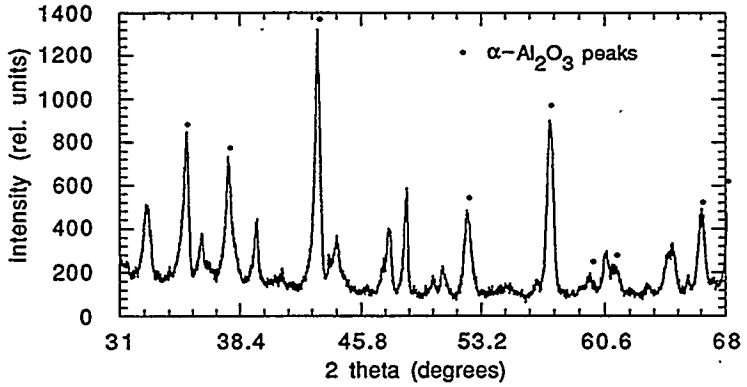

Figure 4. X-ray diffraction spectrum for an alumina film, after heating at 1000°C for 16 hours, indicating mostly α-Al_2O_3 phase. Film thickness 0.5 μ; on FeAl.

Adhesion

The film-substrate adhesion was always good for the as-prepared, pre-heat-treatment films – an adhesion strength as measured with our home-made Sebastian-type pull tester of $\gtrsim 70$ MPa, the instrumental limit of measurement – this for both alumina and chromia films on both FeAl and SiC. Post-heat-treatment, the adhesion strength of the optimally-prepared films is also good for films of thickness $\lesssim 0.5$ μ, but we've had mixed results to-date with films of thickness $\gtrsim 1$ μ. We refer here to heating to 1000°C for a period of either 15 minutes or 16 hours (we've done both), for a single heat cycling.

Adhesion after Repeated Thermal Cycling

We have at the present time data for one set of experimental conditions only. These data are for an alumina film of thickness about 0.25 μ formed on a SiC substrate. The sample was thermally cycled from room temperature to 1000°C though four cycles of 15 minutes duration each; heating and cooling time of the sample was one or two minutes only. The film-substrate adhesion both before and after temperature cycling was excellent, at the instrumental limit of the pull-tester.

CONCLUSION

Films of alumina (and also chromia) have been plasma synthesized on FeAl and SiC substrates. The process is straightforward and produces a mostly α-Al_2O_3 phase. The plasma deposition process is accompanied by a controlled and time-varied ion bombardment such that the film is atomically mixed to the substrate and consequently of high adhesion, and the ion-assist process during the bulk of the film growth helps to form good morphology. For optimally prepared films the film-substrate adhesion is $\gtrsim 70$ MPa, and at least for quarter-micron alumina films on SiC the film retains its integrity and full adhesion strength through a 4-cycle thermal cycling between ambient and 1000°C.

We have reported here on the status at the time of writing of our program to explore the feasibility of the plasma synthesis of alumina and chromia films on silicon carbide and iron aluminide substrates. Clearly there's much work that remains to be done. We can conclude, however, that the plasma and ion beam techniques described here provide a tool that could be valuable for the formation of highly adherent and thermally tolerant ceramic films.

ACKNOWLEDGEMENTS

We are indebted to Peggy Hou, Simone Anders, André Anders and Kin-Man Yu for help in various parts of the work, and to Bob MaGill and Mike Dickinson for support of the experimental equipment. This work was supported by the U.S. Department of Energy, Office of Advanced Research, Fossil Energy, under Contract Number DE-AC03-76SF00098.

REFERENCES

1. I.G. Brown, A. Anders, S. Anders, M.R. Dickinson, I.C. Ivanov, M.A. MacGill, X. Yao and K.M. Yu, Nucl. Instrum. Meth. Phys. Res. B80/81, 1281 (1993).
2. Ian Brown, in *Plasma Synthesis and Processing of Materials*, edited by K. Upadhya (pub. TMS, Warrendale, PA, 1993).
3. A. Anders, S. Anders, I.G. Brown and I.C. Ivanov, Mat. Res. Soc. Symp. Proc. 316, 833 (1994).
4. A. Anders, S. Anders, I.G. Brown, M.R. Dickinson and R.A. MacGill, J. Vac. Sci. Tech. B12, 815 (1994).
5. See, for instance,*Vacuum Arcs - Theory and Application*, edited by J.M. Lafferty, (Wiley, N.Y., 1980).
6. See, for instance,*Vacuum Arc Science and Technology*, edited by R.L. Boxman, P. Martin and D. Sanders, (Noyes, N.Y., 1995).
7. S. Anders, A. Anders and I.G. Brown, J. Appl. Phys. 74, 4239 (1993).
8. A. Anders, S. Anders and I.G. Brown, Plasma Sources Sci. Technol. 4, 1 (1995).
9. S. Anders, A. Anders and I.G.Brown, J. Appl. Phys. 75, 4895 (1994).
10. R.A. MacGill, S. Anders, A. Anders, R.A. Castro, M.R. Dickinson, K.M. Yu and I.G. Brown, "Cathodic Arc Deposition of Copper Oxide Thin Films", submitted to Surface and Coatings Technol.
11. S. Anders, A. Anders, M. Rubin, Z. Wang, S. Raoux, F. Kong and I.G. Brown, "Formation of Metal Oxides by Cathodic Arc Deposition", paper presented at the Int. Conf. on Metallurgical Coatings and Thin Films, San Diego, CA, Apr 24-28, 1995.
12. I.G. Brown, Rev. Sci. Instrum. 10, 3061 (1994).

MECHANICALLY RELIABLE SCALES AND COATINGS

P. F. Tortorelli and K. B. Alexander

Oak Ridge National Laboratory
Oak Ridge, Tennessee 37831-6156

ABSTRACT

As the first stage in examining the mechanical reliability of protective surface oxides, the behavior of alumina scales formed on iron-aluminum alloys during high-temperature cyclic oxidation was characterized in terms of damage and spallation tendencies. Scales were thermally grown on specimens of three iron-aluminum compositions using a series of exposures to air at 1000°C. Gravimetric data and microscopy revealed substantially better integrity and adhesion of the scales grown on an alloy containing zirconium. The use of polished (rather than just ground) specimens resulted in scales that were more suitable for subsequent characterization of mechanical reliability.

INTRODUCTION

In many high-temperature fossil energy systems, corrosion and deleterious environmental effects arising from reactions with reactive gases and condensible products often compromise materials performance and, as a consequence, degrade operating efficiencies. Protection of materials from such reactions is best afforded by the formation of stable surface oxides (either as deposited coatings or thermally grown scales) that are slowly reacting, continuous, dense, and adherent to the substrate. However, the ability of normally brittle ceramic films and coatings to provide such protection has long been problematical, particularly for applications involving numerous or severe high-temperature thermal cycles or very aggressive (for example, sulfidizing) environments. A satisfactory understanding of how scale and coating integrity and adherence are improved by compositional, microstructural, and processing modifications is lacking. Therefore, to address this issue, the present work is intended to define the relationships between substrate characteristics (composition, microstructure, and mechanical behavior) and the structure and protective properties of deposited oxide coatings and/or thermally grown scales. Such information is crucial to the optimization of the chemical, interfacial, and mechanical properties of the protective oxides on high-temperature materials through control of processing and composition and directly supports the development of corrosion-resistant, high-temperature materials for improved energy and environmental control systems.

The work described in this paper is being conducted at Oak Ridge National Laboratory (ORNL) in collaboration with work sponsored by the Department of Energy's Office of Fossil Energy at Argonne National Laboratory (ANL)[1] and Lawrence Berkeley Laboratory (LBL)[2] and in concert with directly related activities that are part of the Office of Basic Energy Sciences' Center of Excellence for the Synthesis and Processing of Advanced Materials. These cooperative efforts allow the integration of several advanced and, in some cases, unique characterization, modeling, and coating/deposition techniques so as to systematically investigate the relationships among corrosion performance, bulk composition, and surface oxide chemistry, structure, adherence, and elastic and plastic properties. However, in order to effectively pursue these types of study, it is necessary to first determine the effects of alloy composition, microstructure, surface condition, etc. on high-temperature oxidation behavior and associated scale integrity and spallation tendencies for a particular system. This paper presents initial results in this regard with respect to alumina scales on iron-aluminum alloys using thermal cycling under oxidizing conditions to gauge scale integrity in terms of gravimetric data and microstructural characterization. A similar characterization effort will then be conducted for as-deposited alumina on similar substrates.[2]

This work will ultimately include several model material systems, which are defined as ones that develop, upon oxidation, slowly growing, chemically stable surface oxides that offer the potential for protection of the metal from rapid reaction at high temperatures and show a substantial sensitivity to small additions of certain alloying elements. Alumina on iron-aluminum alloys appeared to satisfy these criteria[3] and this system was chosen as the initial one for study.

EXPERIMENTAL PROCEDURES

Three iron aluminides were studied. Their compositions and common designations are listed in Table 1. Ingots of these alloys were prepared by arc melting and casting. These were then rolled to a final thickness of between 0.8 and 1.3 mm. Rectangular specimens (typically 12 x 10 mm) were prepared from these sheets. The surface finish was either as-ground (600 grit, SiC paper) or polished (0.3 or 1 μm, alumina paste).

Gravimetric measurements under thermal cycling conditions were used to establish overall corrosion behavior at 1000°C. These cyclic oxidation experiments were conducted in static air by exposing coupons in individual pre-annealed alumina crucibles to a series of (typically) 24-h exposures. At the end of each exposure period, the crucibles were taken

Table 1. Compositions of iron-aluminum alloys used in this study.

Alloy Designation	Concentration[a] (at. %)				
	Al	Cr	Zr	Nb	Other
FA186	28	5			
FA129	28	5	-	0.5	0.2 C
FAL	28	5	0.1	-	0.05 B

[a] Balance is Fe.

from the furnace hot zone into the ambient atmosphere in about 2 min. Both the weight of the specimen, W_S, and that of any spalled scale, W_O (as collected in the crucible holding the coupon), were measured prior to the start of each experiment and after every thermal cycle. In this way, the total reacted mass due to oxidation, W_t, where

$$W_t = \Delta W_S + \Delta W_O, \quad (1)$$

could be measured as a function of oxidation time. Several of the oxidized coupons were examined by scanning electron microscopy (SEM). Two plan-view scale specimens for transmission electron microscopy were prepared from cyclically oxidized FAL and FA129.

RESULTS

Cyclic oxidation results for duplicate FAL specimens with 600 grit surface finishes are shown in Fig. 1. Both ΔW_S and ΔW_O (filled and open symbols, respectively) are plotted versus time; each data point represents one thermal cycle. Note that the weight of spalled material was usually small. In contrast, significant amounts of spalled material were measured for cyclically oxidized FA129 (Fig. 2) and FA186 (Fig. 3). For both of these alloys, ΔW_O was consistently greater than ΔW_S. Comparing Figs. 2 and 3 with Fig. 1, and referring to eq. 1, the total reacted mass due to oxidation (W_t) is therefore significantly greater for FA129 and FA186, as shown in Fig. 4.

Distinct differences in the surface appearance of the respective oxidized iron-aluminide alloys were observed. Visual examination revealed a uniformly dark gray product on the FAL and a lighter, powdery scale on the FA129 and (based on substantially fewer observations) FA186. As typified by the representative SEM micrographs in Fig. 5, the oxidized ground FA129 surfaces exhibited areas of bare metal from where the oxide product had completely spalled and fragmented, loosely-adherent pieces of scale. In contrast, the

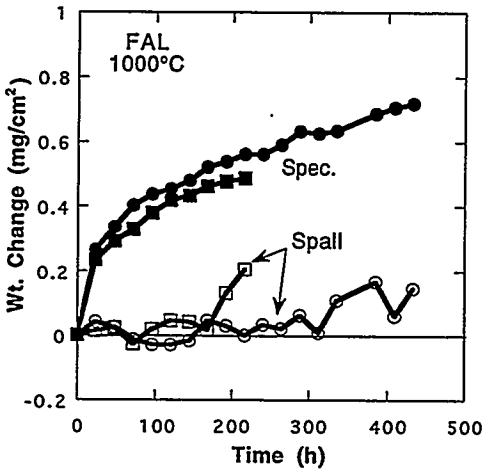

Fig. 1. Weight change versus time for FAL specimens cyclically oxidized in air at 1000°C. Each point represents one thermal cycle. Closed and open symbols represent weight changes of the specimen and spalled material, respectively. The specimens had a 600 grit surface finish.

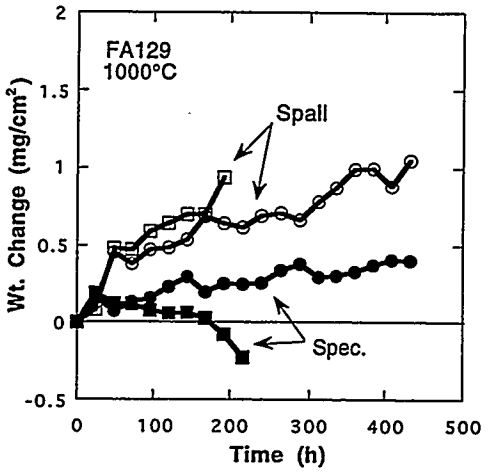

Fig. 2. Weight change versus time for FA129 specimens cyclically oxidized in air at 1000°C. Each point represents one thermal cycle. Closed and open symbols represent weight changes of the specimen and spalled material, respectively. The specimens had a 600 grit surface finish.

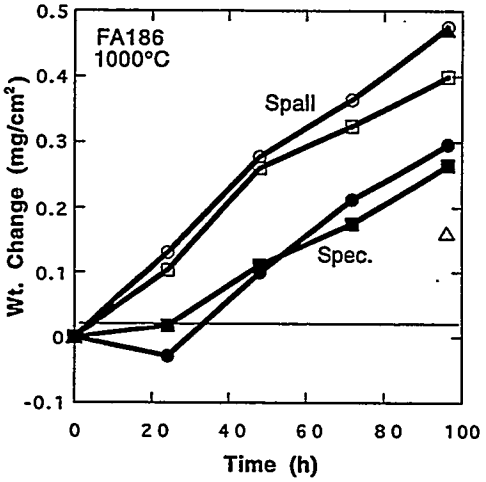

Fig. 3. Weight change versus time for FA186 specimens cyclically oxidized in air at 1000°C. Each point represents one thermal cycle. The triangles are for a specimen that was exposed for one 96-h cycle. Closed and open symbols represent weights of the specimen and amount of spalled material, respectively. The specimens had a 1 μm surface finish. The specimens represented by the circles and triangles were in the as-rolled condition prior to exposure. The squares indicated an annealed condition.

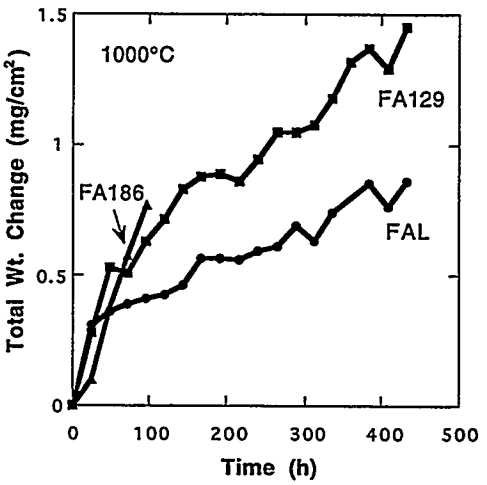

Fig. 4. Total weight change (weight of specimen plus that of spalled material) versus time for FAL, FA129, and FA186 specimens cyclically oxidized in air at 1000°C. Each point represents one thermal cycle.

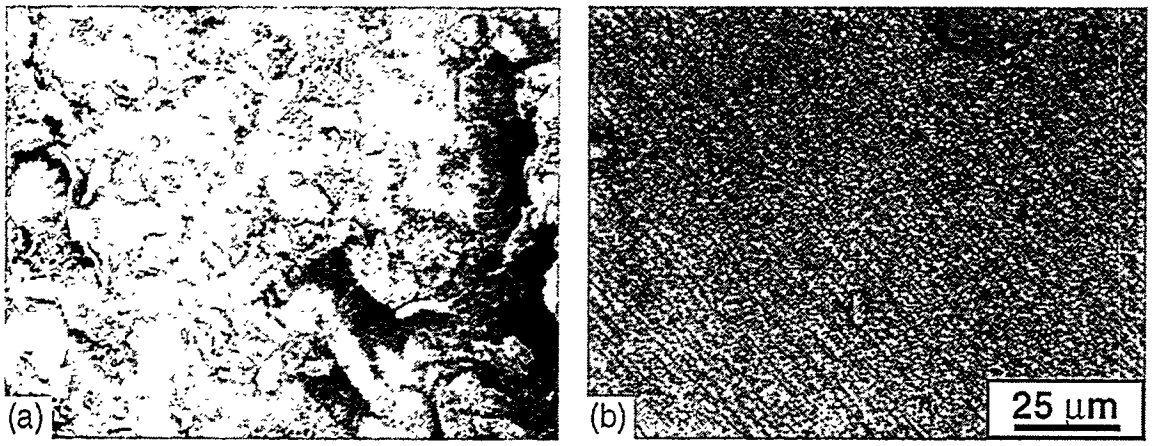

Fig. 5. SEM micrographs of ground (600 grit) iron-aluminum alloys that were oxidized for 48 h (2 24-h cycles) in air at 1000°C. (a) FA129 (b) FAL.

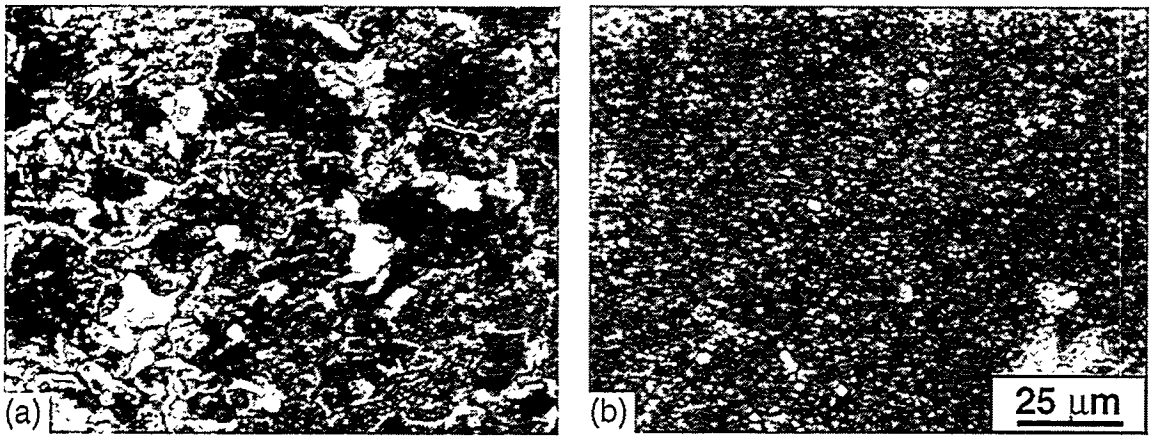

Fig. 6. SEM micrographs of polished (0.3µm) iron-aluminum alloys that were oxidized for 48 h (2 24-h cycles) in air at 1000°C. (a) FA129 (b) FAL.

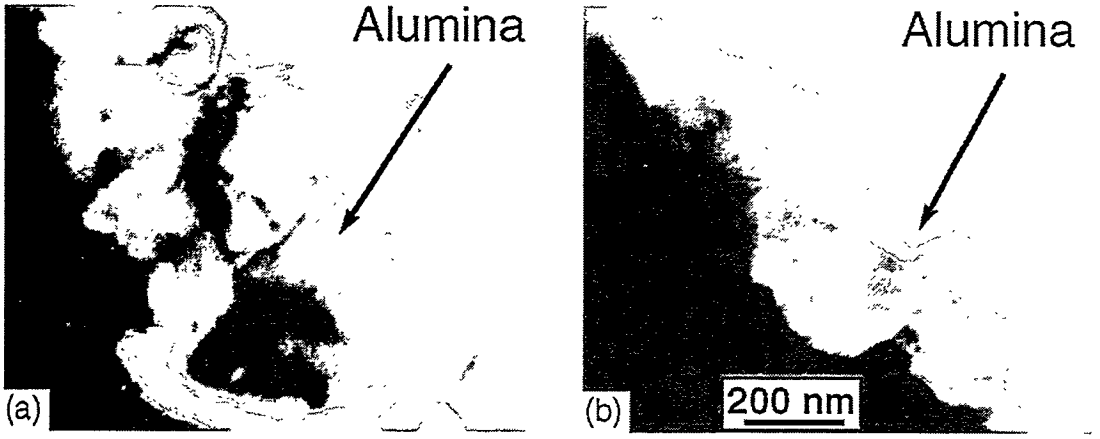

Fig. 7. TEM micrographs of iron-aluminum alloys that were oxidized for 48 h (2 24-h cycles) in air at 1000°C. (a) FA129 (b) FAL.

surface oxides grown on ground FAL were nodular and adherent. In this case, oxide appeared to nucleate along grinding marks - see Fig. 5b. These macro- and microscopic differences were observed regardless of exposure time. The surfaces resulting from cyclic oxidation exposures with specimens that first were polished to a finish of either 0.3 or 1.0 μm showed scale characteristics somewhat different from those observed for the ground specimens. As shown in Fig. 6, there was some, albeit small, areas of adherent scale on FA129, and a finer, less nodular, adherent surface oxide on FAL. Transmission electron microscopy of plan-view scales formed on FAL and FA129 showed very fine-grained oxides (approximately 200 nm) in both cases (Fig. 7).

Weight change measurements for polished specimens of FAL are compared to those for ground surfaces in Fig. 8. The ground specimens had slightly higher specimen weight gains, but all the mass changes shown in Fig. 8 are relatively small. With either type of surface finish, the weights of spalled material were substantially less than the respective changes in specimen weight. For FA129, the ΔW_o of a polished specimen was less than those of the ground ones (Fig. 9), which is consistent with the microscopy results described above. Polished specimens of FA186 were exposed in as-rolled and annealed (1000°C, 1 h) conditions. As shown in Fig. 3 (circles and triangles - as-rolled, squares - annealed), the differences in the gravimetric data due to starting microstructural condition was negligible.

Figure 8 also shows that the gravimetric data for FAL is cycle independent. Two FAL specimens with a 1 μm surface finish that were exposed for 96 h had identical weight changes despite the fact that one had four thermal cycles (square with cross symbols) and the other just one (filled square). In contrast, as shown in Fig. 3, the weight change data for FA186 did depend on the number of cycles - a specimen that was exposed for 96 h prior to cooling to room temperature (triangles) showed substantially different ΔW_s and ΔW_o than those measured for specimens of this alloy that underwent four 24-h thermal cycles from 1000°C (circles and squares).

DISCUSSION

Referring to eq. 1, the principal difference between FAL and the other two iron aluminides was in the weight of spalled scale, ΔW_o. Alloys FA129 and FA186 showed substantial scale spallation during cooling from the oxidation temperature at the end of most exposure periods. On the other hand, W_o for FAL was usually negligible (Fig. 1). These results, which were replicated for several specimens of each composition, are consistent with

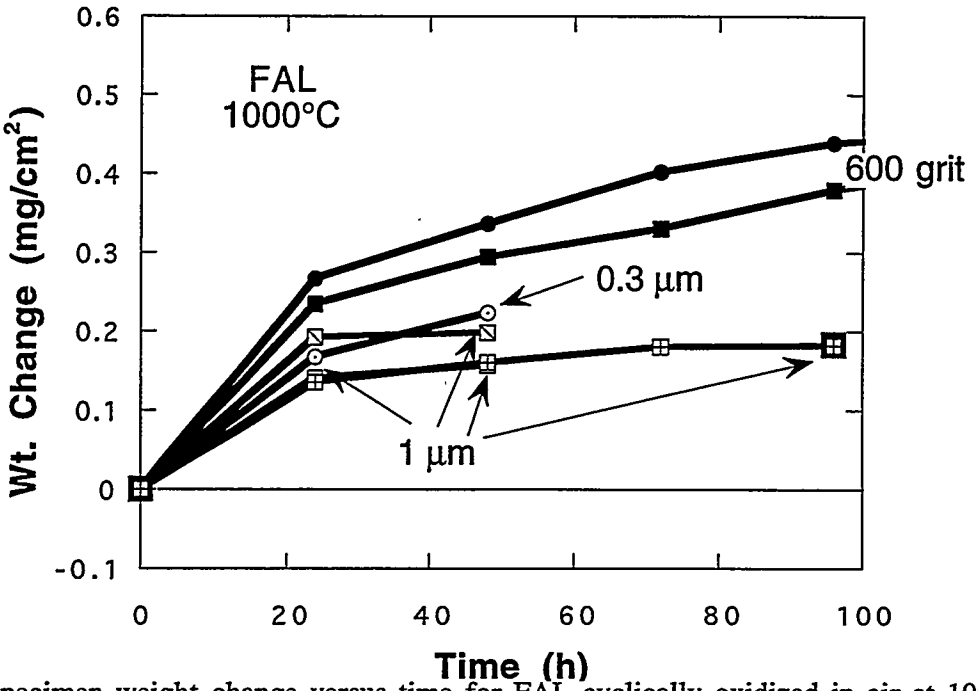

Fig. 8. Specimen weight change versus time for FAL cyclically oxidized in air at 1000°C. Each point represents one thermal cycle. The specimens had either ground (600 grit) or polished (0.3 or 1 µm) starting surfaces as indicated.

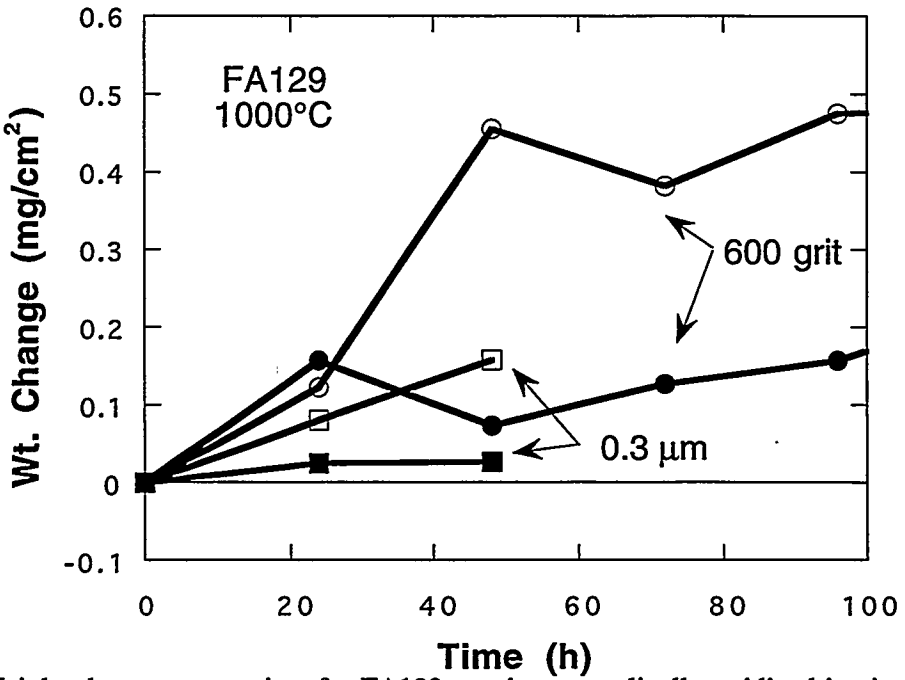

Fig. 9. Weight change versus time for FA129 specimens cyclically oxidized in air at 1000°C. Each point represents one thermal cycle. The specimens had either ground (600 grit) or polished (0.3) starting surfaces as indicated. Closed and open symbols represent weight changes of the specimen and spalled material, respectively.

earlier, preliminary studies showing that zirconium had a beneficial effect on the adherence of scales grown on Fe_3Al alloys at both higher (1300°C)[4] and lower (900°C)[5] temperatures. Zirconium is known to also have a positive effect on scale adherence in other alumina-forming alloys systems (see, for example, ref. 6), but the mechanism by which it provides a beneficial influence in iron aluminides has not been demonstrated. There is some electron microscopy evidence that zirconium ions accumulate in the alumina scale,[7] but these observations do not definitively prove any one particular model for the effect of this element on scale adherence. As the initial transmission electron microscopy revealed that the surface oxides on both FAL and FA129 were fairly fine grained (Fig. 7), the effect of zirconium does not appear to be due to a major modification of the bulk scale microstructure. However, this result is preliminary; the influence of zirconium on scale and interface characteristics will be investigated in more detail using microscopy and other analytical techniques available at ORNL, ANL and LBL.

For spallation-resistant alloys, there should be little influence of cycle frequency on weight-change measurements unless substantial scale cracking occurs. Therefore, the finding that the measured weight changes of FAL undergoing cyclic oxidation at 1000°C are not frequency dependent (Fig. 8) is consistent with the lack of any observations of spallation or visible scale cracking. On the other hand, because of the spallation susceptibilities of FA129 and FA186, the gravimetric results for these alloys do show a dependence on the number of thermal cycles for a given oxidation period (see, for example, Fig. 3). Most of the scale damage is due to thermal cycling; in Fig. 3, W_o is about the same regardless of whether the first cycle was after 24 or 96 h of exposure.

As mentioned above, the present work represents the initial stage in defining the fundamental correlations among properties, structure, and mechanical reliability of the surface oxides as they relate to corrosion performance. This first step includes determination of the effects of starting alloy microstructure, composition, and surface finish on high-temperature cyclic oxidation behavior and associated scale integrity and spallation susceptibility. The results of this work are being used to prepare suitable thermally grown oxides on iron-aluminum alloys for examination by a variety of characterization techniques, including analytical electron microscopy, SEM observation of cracking behavior using a bending stage, and nanoindentation (to determine elastic and plastic properties as well as fracture toughness). In this regard, the oxidation results described above have important implications for the use of these alloys as model materials for such a comprehensive study of the microstructure and properties of alumina scales. The use of polished (rather than just

ground) surfaces on the specimens of FAL results in a more uniform scale upon oxidation such that these characterization techniques can be facilitated. Furthermore, whereas the scales formed on FA129 with a 600 grit surface finish (Fig. 5a) were wholly unsuitable for such analyses, there appears to be some possibility in obtaining information from the pieces of sound, adherent oxide remaining on polished surfaces of this alloy (see, for example, Fig. 7a). This could be a key part of subsequent study as it may be just as crucial to obtain information from spallation-prone scales (in this case, those formed on FA129 and FA186) as it is for adherent surface oxides (such as those grown on FAL). As such, these results may well prove to be an important step in specifying the microstructural, chemical, and mechanical differences of scales exhibiting different degrees of adherence to their alloy substrates.

The present findings on scale damage resulting from cyclic oxidation represent the traditional way of assessing corrosion performance and the mechanical reliability of scales. Because of this, they provide the means of linking oxidation performance of this system with the results forthcoming from use of the characterization techniques listed above. In addition, this study of alumina scales grown on iron-aluminum alloys will form the basis for comparison with results form similar work with as-deposited alumina on the same substrates.

SUMMARY AND CONCLUSIONS

As a part of the initial effort in defining the fundamental relationships among properties, structure, and mechanical behavior of surface oxides that provide corrosion protection at high temperatures, the integrity of alumina scales formed on iron-aluminum alloys during cyclic oxidation was characterized by gravimetric measurements and microscopy. Specimens with ground or polished surface finishes were prepared from three iron-aluminum compositions. Scales were thermally grown using a series of (typically) 24 h exposures to air at 1000°C. Gravimetric data and scanning electron microscopy revealed little scale damage and substantially better adhesion of the alumina grown on the alloy containing zirconium. Thermal cycling caused extensive disruption and spallation of the scales formed on the other two alloys. Transmission electron microscopy showed that scales grown on spallation-resistant and spallation-susceptible iron-aluminum alloys were both fine-grained. Use of polished (rather than just ground) specimens resulted in scales that were more amenable to characterization.

ACKNOWLEDGMENTS

The authors thank M. Howell for experimental support and J. R. DiStefano, B. A. Pint, and I. G. Wright for their thoughtful reviews of the manuscript. This research was sponsored by the Fossil Energy Advanced Research and Technology Development (AR&TD) Materials Program and the Division of Materials Science, U S. Department of Energy, under contract DE-AC05-84OR21400 with Martin Marietta Energy Systems, Inc.

REFERENCES

1. K. Natesan, "Mechanically Reliable Coatings and Scales for High-Temperature Corrosion Resistance," these proceedings.

2. I. W. Brown, "Plasma Synthesis of Alumina Films on Metal and Ceramic Substrates," these proceedings.

3. P. F. Tortorelli and J. H. DeVan, pp. 257-70 in Processing, Properties, and Applications of Iron Aluminides, J. H. Schneibel and M. A. Crimp (eds.), The Minerals, Metals, and Materials Society, Warrendale, PA, 1994.

4. J. H. DeVan, P. F. Tortorelli, and M. J. Bennett, pp. 309-20 in *Proc. Eighth Annual Conf. Fossil Energy Materials*, N. C. Cole and R. R. Judkins (comp.), CONF-9405143, U. S. Department of Energy, August 1994.

5. J. H. DeVan, P. F. Tortorelli, and U. K. Abdali, "Environmental Effects on Iron Aluminides," pp. 216-226 in *Proc. Sixth Annual Conf. Fossil Energy Materials*, N. C. Cole and R. R. Judkins (comp.), U. S. Department of Energy, July 1992.

6. J. Doychak, pp. 977-1016 in Intermetallic Compounds: Vol. 1, Principles, J. H. Westbrook and R. L. Fleischer (eds.), John Wiley & Sons, New York, 1994.

7. J. A. Horton, Oak Ridge National Laboratory, unpublished results.

WELDING AND MECHANICAL PROPERTIES OF CAST FAPY (Fe-16 at. % Al-BASED) ALLOY SLABS

V. K. Sikka, G. M. Goodwin, D. J. Alexander, and C. R. Howell

INTRODUCTION

The low-aluminum-content iron-aluminum program deals with the development of a Fe-Al alloy with aluminum content such as a produce the minimum environmental effect at room temperature. The FAPY is an Fe-16 at. % Al-based alloy developed at the Oak Ridge National Laboratory as the highest aluminum-containing alloy with essentially no environmental effect.[1] The chemical composition for FAPY in weight percent is: aluminum = 8.46, chromium = 5.50, zirconium = 0.20, carbon = 0.03, molybdenum = 2.00, yttrium = 0.10, and iron = 83.71. The cast ingots of the alloy can be hot worked by extrusion, forging, and rolling processes. The hot-worked cast structure can be cold worked with intermediate anneals at 800°C. Typical room-temperature ductility of the fine-grained wrought structure is 20 to 25% for this alloy. In contrast to the wrought structure, the cast ductility at room temperature is approximately 1% with a transition temperature of approximately 100 to 150°C, above which ductility values exceed 20%. The alloy has been melted and processed into bar, sheet, and foil. The alloy has also been cast into slabs, step-blocks of varying thicknessess, and shapes.

The purpose of this section is to describe the welding response of cast slabs of three different thicknesses of FAPY alloy. Tensile, creep, and Charpy-impact data of the welded plates are also presented.

Discussion of Current Activities

Casting

For the welding studies, the FAPY alloy was used in the as-cast condition, prepared by vacuum-induction melting, and cast in graphite molds measuring 100 by 150 mm (4 by 6 in.) in length and having thicknesses of 12, 25, and 51 mm (0.5, 1, and 2 in.). All three plates had good as-cast surfaces. The welding studies were conducted on the plates in the as-cast condition.

Weld Production

Weld joints were prepared by sawing as shown in Fig. 1. The included angle of 60° in the double-vee groove geometry was used for all three slab thicknesses and is typical of industrial practice for plate welding.

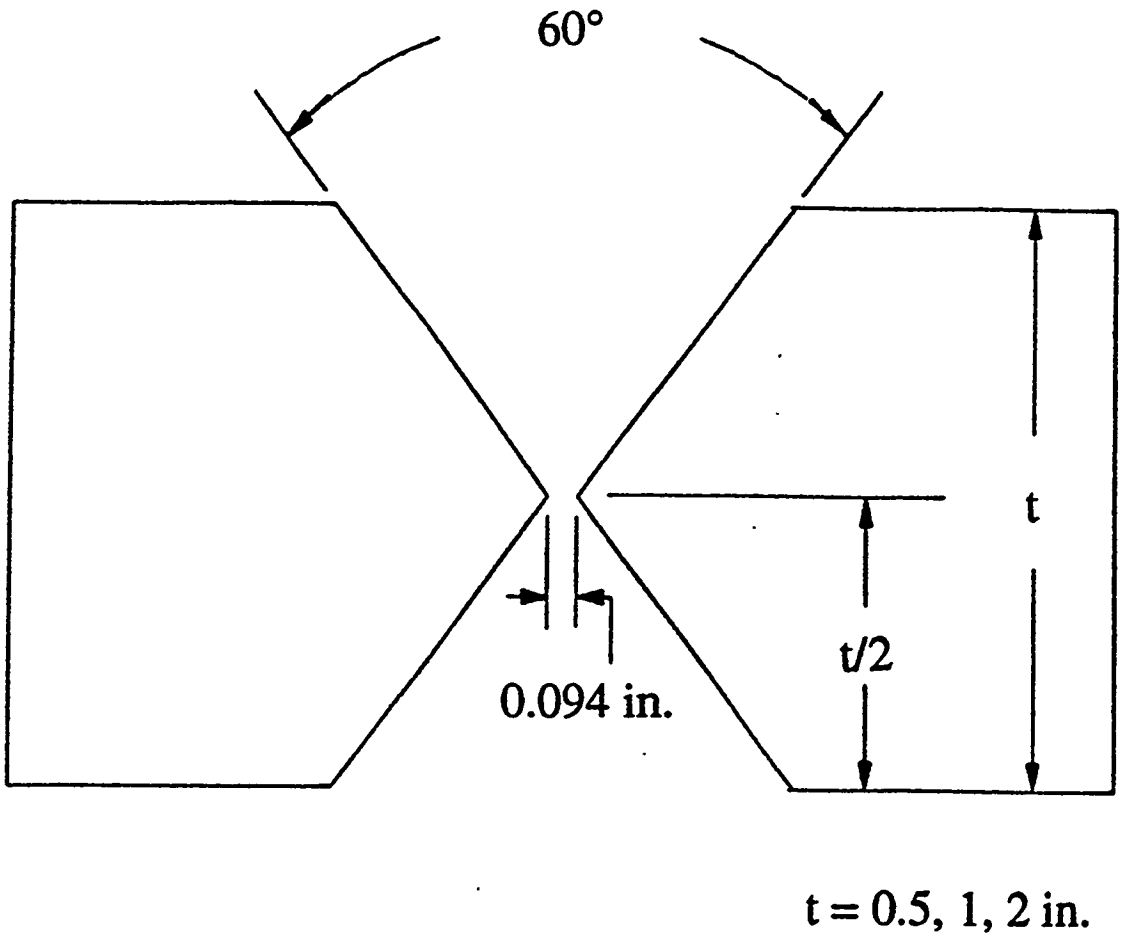

Fig. 1. Joint geometty for FAPY cast slab welds.

Weld wire of 3.2 mm (0.125 in.) diam with a matching composition of FAPY alloy was used for all weldments using the manual gas tungsten arc (GTA) process. The joint surfaces and filler wire were cleaned by wire brushing and solvent degreasing with acetone. A summary of the welding parameters is shown in Table 1.

Preheat, when used, was accomplished with an oxyacetylene torch. Interpass temperature was maintained at 350°C minimum. Postweld heat treatment (PWHT), when used, was done immediately following welding in an air furnace followed by free cooling in still air.

Table 1. Welding parameters for cast FAPY alloy slabs

Process:	Manual gas tungsten arc
Joint geometry:	Double-vee groove, 60° included angle
Base metal:	Cast slabs [100 ¥ 150 ¥ 12, 15, and 51 mm (4 × 6 × 0.5, 1, and 2 in.) thicknesses]
Filler metal:	3.2-mm (0.125 in.) -diam rod, matching composition
Weld current:	100 to 175 A direct current electrode negative
Weld voltage:	10 to 12 V
Torch gas:	Argon, 15 cfh (7.1 L/min)
Backing gas:	Argon, 15 cfh (7.1 L/min)
Approximate number of passes (alternating sides):	12-mm (0.5-in.) slab: 6 25-mm (1-in.) slab: 25 51-mm (2-in.) slab: 65

Completed weldments were examined for possible defects using liquid-dye penetrant. A summary of the inspection results is shown in Table 2. End sections were removed from each weldment for optical metallography.

Table 2. Inspection results of cast FAPY alloy slab welds

Temperature, °C		Slab thickness, mm (in.)		
Preheat	Postheat	12 (0.5)	25 (1)	51 (2)
350	750	No cracks	No cracks	No cracks
200	750	--	--	No cracks
20	20	No cracks	Cracks	--

Mechanical Properties

The welded slabs were cut up for mechanical property determinations. The 12-mm (0.5-in.) -thick plates were used for Charpy-impact testing. The 25- and 51-mm (1- and 2-in.) -thick plates were used for tensile and creep properties. The specimen cut-up diagrams for the Charpy, tensile, and creep specimens are shown in Fig. 2.

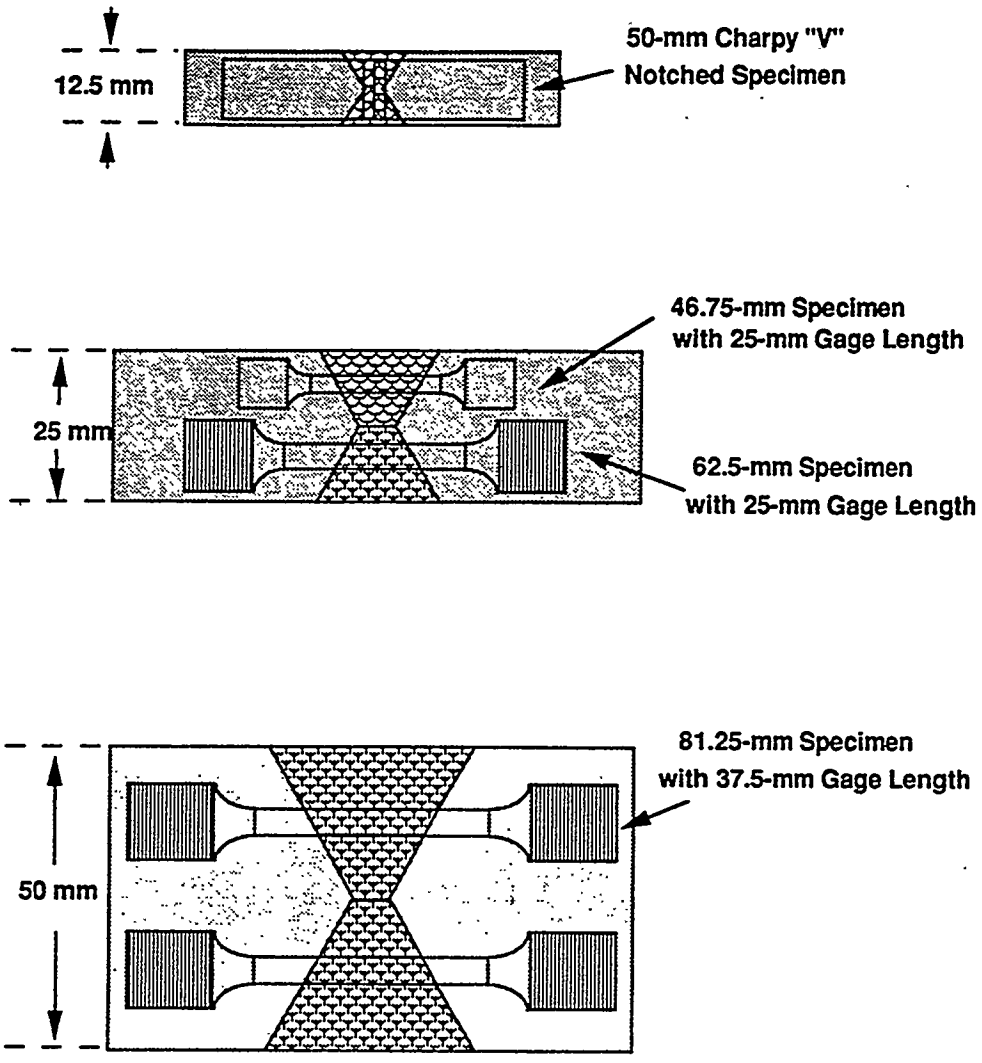

Fig. 2. Schematic showing the location and size of mechanical property specimens machined from welded slabs of FAPY alloy.

Tensile Properties

The tensile data from room temperature to 800°C for the 25- and 51-mm (1- and 2-in.) -thick welded plates are summarized in Table 3. The strength and ductility data of the weldments are plotted and compared with the base-metal data of the cast slabs in Figs. 3 through 6. The following observations are possible from these figures:

1. The 0.2% yield strength of the weldment specimens is essentially the same as the base-metal values for the entire temperature range. This is true for specimens taken from both the 25- and 51-mm (1- and 2-in.) -thick welded plates.

Table 3. Tensile properties of weldment specimens machined from the cast-welded 25- and 51-mm (1- and 2-in.) -thick slabs of FAPY alloy

Specimen No.	Test temperature (°C)	Heat-treatment temperature (°C)		Yield strength (MPa)	Tensile strength (MPa)	Total elongation (%)	Reduction of area (%)
		Preheat	Postheat[a]				
1L[b]	23	350	750	70.91	70.91	1.79	0.08
2L[b]	100	350	750	60.31	79.81	22.88	32.53
3L[b]	200	350	750	47.91	75.07	24.32	44.38
4L[b]	400	350	750	41.19	76.78	25.58	42.89
5L[b]	600	350	750	39.26	39.50	46.16	74.71
6L[b]	800	350	750	11.82	12.22	78.24	83.80
11L[c]	23	200	750	65.39	65.39	0.91	0.00
12L[c]	50	200	750	64.43	65.14	1.62	0.40
13L[c]	100	200	750	57.09	73.77	9.20	9.28
14L[c]	200	200	750	45.36	71.94	20.46	50.37
15L[c]	400	200	750	37.04	73.36	26.35	41.20
16L[c]	600	200	750	37.81	38.93	43.74	72.05
17L[c]	800	200	750	--	11.53	64.13	80.37

[a]Time at temperature: 1 h.
[b]Specimen gauge length: 25 mm (1 in.); strain rate: 3.3×10^{-3}/s.
[c]Specimen gauge length: 51 mm (2 in.); strain rate: 2.2×10^{-3}/s.

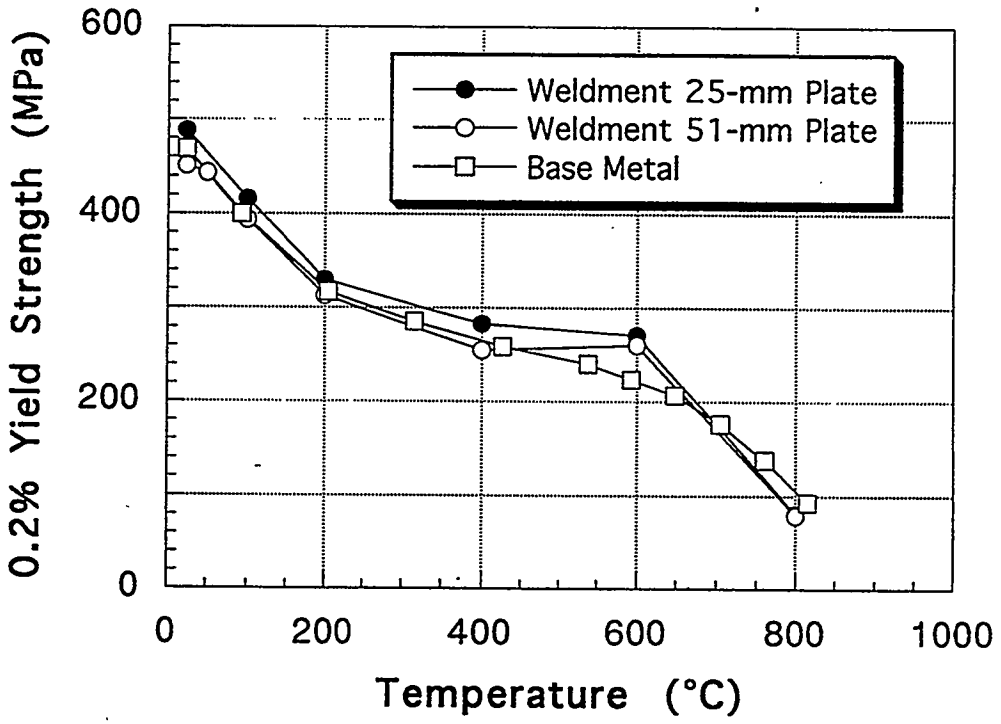

Fig. 3. Comparison of 0.2% yield strength of weldment specimens with base metal of FAPY alloy. The base-metal data are from a previous study on cast slab.

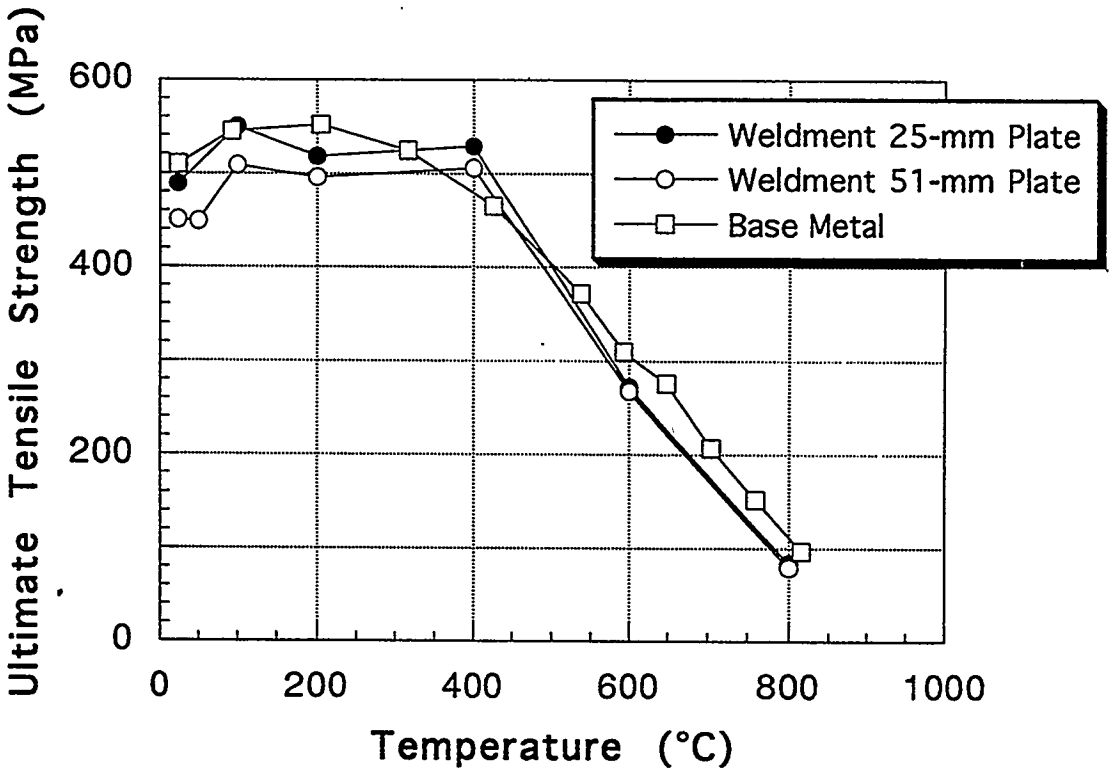

Fig. 4. Comparison of ultimate tensile strength of weldment specimens with base metal of FAPY alloy. The base-metal data are from a previous study on cast slab.

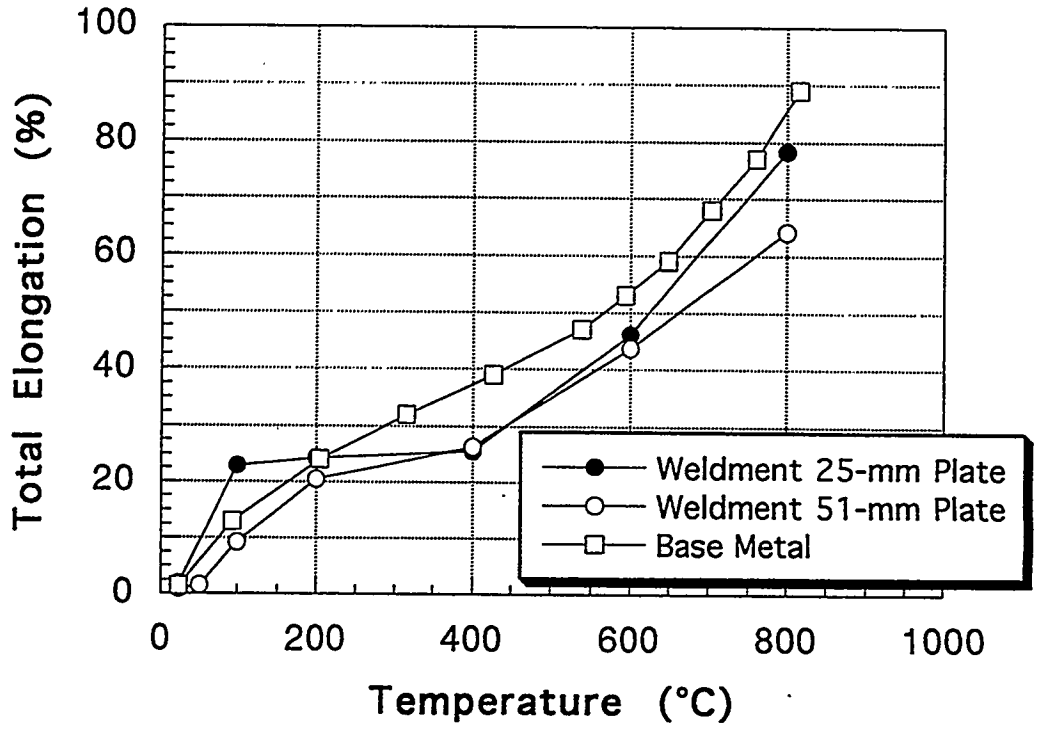

Fig. 5. Comparison of total elongation of weldment specimens with base metal of FAPY alloy. The base-metal data are from a previous study on cast slab.

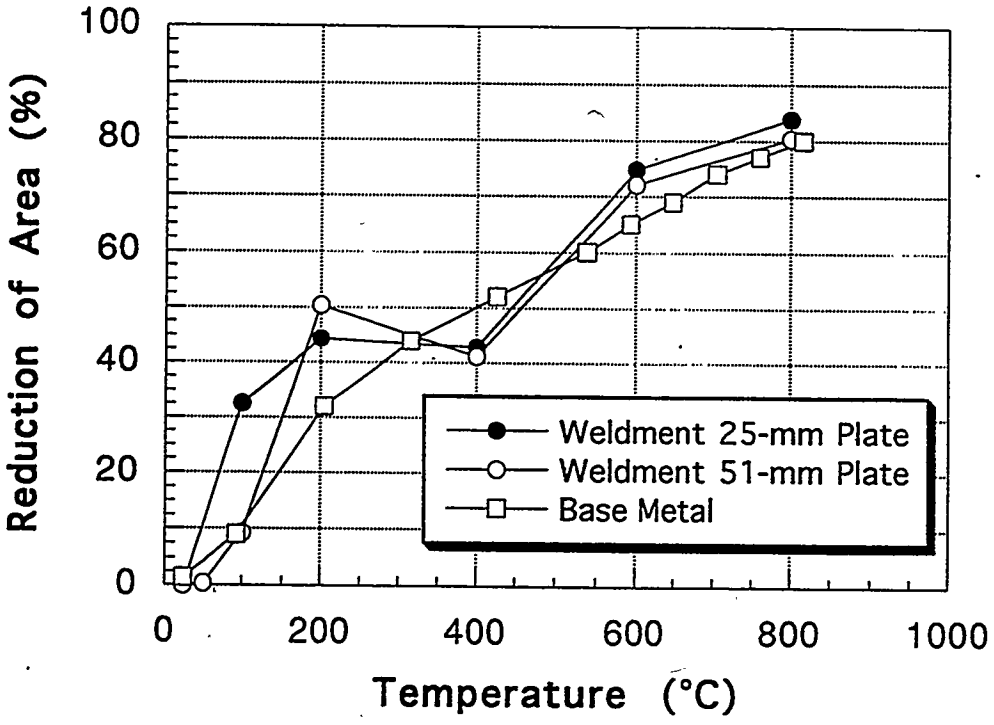

Fig. 6. Comparison of reduction of area of weldment specimens with base metal of FAPY alloy. The base-metal data are from a previous study on cast slab.

2. The ultimate tensile strength of the weldment specimens from the 51-mm (2-in.) -thick plate showed lower values than the base metal in the test-temperature range up to 200°C. This is the same temperature region where ductility of both base metal and weldments is low (see Figs. 5 and 6). The observed results in Fig. 4 imply that the weldment specimens from the 51-mm (2-in.) -thick plates are slightly more brittle in this temperature range than base metal or 25-mm (1-in.) -thick plate.
3. The general trend of total elongation and reduction of area of weldments is the same as that for the base metal (see Figs. 5 and 6).

Creep Properties

The creep data on three weldment specimens machined from 25-mm (1-in.) -thick welded plate are summarized in Table 4. The creep-rupture data on the weldment specimens are compared with the previously developed data on as-cast and wrought base-metal specimens in Fig. 7 which shows that although limited in number, the short-term data on weldment specimens match the data on base-metal, as-cast, and wrought specimens. It should be recognized that long-term data are required to further confirm these observations.

Table 4. Creep properties of weldment specimens*a* machined from the cast-welded 25-mm (1-in.) -thick slab of FAPY alloy

Test No.	Specimen No.	Test temperature (°C)	Stress (MPa)	Time to rupture (h)	Rupture elongation (%)	Reduction of area (%)	Creep rate (%/h)
28312	7L	550	207	2.2	19.20	64.94	--
28321	8L	600	138	2.8	30.38	67.08	--
28314	9L	650	69	13.6	55.96	75.89	--
28313	10L	700	21.69	1389.3	48.90	85.90	--

[a]Weldment prepared with a preheat of 350°C and a postweld heat treatment at 750°C for 1 h.

Charpy-Impact Tests

Full-size Charpy-impact specimens were machined from two welded plates of 12 mm (0.5 in.) thickness. One of the plates contained a weld in the as-welded condition, and the other one was given a PWHT at 750°C for 1 h. The schematic in Fig. 2 shows the cut-up schedule for the Charpy specimens. The crack growth was parallel to the welding direction (T-L orientation). The specimens were tested on a 325-J capacity impact tester, and the data are summarized in

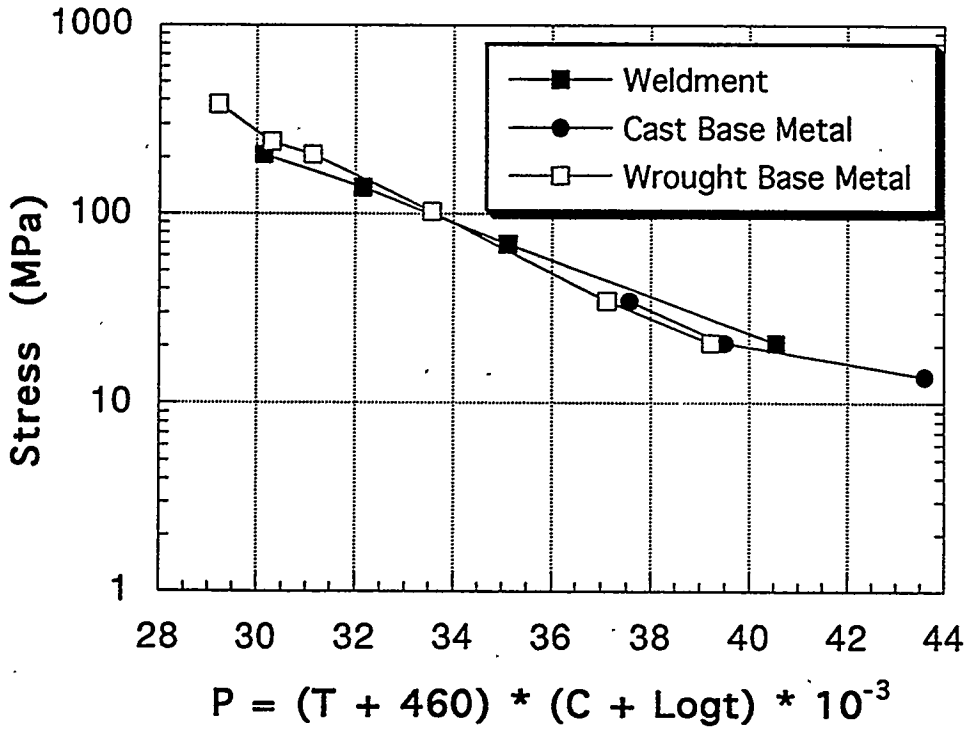

Fig. 7. Comparison of creep rupture properties of weldment specimens with the as-cast and wrought base-metal specimens.

Table 5. The data, plotted in Fig. 8, were fitted with a hyperbolic tangent function. The lower-shelf energy was fixed at 2 J and the upper-shelf energy was fixed at the value of the test at 400°C for each set of specimens (122 J for the as-welded specimens, 144 J for the postweld heat-treated specimens).

The results show that the PWHT does improve the toughness of the material. The ductile-to-brittle transition temperature, defined at an energy level midway between the upper- and lower-shelf energy levels, decreases from 245°C for the as-welded material to 200°C for the material that was given the postweld heat treatment, a 45°C improvement. The transition temperature is still quite high however. The upper-shelf energy also improves with heat treatment, increasing from 122 to 144 J. The specimens tested at 400°C showed completely ductile fracture, and they provide a good estimate of the upper-shelf energy, although only one specimen was tested for each material at high enough temperatures to give fully ductile fracture.

Table 5. Charpy-impact energy data on weldment specimens from 12-mm (0.5-in.) -thick plate of FAPY alloy

Test temperature (°C)	Charpy-impact energy			
	As welded		Postweld heat treated[a]	
	J	ft/lb	J	ft/lb
25	2	1.5	2.6	1.9
100	5.4	4.0	5.3	3.9
150	9.5	7.0	9.2	6.8
175	--	--	20.3	15.0
200	20.3	15.0	72.5	53.5
250	71.2	52.5	--	--
300	100.3	74.0	126.1	93.0
400	122.0	90.0	143.7	106.0

[a]Postweld heat treatment at 750°C for 1 h.

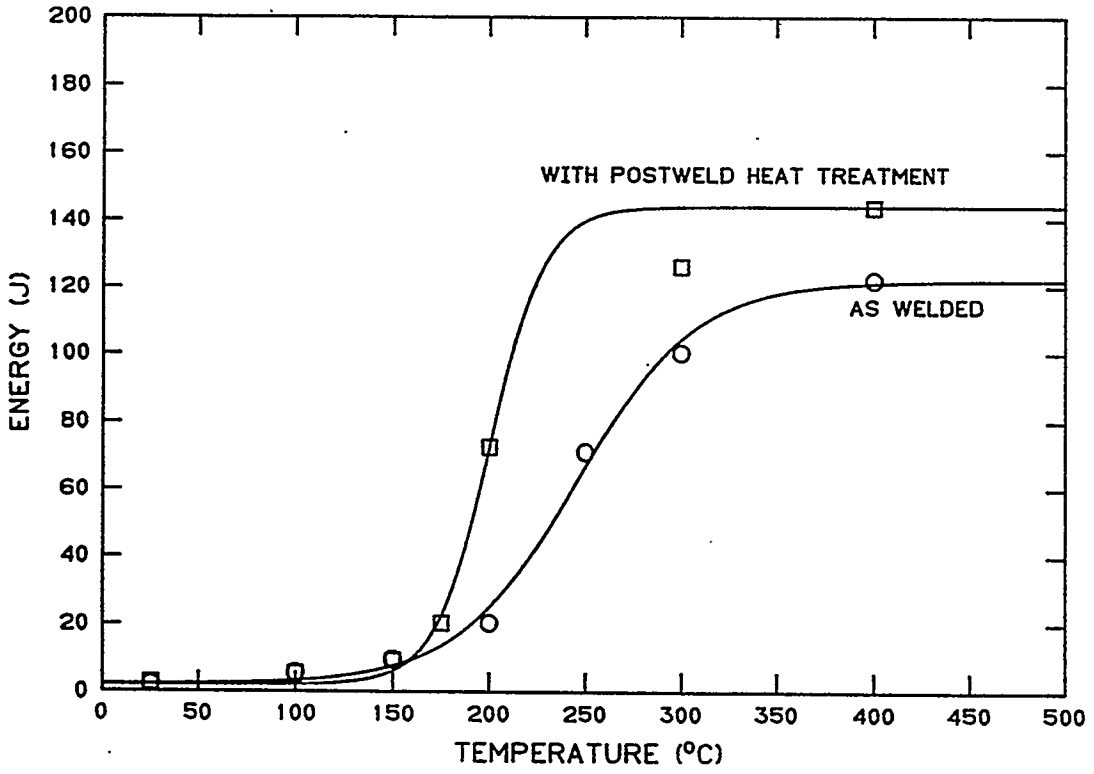

Fig. 8. Plot of Charpy-impact energy of weldment specimens from 12-mm- (0.5-in.-) thick cast plate of FAPY alloy. Postweld heat treatment was carried out at 750°C for 1 h.

The Charpy-impact energy data for the weldment specimens are compared with that of the wrought base-metal data in Fig. 9. This figure shows that the transition temperature is approximately 50° higher for the weldment specimens, and the upper-shelf energy is lower by approximately 100 J. The most likely cause for the higher transition temperature for the weldment specimens is their much coarser grain size as opposed to the wrought material.

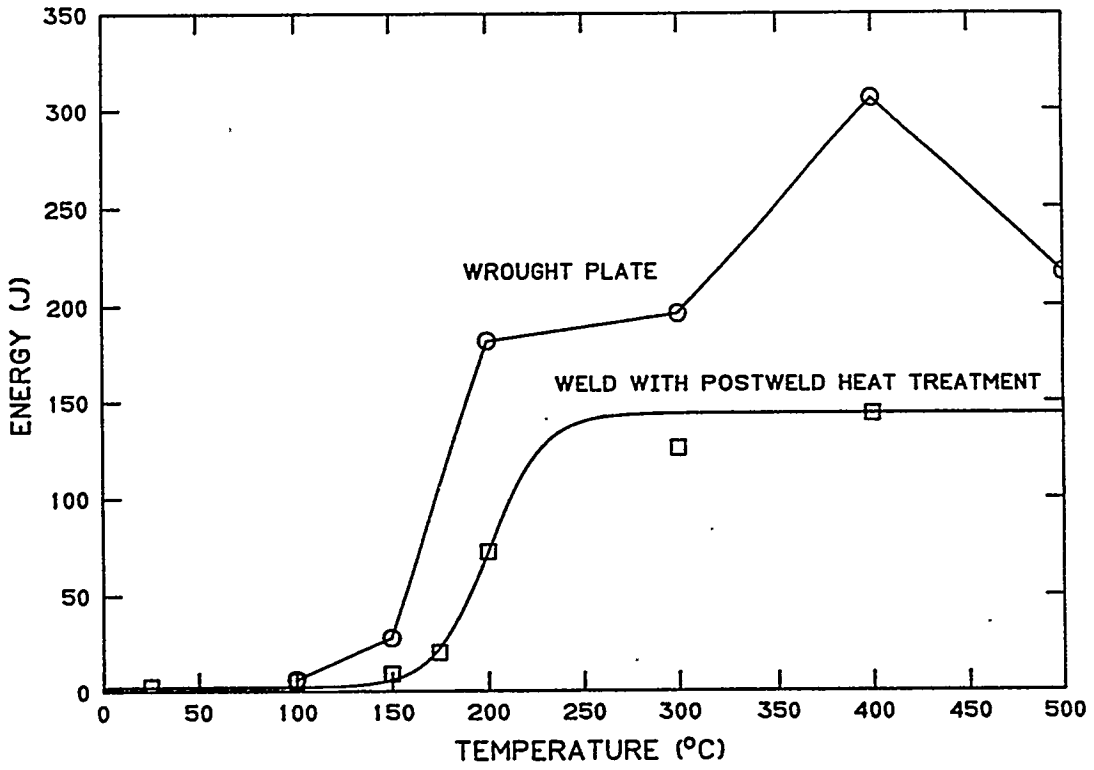

Fig. 9. Comparison of Charpy-impact energy data of weldment specimens with that of base-metal specimens in the wrought condition.

Microstructure and Hardness Data

In addition to the macroetched cross sections, photomicrographs of various regions of the weldment were also taken. The general observations from the weldment photomicrographs are: (1) the weld metal showed a coarse-grained structure similar to the cast base metal, and (2) the region identified as HAZ had an epitaxial grain growth of the base-metal grains into the weld metal.

The microhardness data of the base-metal, HAZ, and weld-metal regions show that they are essentially the same for plates of a given thickness (see Table 6). However, there is approximately a 10- to 20-dph point increase in hardness of thicker plates as opposed to a 12-mm (0.5-in.) -thick plate.

Table 6. Microhardness of base, weld, and heat-affected zone of welds in 12-, 25-, and 51-mm (0.5-, 1-, and 2-in.) -thick welded plates in the as-cast condition

Plate thickness (mm)	Microhardness (dph)			
	Base metal	Weld metal	Heat-affected zone	Base metal and heat-affected zone in unusual area
12	223 ± 4	227 ± 5	223 ± 7	--
25	238 ± 4	237 ± 6	243 ± 3	246 ± 6
51	233 ± 10	252 ± 7	238 ± 4	240 ± 11

DISCUSSION

The vacuum-induction-melted and as-cast plates of 12, 25, and 51 mm (0.5, 1, 2 in.) thicknesses were successfully welded using the GTA process. All of the welds used a filler wire of base-metal composition. The 12-mm (0.5-in.) -thick plate could be welded without a preheat. However, 25 mm (1 in.) and thicker sections required a preheat to make crack-free welds. The preheat temperature for the FAPY alloy can be as low as 200°C, which is no different than that required for most of the ferritic steels. In addition to preheat, a PWHT of 750°C is highly desirable for lowering the transition temperature and increasing the upper-shelf energy during Charpy-impact testing.

The microstructure of the starting plates was coarse due to being in the as-cast condition. For the thinner plate of 12 mm (0.5 in.) thickness, the grain structure was primarily columnar. However, for the plates of 25 and 51 mm (1 and 2 in.) thicknesses, some equiaxed structure was also present in addition to the columnar structure. The weld region also showed a coarse-grained microstructure similar to the cast structure of the base metal. Indications of epitaxial growth of base-metal grains into the weld region were observed. No distinct transition in microstructure was observed from the base- to the weld-metal regions. This observation was confirmed by noting essentially the same microhardness values for base-metal, HAZ, and the weld-metal region. The uniformity in microstructure and microhardness was also confirmed by the failure of

the tensile specimens in the middle of the gage section, which normally happens for a material of uniform properties.

The similarity in microstructure and microhardness of the base and weld metals yielded tensile properties of the weldment specimens to match the base-metal properties. A similar match was also observed for the creep-rupture properties. It is important to note that although the properties of the weldment specimens matched the base-metal properties in the as-cast condition, the ductility values for FAPY alloy are too low at temperatures ≤ 100°C.

An unusual event of cracking was observed in this weldment section of the 51-mm- (2-in.-) thick plate during the etching process to reveal its macrostructure. The acid-etching process is known to produce hydrogen, and it is this hydrogen that is believed to have caused the cracking. This cracking was observed only in the 51-mm (2-in.) -thick plate and not in the plates of 12 and 25 mm (0.5 and 1 in.) thicknesses. Since the hydrogen-related cracking typically requires the combination of stress and the presence of hydrogen, it is believed that a PWHT of 750°C was not adequate to relieve the welding stresses for the 51-mm (2-in.) -thick plate. However, the same PWHT must have been adequate for the thinner sections, which had lower welding stresses to start with because of their thinner sections. Thus, it is believed that a higher PWHT temperature than 750°C may be required for section sizes of ≥ 51 mm (2 in.). Additional work is required to establish the PWHT requirements as a function of section thickness for the FAPY alloy.

SUMMARY AND CONCLUSIONS

The as-cast plates of 12, 25, and 51 mm (0.5, 1, and 2 in.) thicknesses of FAPY alloy were welded using the GTA process and a 3-mm (0.125-in.) -diam filler wire of matching composition. Welds were made without any preheat and with preheats of 200 and 300°C. The crack-free welds could be prepared in 12-mm (0.5-in.) -thick plates. However, the thicker plates required a preheat for crack-free welds, and a temperature of 200°C was acceptable up to plate thickness of 51 mm (2 in.). The preheat temperature for thicker sections may be higher and needs to be determined. The PWHT at 750°C for 1 h was found to lower the transition temperature and increase the upper-shelf energy during Charpy-impact testing of the 12-mm- (0.5-in.-) thick welded plate. Thus, all the other weldment properties were determined in the postweld heat-treated condition. Tensile and creep properties of the weldment specimens matched the properties of the base metal. These results were explained on the basis that the microstructure and microhardness of the weld region were similar to the base metal.

Major conclusions from this study include:

1. The cast plates of the FAPY alloy can be welded by a commonly used GTA process. A filler wire of composition matching the base metal is acceptable. No preheat is required for plates of 12 mm (0.5 in.) thickness. Plates of ≥ 25 mm (1 in.) thickness require a preheat of at least 200°C. A PWHT at 750°C for 1 h is desirable to improve the Charpy-impact properties and to reduce the suceptibility of the weld to hydrogen-related cracking. A PWHT temperature of higher than 750°C is probably required to eliminate the hydrogen-related cracking in the 51-mm- (2-in.-) thick welds. However, a correlation of PWHT as a function of section thickness needs to be developed.
2. Tensile and creep properties of the weldment specimens matched that of the base metal. These results are explained on the basis that the microhardness and microstructure of the welds are very similar to the base metal.

FUTURE WORK

Additional work is required on welding of thicker sections of the FAPY alloy:

1. Prepare welds in a section thickness greater than 51 mm (2 in.), and determine the PWHT temperatures to eliminate hydrogen-related cracking. Macroetching solution can be used to determine the presence of hydrogen-related cracking.
2. Determine the effect of PWHT temperature on Charpy-impact properties. Use these data to select the optimum temperature for the best combination of transition temperature and upper-shelf energy.
3. Determine additional weldment creep tests to obtain data for rupture times exceeding 1000 h.

REFERENCES

1. S. Vyas, S. Viswanathan, and V. K. Sikka, "Effect of Aluminum Content on Environmental Embrittlement in Binary Iron-Aluminum Alloys," *Scr. Metall. Mater.* **27**, 185-190 (1992).

THE INFLUENCE OF PROCESSING ON MICROSTRUCTURE AND PROPERTIES OF IRON ALUMINIDES

R. N. Wright and J. K. Wright

Idaho National Engineering Laboratory
Lockheed Idaho Technologies Company
Idaho Falls, ID 83415-2218

ABSTRACT

An Fe-28%Al alloy containing 5% Cr has been synthesized by reaction of elemental powders, followed by consolidation using hot isostatic pressing or hot extrusion. The resulting materials are fully dense, homogeneous, and have a grain size of less than 5μm. Processing strongly influences the propensity toward secondary recrystallization. While HIPped material is extremely resistant to grain growth, under some circumstances hot extruded material undergoes secondary recrystallization, resulting in grain sizes as large as 25 millimeters. Elevated temperature tensile properties and strain rate sensitivities are reported for fine and very coarse grained materials. Grain boundary sliding is not a significant deformation mode for any of the materials. The properties are compared to those of Fe_3Al processed from conventional hot extruded prealloyed powder. It has been found that the reaction synthesized materials generally have superior elevated temperature tensile strength.

INTRODUCTION

Recent work indicates the problem of limited ductility exhibited by Fe_3Al may be overcome by small additions (2-5 wt%) of chromium (1). Tensile elongations for Fe_3Al + 5% Cr are found to approach 20% with little sacrifice in resistance to oxidation and sulfidation (2). Unfortunately, the yield strength of Fe_3Al rapidly decreases above 500°C, thereby reducing the suitability of this material for high temperature applications (2). Nickel-based materials, suffering from a similar decrease in high temperature strength, are strengthened through the incorporation of oxide particles (oxide-dispersion-strengthened or ODS alloys). The oxide particles impede dislocation motion and prevent grain boundary sliding, thus increasing the high temperature strength and creep resistance of these alloys (3). Since the oxide dispersion affects the mechanisms of deformation, a similar improvement in high temperature strength is expected by incorporating an oxide dispersion into Fe_3Al.

This work reports the high temperature mechanical properties of fully dense Fe_3Al, produced by reaction synthesis from elemental powders followed by hot extrusion, and examines the influence of a dispersion of oxide particles on the observed increase in high temperature strength. In this work, the surface oxide coating the elemental powders prior to reaction synthesis provides the desired dispersion of oxide particles in the processed material. The results are compared to Fe_3Al lacking a dispersion of oxide

particles, processed by hot extrusion of pre-alloyed powders. High temperature characterization of the various materials includes grain growth studies, as well as the determination of their high temperature mechanical properties.

EXPERIMENTAL PROCEDURE

Reaction synthesized material was made using carbonyl iron (8 μm diameter), helium gas atomized aluminum (10 μm diameter) and chromium (1-5 μm diameter) powders, mixed in the proper portions to yield Fe-28%Al-5%Cr. Reaction between the elemental powders occurred during a 2 hour thermal treatment at 1100°C in flowing argon. After canning in mild steel, full density rod was produced by hot extrusion (9:1 reduction in area) at extrusion temperatures of 900°C and 1100°C. Fully dense material was also fabricated by hot isostatic pressing a pre-reacted compact at 207 MPa and 1100°C for 2 hours. Consolidated material lacking an oxide dispersion was produced via extrusion of pre-alloyed powder of composition Fe_3Al + 5%Cr made by gas atomization. Extrusion of this material was carried out at 1000°C with a 9:1 reduction in area.

Grain growth experiments were performed during one hour heat treatments in flowing argon at various temperatures. The mean grain size was determined by the linear intercept method on photomicrographs taken of polished and etched samples. Mechanical properties were evaluated during elevated temperature tensile tests. Round cross section tensile bars, machined by centerless grinding from a portion of each of the materials, were tested in tension at various temperatures in laboratory air. In addition, strain rate jump tests were performed on some tensile specimens to measure the strain rate sensitivity at temperatures of 500, 800, and 900°C. Strain rates for these tests ranged from approximately 10^{-4} to $4x10^{-2}$ s^{-1} and each jump approximately doubled the nominal strain rate.

RESULTS AND DISCUSSION

Figure 1 shows an example of the distribution of particles in the HIPped material, obtained using transmission electron microscopy (TEM). The strain imparted to a preform during HIPping is relatively homogeneous, leaving the distribution of inclusions relatively unchanged from the configuration produced by reaction synthesis. The inclusions appear to originate at the surfaces of individual powder particles and are expected to be largely aluminum-rich oxides, which has been confirmed in a previous study (4). The iron oxide on the elemental iron particles is reduced to iron by the aluminum during the reaction (5); the oxygen available from this reduction reacts to form Al_2O_3.

Extrusion causes extensive deformation to the preform, forming the stringers of particles seen in Figure 2a. Electron diffraction from larger particles indicates their crystal structure to be α-alumina. Qualitative energy dispersive spectroscopy (EDS) reveals the particles are also aluminum-rich, supporting the identification of the particles as α-Al_2O_3. However, it should be noted that EDS and Auger spectroscopy also show the particles to contain small amounts of chromium and possibly iron. Heat treatment of the extruded material at 1300°C for one hour leads to significant coarsening of the oxide particles. Small particles, like those seen in Figure 2a, show considerable growth, as seen in Figure 2b.

Fig. 1. TEM micrograph of HIPped material showing distribution of dispersoid.

The dependence of grain size, measured normal to the extrusion direction, on annealing temperature is shown in Figure 3. The grain size remains relatively constant for one hour anneals below 800°C, regardless of extrusion temperature. Between 800°C and 900°C, the material extruded at 1100°C undergoes extensive grain growth; while the material extruded at 900°C shows a dramatic increase in grain size after annealing above 1100°C. Grain growth parallel to the extrusion direction shows trends similar to those shown in Figure 3, however, the grain sizes in that direction are much larger. It can be seen from Figure 4, an optical micrograph of material extruded at 900°C and heat treated at 1300°, that the grains extend through the entire 25 mm long sample, therefore, an accurate measure of the grain size has not been determined. The material extruded at 1100°C exhibits a maximum grain size in the extrusion direction of approximately 800 μm.

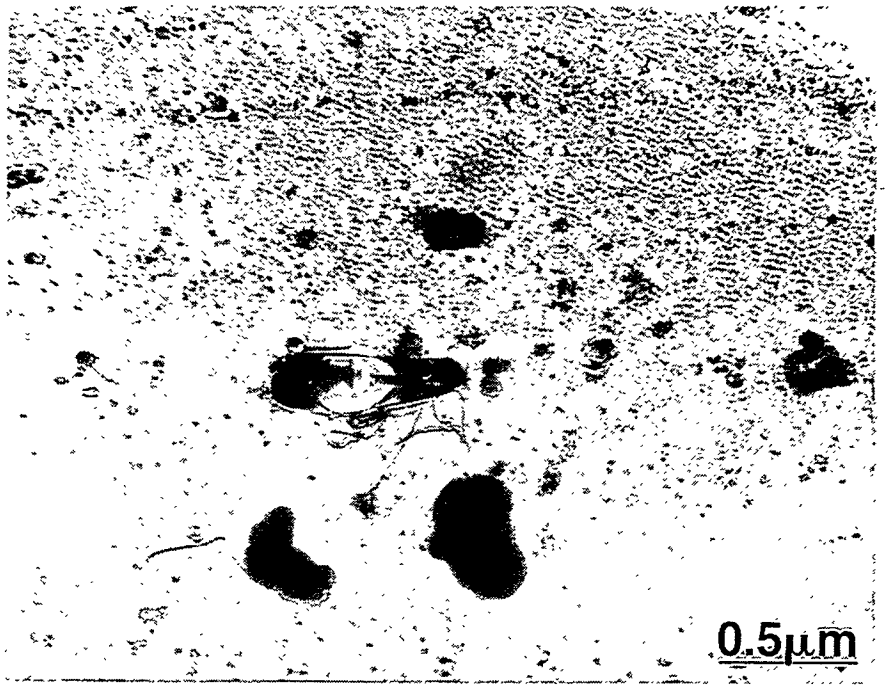

(a)

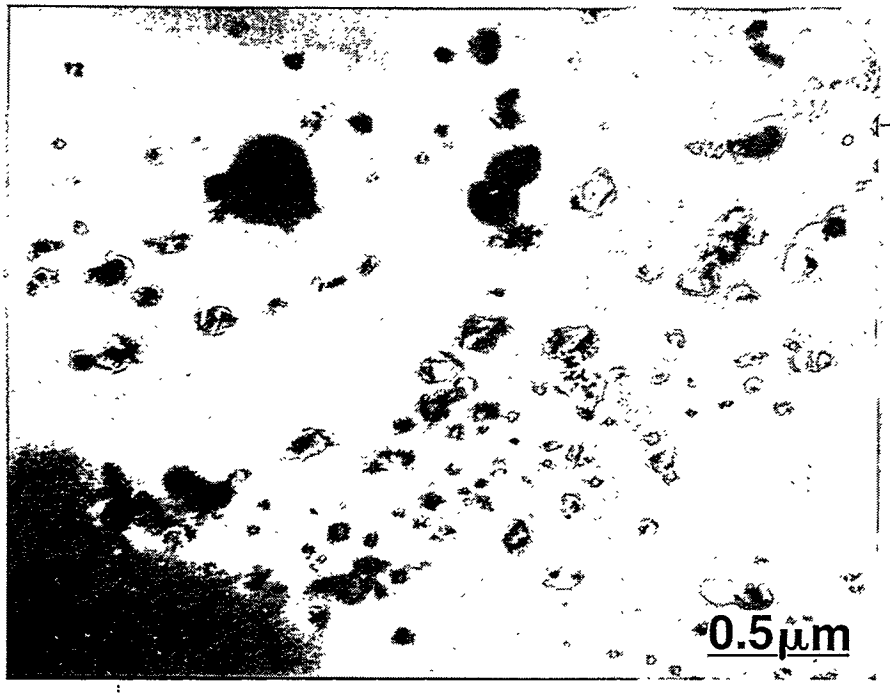

(b)

Fig. 2. TEM micrographs showing (a) stringers of oxide particles in extruded material after 1 hour at 1000°C and (b) increase in particle size after a 1 hour at 1300°C.

The observed grain growth at high temperatures is secondary recrystallization since primary recrystallization is already complete following the one hour anneal at 700°C for either extrusion temperature. A TEM micrograph showing recrystallization after annealing at 700°C is shown in Figure 5. Furthermore, the grain size at higher annealing temperatures remains virtually unchanged after the initial rapid grain growth, behavior characteristic of material having undergone secondary recrystallization (6). The extruded pre-alloyed powder material retains a stable grain size of approximately 50 μm for the annealing temperatures used in this study. Thus, secondary recrystallization appears to be absent in the pre-alloyed material, as well as the HIPped reaction synthesized material where only minor grain growth observed at the annealing temperatures studied.

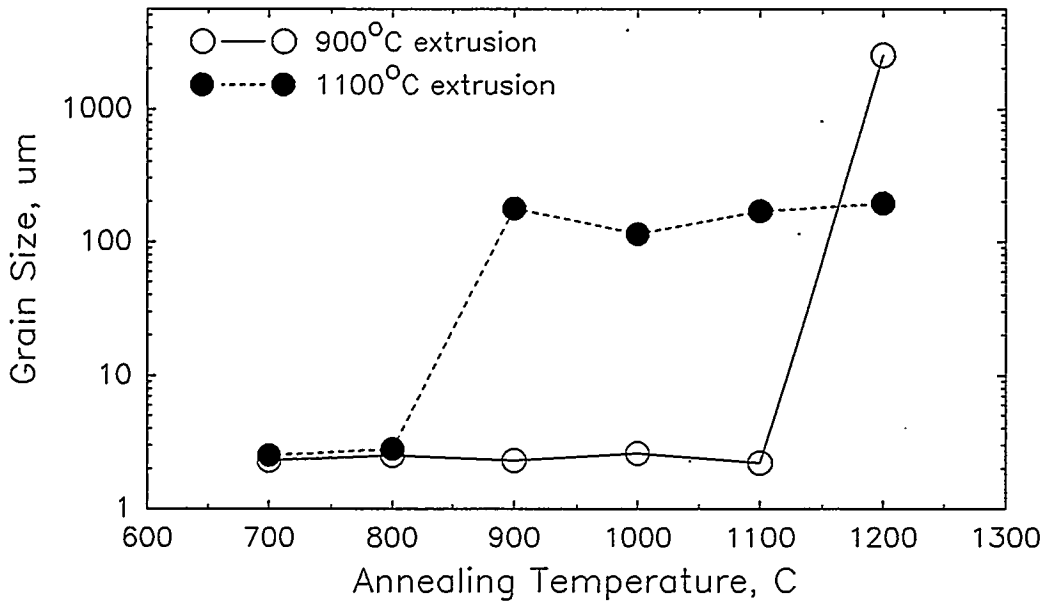

Fig. 3. Effects of annealing on grain size normal to the extrusion direction.

The annealing behavior of the materials in the current study is similar to that of oxide dispersion strengthened nickel (6). Ni-based materials experience severe grain growth at high temperature as a few grains with high mobility boundaries break away from pinning particles and grow rapidly, driven by the reduction in total grain boundary area. The final grain size after secondary recrystallization is determined by the density of nuclei with high boundary mobility (6). Therefore, the exact nature of the annealing response in the Ni-based materials is a function of the processing history, volume fraction of dispersoid and annealing schedule, and is consistent with the behavior of the material used in this study (6).

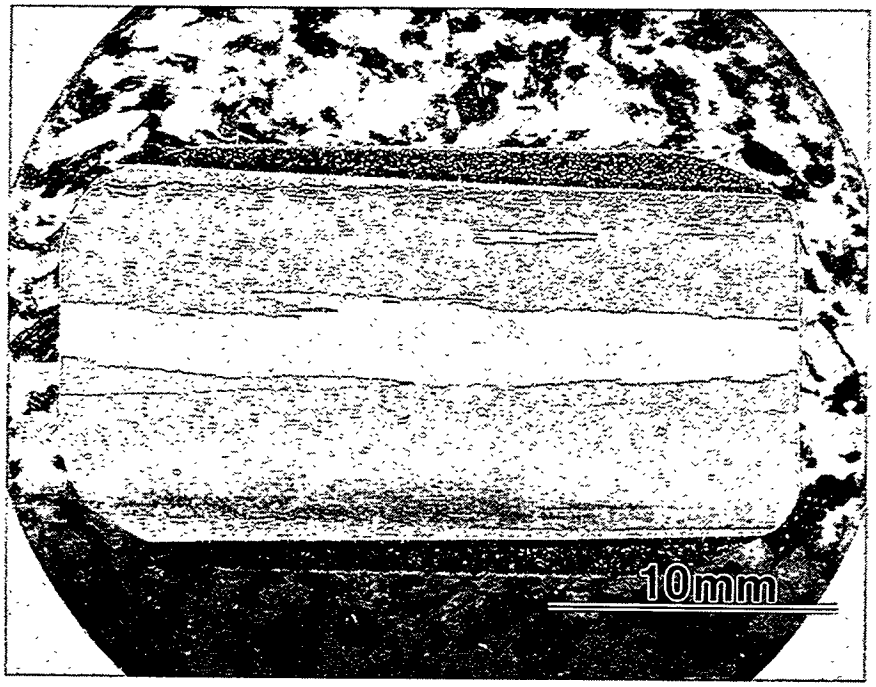

Fig. 4. Optical micrograph of material extruded at 900°C and annealed at 1300°C.

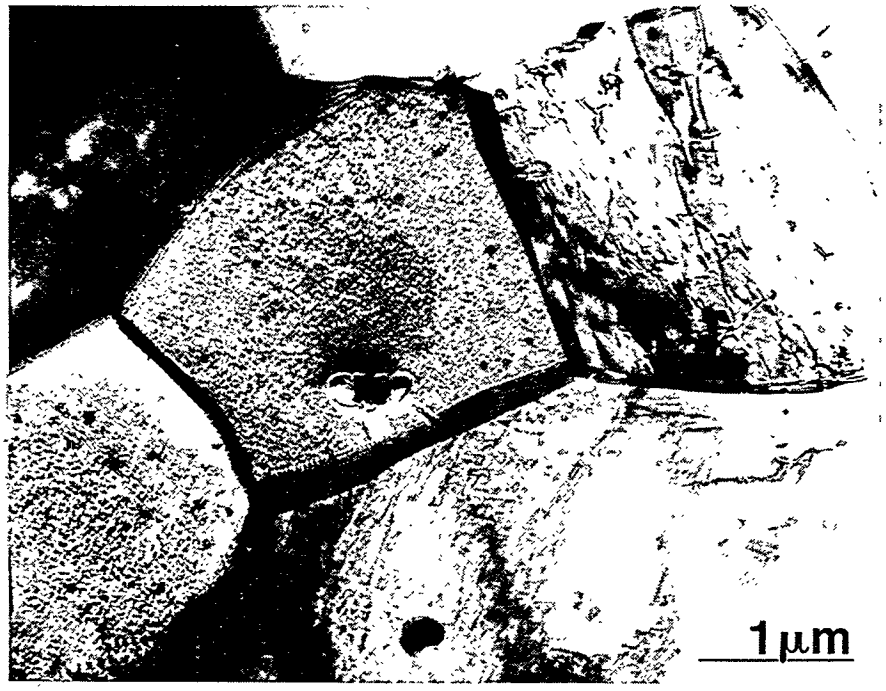

Fig. 5. TEM micrograph of extruded material after annealing 1-hr at 700°C.

Detailed determination of the mechanisms responsible for the unusual grain growth of extruded reaction synthesized material remains under investigation. An analysis by Hillert (7) suggests three conditions are necessary for secondary recrystallization to be observed:

1. Second phase particles prevent normal grain growth.
2. The average grain size cannot exceed a critical value which is determined by dispersoid size and volume fraction.
3. At least one grain much larger than the average grain size must be present.

It has been shown previously that the reaction synthesized material has a critical grain size of about 7 μm (4). Since all of the reaction synthesized materials have approximately the same grain size after primary recrystallization, and all of the grain sizes are below the critical value, it appears differences observed in the tendency to undergo secondary recrystallization are a result of differences in grain shape, texture, and/or the distribution of dispersoid.

Evaluation of the mechanical properties of the reaction synthesized material reveals the oxide dispersion significantly influences the high temperature behavior of chromium-modified Fe_3Al. Figure 6a shows the yield strength of the fine grained ODS alloy to be nearly doubled over that of the pre-alloyed P/M material. The effect appears most dramatic at room temperature; however, the increment of strengthening has been retained at 800°C where the ODS material is still twice as strong despite severely diminished strength for both materials. The 2.7 μm grained material is strongest at all test temperatures while retaining room temperature ductility of approximately 2%; however the yield strengths of the 113 and 1000 μm grained materials do not vary significantly from one another.

The component of strengthening resulting from grain size effects can be seen more clearly from Figure 6b. The grain size and yield strength of HIPped and extruded reaction synthesized material have been plotted along with those from Ceracon consolidated material tested in a previous study (2), and suggests standard Hall-Petch behavior of:

$$\sigma = \sigma_o + kd^{-\frac{1}{2}}$$

where σ_o = 473 MPa and k = 925 MPa $\mu m^{1/2}$. A particle strengthening component of 240 MPa is indicated by the data point (filled) for pre-alloyed material, which should fall on the line of Figure 4b if all strengthening was the result of grain refinement.

In contrast to the yield strength, the strain-rate sensitivity measured at 900°C is not significantly affected by grain size (Figure 7). In addition, the strain rate sensitivity values observed are less than about 0.2 which is relatively low; typically values above 0.5 are characteristic of superplastic materials.

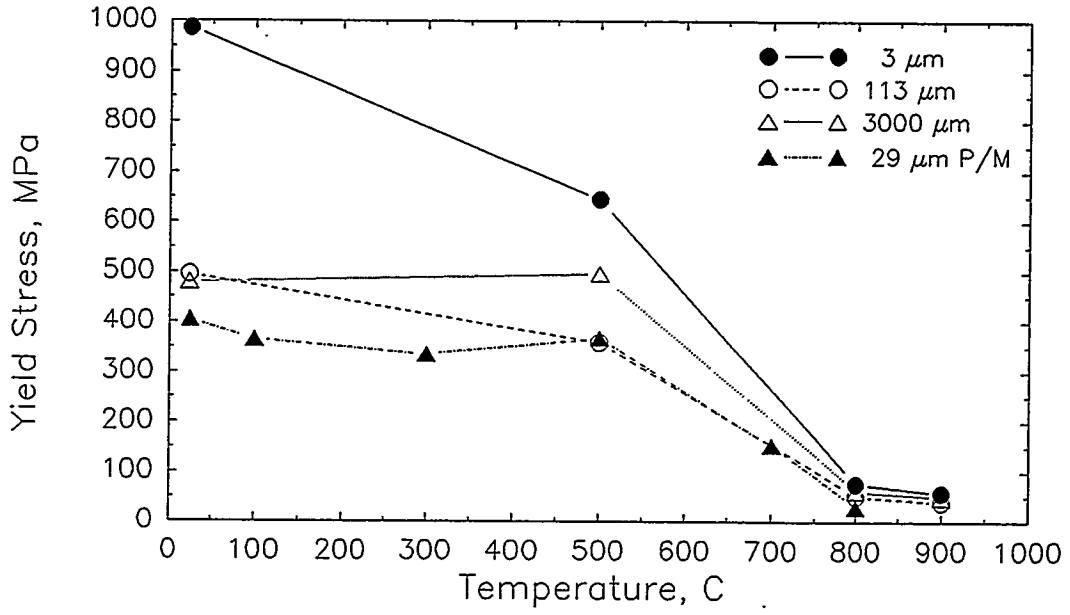

(a)

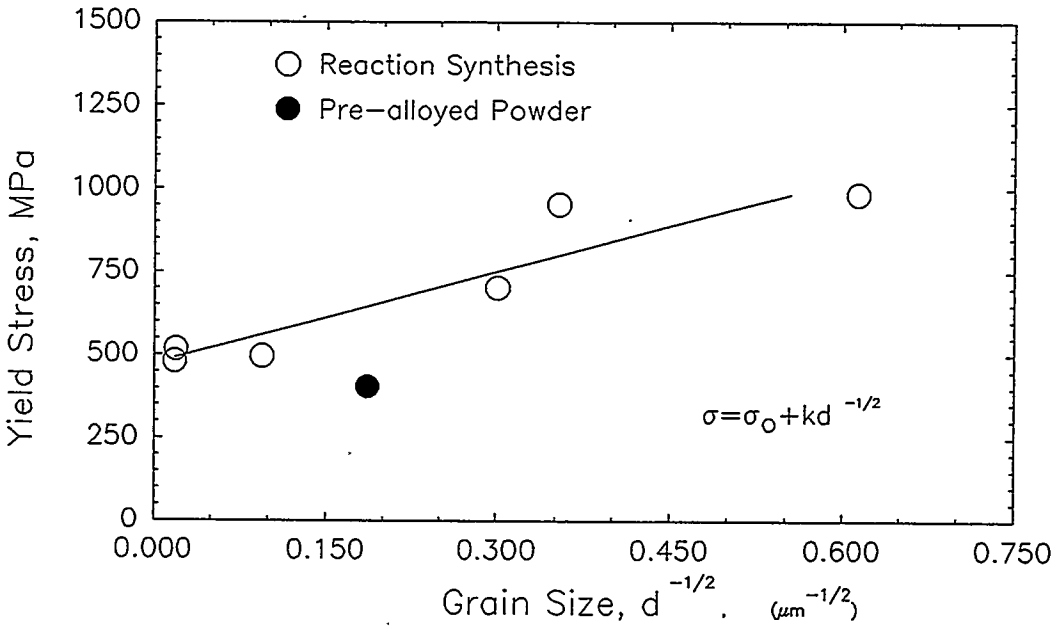

(b)

Fig. 6. Effects of temperature (a) and grain size (b) on yield stress of reaction synthesized Fe_3Al + 5%Cr.

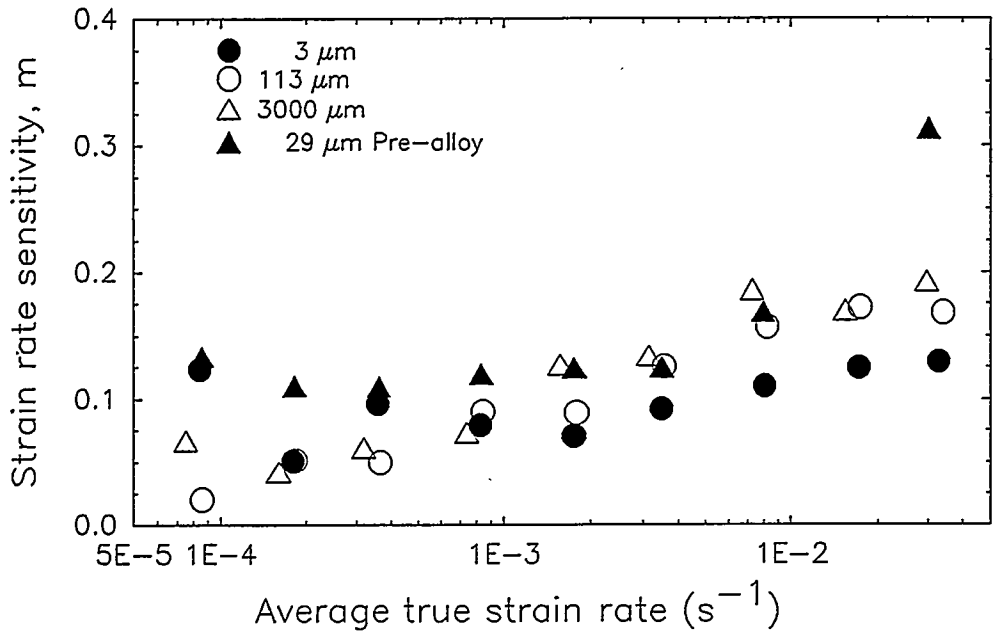

Fig. 7. Effect of grain size on strain rate sensitivity.

The low *m* values measured for this fine grained reaction synthesized material indicate that it is not superplastic even though superplasticity is frequently found in systems with small, stable equiaxed grains. Furthermore, *m* values which do not exhibit a dependence on grain size, as shown in Figure 7, suggest deformation does not occur by grain boundary sliding. A possible explanation for this behavior is that a fraction of the oxide particles reside in the grain boundary, preventing significant grain boundary sliding. These findings are in contrast to reports of superplasticity in a two phase Fe_3Al - Fe_2Nb reaction synthesized material (8) and in Ni_3Al (9).

Generally, large grains are desirable for good creep strength; in these materials, the absence of a grain boundary sliding mechanism holds the promise of reasonable creep properties despite the fine grain size. The total oxygen contents for the extruded and HIPped reaction synthesized materials are all very similar. The HIPped material is known to contain about 0.8 vol% dispersoid and it is expected that the extruded material has a similar oxide content. This value is about a factor of 3 less than commercial ODS alloys. Additional studies are planned to increase the oxide content of the reaction synthesized material, and to evaluate the tensile and creep properties of material with a higher volume fraction of particulate.

CONCLUSIONS

Fine grained Fe_3Al containing an oxide dispersion has been formed using reaction synthesis followed by consolidation by HIPping or extrusion. Materials consolidated by either method are fully dense and have grain sizes below 5 μm. The HIPped material exhibits very little grain growth at 1300°C, while material extruded at 900°C undergoes secondary recrystallization above 1100°C, resulting in a final grain size of greater than 25 millimeters.

The fine grain size after primary recrystallization results in significantly increased yield strength compared to conventional powder metallurgy material of the same composition. In addition to Hall-Petch strengthening, the oxide particles contribute approximately 200 MPa of strengthening at room temperature. Strain rate sensitivity tests indicate that grain boundary sliding is not a significant deformation mechanism up to temperatures of 900°C, even for the fine grained material.

ACKNOWLEDGEMENTS

The authors gratefully acknowledge the assistance of G. L. Fletcher and M. D. Harper in conducting experiments, and L. R. Harper in preparing the manuscript.

REFERENCES

1. C.G. Mckamey, J.H. DeVan, P.F. Tortorelli, and V.K. Sikka, J. Mater. Res., 6, 1779 (1991).
2. C.R. Clark, R.N. Wright, J.K. Wright, and B.H. Rabin, Scripta Met., accepted for publication.
3. R.L. Cairns, L.R. Curwick, and J.S. Benjamin, Metall. Trans., 6A, 179 (1975).
4. B.H. Rabin, J.K. Wright, R.N. Wright, and C.H. Sellers, J. Mater. Res., 9, 1384 (1984).
5. B.H. Rabin and R.N. Wright, Metall. Trans., 22A, 277 (1991).
6. J.J. Petrovic and L.J. Ebert, Metall Trans., 3, 1131 (1972).
7. M. Hillert, Acta Met., 12, 227 (1965).
8. S. Ranganath, A. Dutta, and J. Subrahmanyam, Scripta Met., 25, 1593 (1991).
9. R.N. Wright and J.R. Knibloe, Acta Metall., 38, 1993 (1990).

WELD OVERLAY CLADDING WITH IRON ALUMINIDES

G.M. Goodwin

Oak Ridge National Laboratory
P.O. Box 2008
Oak Ridge, TN 37831-6095

ABSTRACT

The hot and cold cracking tendencies of some early iron aluminide alloy compositions have limited their use in applications where good weldability is required. Using hot crack testing techniques invented at ORNL, and experimental determinations of preheat and postweld heat treatment needed to avoid cold cracking, we have developed iron aluminide filler metal compositions which can be successfully used to weld overlay clad various substrate materials, including 9Cr-1Mo steel, 2-1/4Cr-1Mo steel, and 300-series austenitic stainless steels. Dilution must be carefully controlled to avoid crack-sensitive deposit compositions. The technique used to produce the current filler metal compositions is aspiration-casting, i.e. drawing the liquid from the melt into glass rods. Future development efforts will involve fabrication of composite wires of similar compositions to permit mechanized gas tungsten arc (GTA) and/or gas metal arc (GMA) welding.

INTRODUCTION

We have made significant progress toward development of filler metals for weld overlay cladding using the GTA press on a number of substrate materials including austenitic stainless steel, 2-1/4 Cr-1 Mo steel, and 9 Cr-1 Mo steel. Aspiration casting is the primary technique being used for producing wire, with a smaller effort devoted to development of a shielded metal arc electrode formulation.

Development of Aspiration-Cast Filler Metal

Eleven compositional iterations of cast wire, produced both in-house and through a commercial supplier (Haynes International, Kokomo, IN) have led to optimized compositions which provide crack-free deposits on all three substrate materials. These developmental compositions are summarized in Table 1. A graphic illustration of the influence of aluminum level on cracking is shown in Figure 1. The two deposits on the left of the figure contain greater than 30 atomic % aluminum, and show severe hydrogen cracking, even though preheat of 350°C and postweld heat treatment of 750°C were employed. The two deposits on the right-hand side of the figure, welded under the same conditions, show no evidence of cracking. They contain 20 atomic % aluminum or less. It has been determined that approximately 20 atomic % aluminum or greater is required for optimum corrosion resistance, so in essence, the development effort has involved establishing the compositional window, as illustrated in Figure 2, within which good corrosion resistance and weldability coexist. The final heat of wire, denoted Haynes IV, is in the middle of this window, and represents the optimum composition for overlay cladding with these alloys using the manual GTA welding process. A typical single layer overlay clad (on type 304 stainless steel) is shown in Figure 3. Note that although crack-free deposits can readily produce with several of these filler metal compositions, preheat and postweld heat treatment must still be employed, typically 350°C and 750°C respectively, and dilution must be carefully controlled. Hydrogen cracking is still a problem with these materials.

Development of Shielded Metal-Arc (SMA) Electrodes

Through a cooperative research and development agreement (CRADA) with Devasco International, Houston, TX, we are attempting to extend the technology developed with aspiration-cast wire to the production of shielded metal arc (SMA) electrodes. This effort is considered to be very difficult and high-risk due to the aggressive nature of the fluxing agents which must be used in an electrode coating with the high aluminum contents

Table 1. Composition and Cracking Resistance of Developmental Iron Aluminide Filler Metals

	Nominal Wire Composition, Weight %			
Wire	Al	Cr	Other	Results
Haynes I	30	5	Nb, Ti, C, Mo, Zr, B	No Cracks
Haynes II	30	-	Nb, C, Zr, B	Unusable
ORNL I-01	30	-	Ti, Zr, B	Cracks
ORNL I-02	30	7	Ti, Zr, B	Cracks
ORNL I-03	30	-	C, Mo, Zr, B	Cracks
ORNL II-01	30	5	Nb, Ti, C, Mo, Zr, B	Cracks
ORNL II-02	25	5	Nb, Ti, C, Mo, Zr, B	Cracks
ORNL II-03	20	5	Nb, Ti, C, Mo, Zr, B	No Cracks
Haynes III-01	30	7	Nb, Ti, C, Mo, Zr, B	No Cracks
Haynes III-02	30	-	Mo, Zr, B	No Cracks
Haynes IV	25	7	C, Mo, Zr, B	No Cracks

YP19676

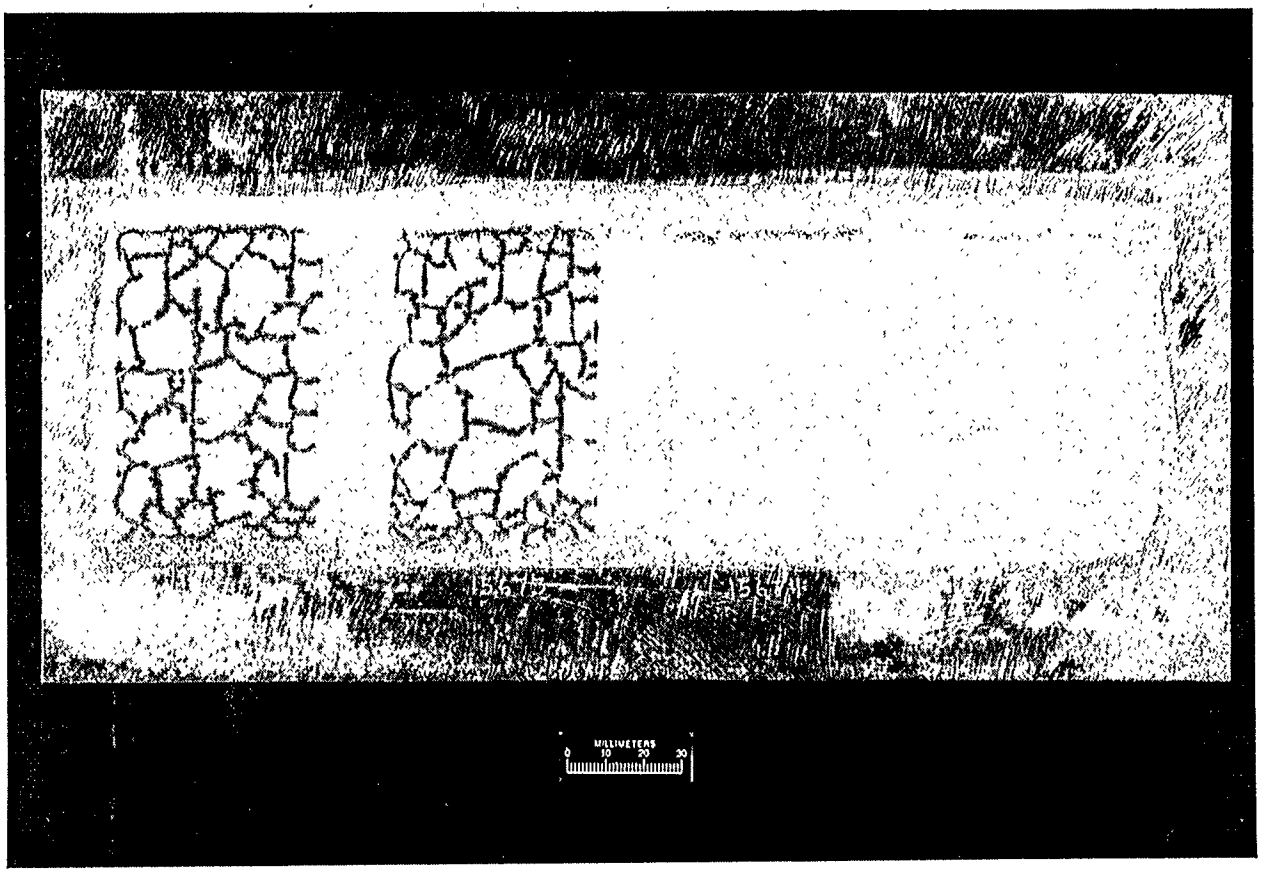

ORNL II-01	ORNL II-02	ORNL II-03	ORNL-385
35.8 a/o Al	31 a/o Al	20.2 a/o Al	8.5 a/o Al

Fig. 1. Iron aluminide weld deposits on 9 Cr-1 Mo plate.

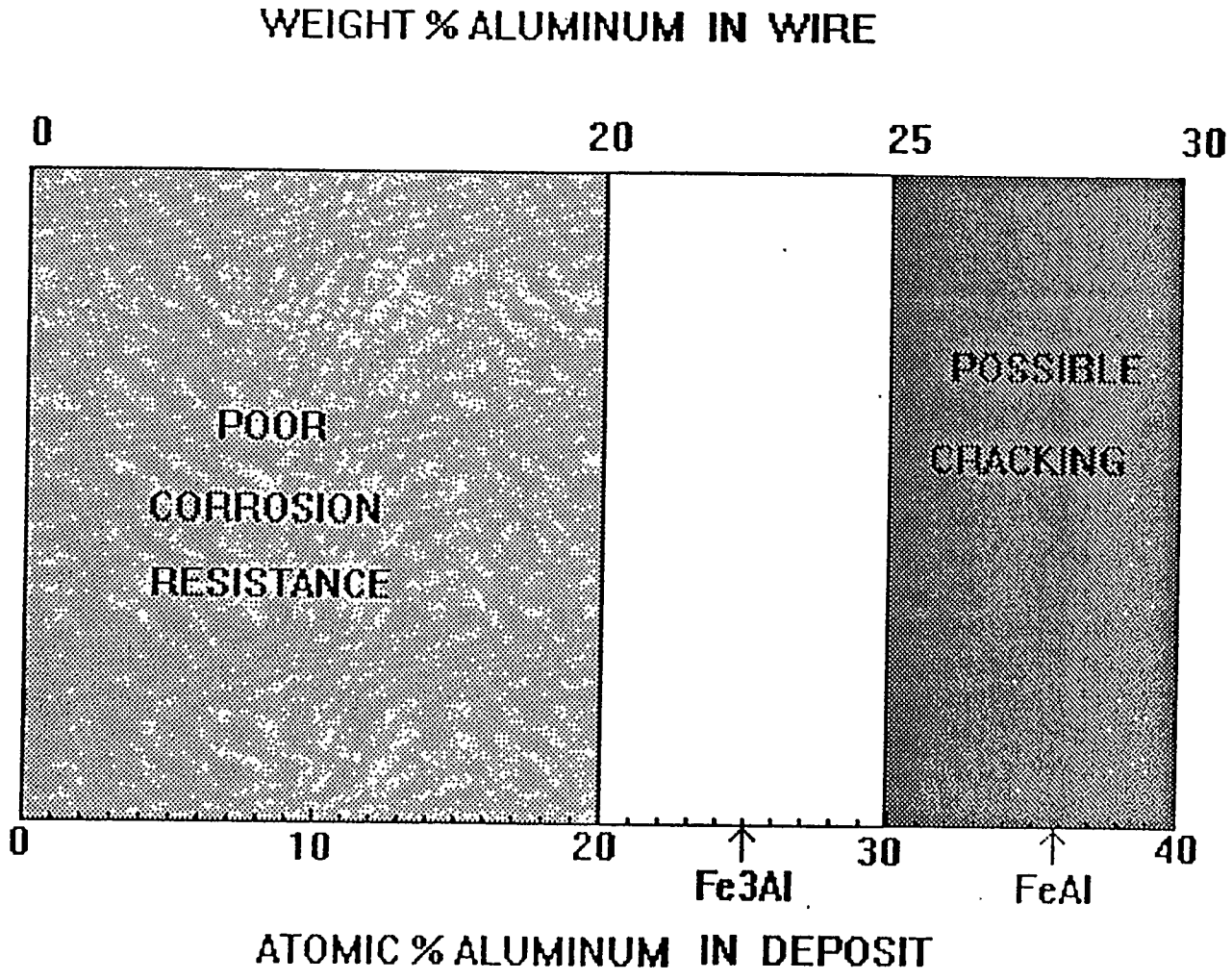

Fig. 2. Compositional window within which good corrosion resistance and weldability coexist.

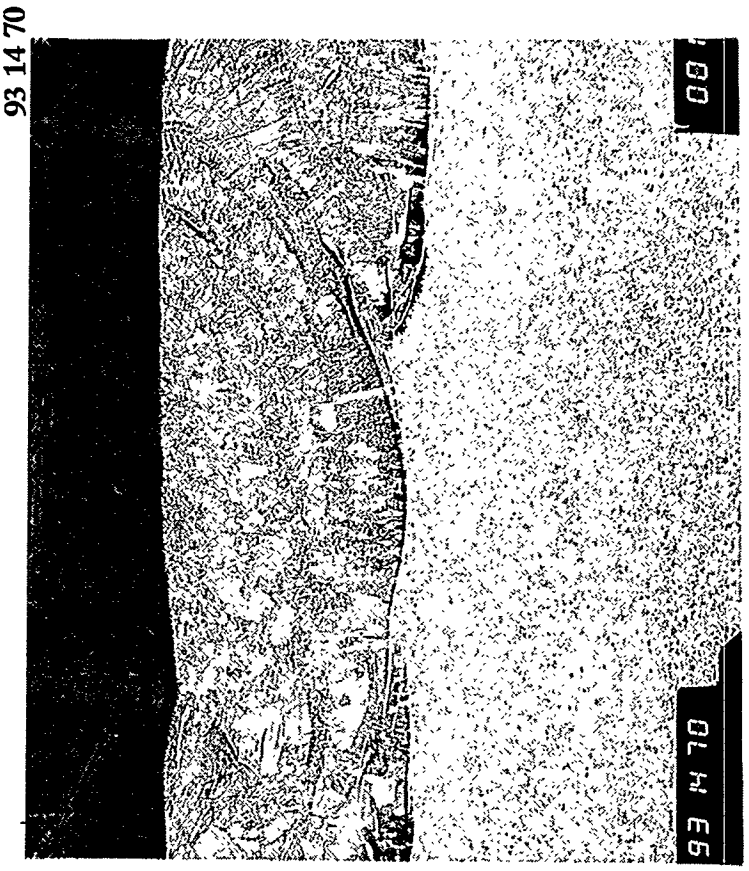

Fig. 3. Typical single layer GTA weld overlay (on type 304 stainless steel). 13x magnification. Deposit is approx. 3 mm thick.

involved here. Several coating formulations have been developed which provide adequate usability, but aluminum recovery in the deposit has been low. This task is continuing.

Development of Powder-Cored Filler Wire

Broader application of these alloys could be achieved, and economics significantly enhanced, by the development of a powder-cored wire formulation. The availability of this wire in coil form would permit careful control of dilution using the mechanized gas tungsten arc (GTA) and gas metal arc (GMA) welding processes, and would ultimately be much cheaper to produce and apply. Toward this end an order has been placed with Stoody Company, Bowling Green, KY, to produce 1/16-in. diam. wire yielding a deposit composition of approximately 15 weight % Al, 7 weight % Cr, 0.1 weight % C, 0.2 weight % Zr, 0.25 weight % Mo, balance Fe. This deposit composition is based on a single layer weld overlay on 2-1/4 Cr-1 Mo steel.

Conclusions

- Significant progress has been made toward development of aspiration-cast filler metal for GTA weld overlay deposits.
- A composition window of aluminum content has been established within which good corrosion resistance and weldability coexist; however,
- Hydrogen cracking is still a problem with these materials.
- Filler metals are being developed for alternate welding processes (mechanized GTA, GMA, SMA) to achieve broader application of the alloys.

HIGH-TEMPERATURE CORROSION BEHAVIOR OF IRON-ALUMINIDE ALLOYS AND COATINGS

P. F. Tortorelli, J. H. DeVan, B. A. Pint, and I. G. Wright

Oak Ridge National Laboratory
Oak Ridge, Tennessee, U. S. A.

and

S. R. J. Saunders

National Physical Laboratory
Teddington, Middlesex, United Kingdom

ABSTRACT

An Fe - 28 at.% Al - 2% Cr alloy doped with Y_2O_3 showed improved scale adhesion relative to a dispersion-free form of the same composition. However, doping with CeO_2 or La_2O_3 was detrimental to oxidation behavior. A study of weld-overlay iron-aluminide coatings showed that, those with sufficiently high aluminum concentrations had sulfidation resistance in H_2S-H_2-H_2O-Ar at 800°C equivalent to the most resistant bulk iron aluminides. These corrosion-resistant coatings have the potential to be effective barriers in high-temperature sulfidizing environments provided the appropriate combinations of filler metal, process parameters, and substrate are used to produce adequate aluminum concentrations and minimal chromium contents. Exposures in an oxidizing/sulfidizing environment containing varying amounts of HCl at 450 and 550°C showed that Fe_3Al alloys had good corrosion resistance.

INTRODUCTION

The iron-aluminum system has been studied by alloy developers for over sixty years.[1] A primary reason is the potential of iron aluminides for excellent high-temperature corrosion resistance in a number of environments. Alumina surface layers will form on iron aluminides even in environments with extremely low oxygen partial pressures.[2] This ability to form Al_2O_3 across a wide range of oxygen activities allows iron aluminides to be corrosion resistant not only in air or oxygen, but also to a variety of mixed gases and salts.[3] Therefore, determining the corrosion behavior of Fe_3Al alloys in aggressive environments at elevated temperatures forms an important part of the development of these aluminides. This paper reports recent results on the high-temperature corrosion behavior of iron aluminides relevant to three areas of alloy and process development for fossil-energy applications: oxidation of selected oxide-dispersion-strengthened (ODS) Fe_3Al alloys, sulfidation of iron-aluminide weld overlays, and corrosion of several iron-aluminum alloys in a simulated coal gasification environment in which the chlorine level was varied.

OXIDATION OF ODS Fe_3Al ALLOYS

As described elsewhere,[4] ODS Fe_3Al alloys are currently being developed to increase the operating temperature regime of these uniquely sulfidation-resistant materials. Determining the effects of a dispersion of oxides on the high-temperature oxidation resistance of Fe_3Al is a key part of this effort. Use of a reactive element (RE) oxide may further improve the adhesion of alumina scales on iron aluminides, as has been shown for the FeCrAl, NiCrAl, and NiAl systems (see, for example, refs. 5-7). The initial results on the effects of Y_2O_3, CeO_2, and La_2O_3 on high-temperature cyclic oxidation of Fe-28% Al-2% Cr (FAS) are summarized here. More details of the work with the Y_2O_3 and CeO_2-doped FAS can be found in ref. 8.

Powders of gas-atomized FAS and submicron oxides (Y_2O_3, CeO_2, or La_2O_3) were mechanically blended in a flowing Ar atmosphere using a high-speed attritor and stainless steel balls. (Unless otherwise noted, all concentrations are in at.%). The blended powder was canned, degassed, and extruded at 1100°C. For comparison, a FAS powder extrusion without an oxide addition, ingot-processed Fe-28% Al-5% Cr-0.1% Zr (FAL), and a commercial ZrO_2-dispersed (0.06% Zr) Fe-20% Cr-10% Al alloy (Kanthal alloy APM) were also tested. Coupons (about 15 mm diam x 1 mm thick) were polished with 0.3 μm alumina prior to oxidation. Cyclic oxidation experiments were conducted at 1200°C in air and in dry, flowing O_2. Admittedly, the exposure temperature of 1200°C is significantly higher than most potential applications for iron aluminides, but it is a convenient way to assess the potential lifetime of these materials based on aluminum consumption. A similar approach was previously used to predict oxidative lifetimes for ingot-processed iron aluminides and for comparison with FeCrAl alloys.[9] In short-term cyclic testing (2 h cycles), specimens were hung in a furnace in flowing O_2 and weight changes were measured continuously using a microbalance to check for any indication of isothermal spallation. (However, spallation was only observed upon cooling.) In long-term testing (100 h cycles), specimens were placed in a static air furnace inside individual alumina crucibles so that any spalled oxide was collected and weighed. In both types of tests, the specimen weight changes were measured before and after oxidation. After oxidation, specimens were examined using scanning electron microscopy (SEM) with energy dispersive x-ray (EDX) analysis.

Specimen weight change data for the various alloys exposed to 2 h cycles are shown in Fig. 1. A fine powdery alumina scale formed on the undoped FAS alloy and led to large weight losses after just a few cycles. In contrast, rapid weight gains were observed for the CeO_2- and La_2O_3-dispersed alloy specimens. The CeO_2-dispersed alloy exposure was

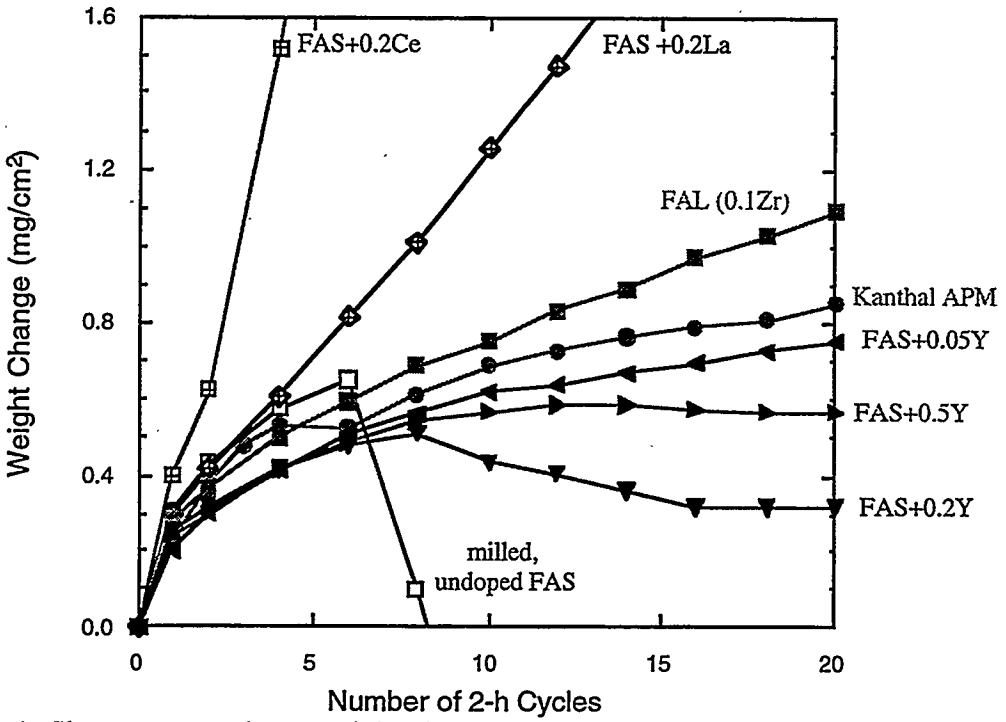

Fig. 1. Short-term specimen weight changes upon cyclic oxidation at 1200°C in O_2 for iron aluminides with various oxide dispersions.

stopped after 14 cycles when breakaway oxidation (formation of FeO_x) began at one edge. The detrimental effects of CeO_2 and La_2O_3 are comparable to that of La_2O_3 in β-NiAl.[7] In all these cases, the additions resulted in accelerated oxidation relative to the undoped alloy. Whether this effect is primarily in the oxide or in the alloy is unclear and is under investigation.

All cyclically exposed alloys had some scale loss except for the ZrO_2-dispersed FeCrAl and the FAS with 0.05% of Y cations. Of the Y_2O_3-dispersed FAS alloys, the 0.2% Y addition had the largest amount of scale spallation (about 40% of area), in agreement with the weight change measurements shown in Fig. 1. In general, spallation to bare metal was observed and voids at the metal-oxide interface were apparent. However, compared to the undoped alloy, all of the Y_2O_3 additions to FAS reduced the amount of scale spallation. Also, Y doping produced a flatter, less convoluted scale than that observed on the undoped FAS, as does Zr in the ingot-processed FAL.

The longer-term cyclic oxidation results are shown in Fig. 2. In contrast to the data in Fig. 1, the specimens were exposed for 100 h each time and the reported results represent total mass change (specimen plus any spalled oxide). In this way, the measurements are proportional to the amount of metal consumed by oxidation. Comparing these total weight

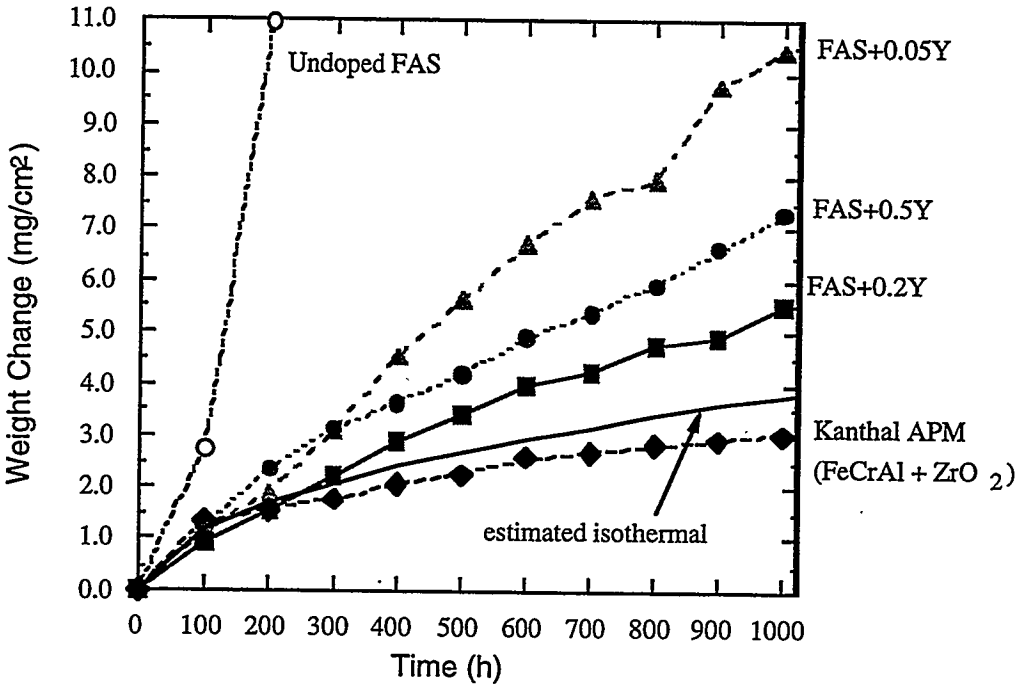

Fig. 2. Total weight gain (including spalled scale) for 100-h cycles at 1200°C in air.

gains, the alloy with the smallest Y_2O_3 addition (0.05% Y) performed worst and that with the 0.2% Y had the best behavior, which is the opposite result of the short-term oxidation results (Fig. 1). Nevertheless, Y_2O_3 additions still improved oxidation resistance relative to the undoped FAS alloy, which went into breakaway oxidation after three cycles. The ability to increase the effectiveness of yttria, and possibly other oxides, in increasing the oxidation resistance of iron aluminides by improving dispersion uniformity and controlling microstructure is currently under study.

The rate at which aluminum in the alloy is consumed is a critical factor in predicting time to breakaway oxidation (as defined above) and the higher Al content of iron aluminides relative to FeCrAl alloys could result in longer oxidative lifetimes. However, scale spallation was more severe for the Y_2O_3-doped FAS alloys than for the ZrO_2-dispersed FeCrAl and, based on the total weight gains (Fig. 2), the aluminum consumption rate was 2 to 4 times higher for the former materials. In previous work on ODS FeCrAl and β-NiAl alloys,[10] Y and Zr dopants were found to have identical beneficial effects on the oxidation behavior. Thus, it appears that the difference in oxidation behavior between the ODS FeCrAl and Fe_3Al alloys cannot be explained by the difference in their dopant oxides. Furthermore, the Zr-containing FAL suffered greater cyclic weight gains and scale spallation than the Zr-doped FeCrAl alloy (Fig. 1). A similar result was also observed for 1300°C oxidative lifetime testing:[9] despite the

lower Al content of a RE-doped FeCrAl alloy, its time to breakaway oxidation was comparable to that for ingot-processed FAL containing 0.1% Zr, thereby indicating a higher Al consumption rate for the FAL alloy.

OXIDATION-SULFIDATION OF IRON-ALUMINIDE WELD OVERLAYS AT 800°C

The oxidation and sulfidation resistance of iron aluminides containing greater than 18 - 25 at.% Al is maintained at temperatures (for example, 800°C) well above those at which these alloys have adequate mechanical strength. Because of this, and possible cost considerations, it is anticipated that appropriate compositions of iron aluminides may find application as coatings or claddings on more conventional higher-strength materials which are less corrosion-resistant at high temperatures. Initial work in this regard focused on examining the sulfidation resistance of iron-aluminide coatings deposited by a weld-overlay technique.

Weld-overlay deposits of Fe-Al alloys were produced on 25 mm-thick 2.25 Cr - 1 Mo (wt%) steel and 50 mm-thick type 304 stainless steel substrates using techniques and filler materials described elsewhere.[11,12] Rectangular pieces, approximately 18 x 12 mm, were cut from the weld overlay specimens. Coupons for the corrosion experiments were then prepared by grinding away the substrate material so that they consisted of only weld metal (approximately 1 - 2 mm thick). Corrosion behavior was characterized by use of a continuous-recording microbalance to measure the weight of these specimens during exposure at 800°C to a flowing (~2 cm^3/s) mixed gas consisting of 5.4% H_2S - 79.4% H_2 - 1.6% H_2O - 13.6% Ar (by volume). The oxygen partial pressure, as determined by a solid-state oxygen cell, was 10^{-22} atm, and the sulfur pressure was calculated to be 10^{-6} atm. This type of experiment has been used to characterize the sulfidation resistance of many iron aluminides and several other alloys.[3,13,14] Due to mixing during welding, the composition of a particular weld overlay depends not only on the elements present in the filler metal but also on the alloy used as the substrate.[11,12] Therefore, it was important to determine the actual concentrations of the appropriate elements in the deposited layers and these are shown in Table 1.

The weight change results for the six overlay coatings exposed to H_2S - H_2 - H_2O - Ar at 800°C are shown in Fig. 3. The curves clearly fell into groups of either low (C1, C2, C3) or high (O1, O2, O3) weight gains. Figure 4 presents a more detailed view of the thermogravimetric data for the coupons in the low weight-gain group and, for the sake of comparison, includes two curves for specimens of wrought FAS. This composition has been shown to be among the most corrosion-resistant Fe_3Al alloys in this gas mixture.[14]

Table 1. Weld Deposit Compositions

Specimen	Substrate	Concentration (at.%)[a]							
		Al	Cr	Nb	Ti	Ni	Mo	Zr	C
C1	Cr-Mo	35.4	2.5	0.2	0.4	-	0.6	0.2	1.0
C2	Cr-Mo	36.7	4.7	0.2	0.4	-	0.6	0.2	1.0
C3	Cr-Mo	35.5	0.7	-	-	-	0.7	0.1	1.0
O1	304	11.1	6.7	<0.01	<0.01	6.6	0.2	0.03	0.5
O2	304	23.1	6.3	0.1	0.1	6.3	0.2	0.1	0.5
O3	Cr-Mo	21.7	2.1	0.1	-	-	0.7	0.1	-

[a] Determined by spark source mass spectrometry. Balance is Fe.

Differences in corrosion behavior between the C and O groups of specimens were also reflected in the respective corrosion product morphologies.[15] The higher-aluminum specimens exhibited thin, fairly uniform scales with just a small amount of powdery, spalled scale. In contrast, significant scale loss (upon cooling and handling), were observed for the three coatings with lower aluminum concentrations. Specimens O1 and O2 had relatively thick, black corrosion products which consisted of dense mattes of aluminum and iron sulfides, as determined by EDX analyses in a SEM. Specimen O3 exhibited a smaller population of the same type of sulfides.

Based on findings from previous iron-aluminide studies,[3,14] the corrosion data shown in Figs. 3 and 4 are consistent with the deposit compositions recorded in Table 1. The coatings exhibiting relatively high weight gains and corrosion rates (O1, O2, O3) have relatively low aluminum and high chromium concentrations. In the case of O1, the aluminum content is very much lower than what has been found to be needed for the best sulfidation resistance,[16] while O2 and O3 exceed this critical concentration somewhat. As expected, O1 showed the greatest sulfidation susceptibility of the group O specimens due to its low aluminum concentration. The somewhat worse behavior of O2 vis-à-vis O3 is probably due to the higher chromium and nickel concentrations of the former. Chromium levels similar to that in O2 exacerbate the sulfidation reaction for Fe_3Al alloys.[14] While the three weld clads with the lower aluminum concentrations exhibited substantial mass gains, their relative corrosion resistance was still somewhat better than that of Fe-Cr-Ni alloys.[13,14]

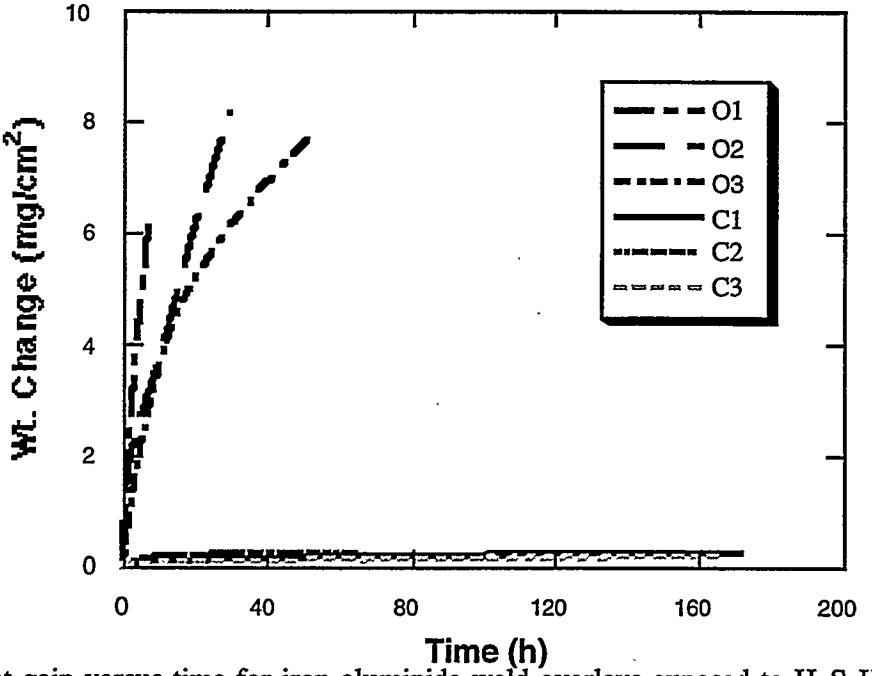

Fig 3. Weight gain versus time for iron-aluminide weld overlays exposed to H_2S-H_2-H_2O at 800°C. Overlay compositions are shown in Table 1.

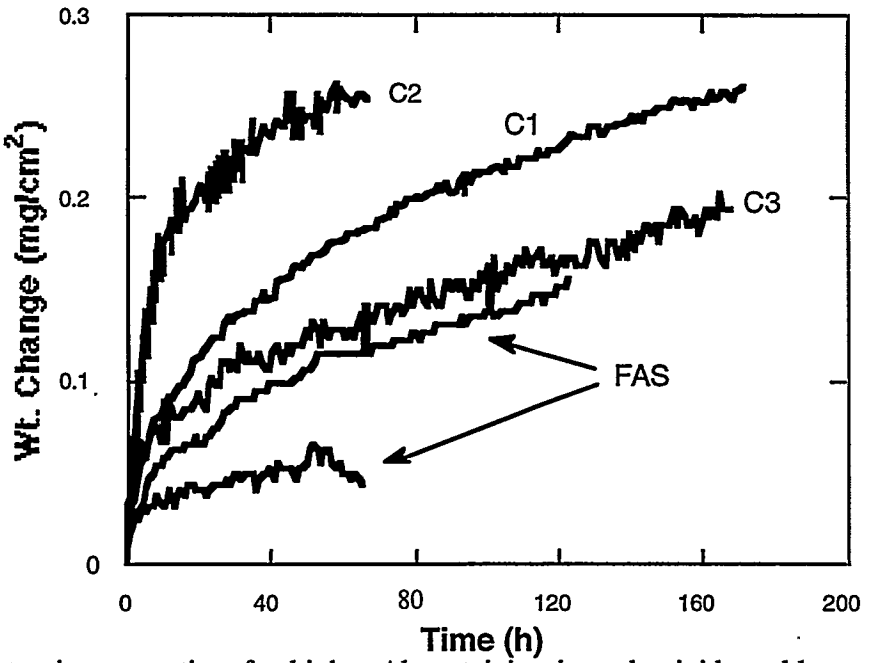

Fig. 4. Weight gain versus time for higher-Al-containing iron-aluminide weld overlays and alloy FAS exposed to H_2S-H_2-H_2O at 800°C. Overlay compositions are shown in Table 1.

The specimens denoted C1, C2, and C3 all have aluminum concentrations well in excess of the critical amount needed for excellent sulfidation resistance in the subject mixed gas.[16] Their oxidation/sulfidation behavior therefore resembles that of the most resistant iron aluminides.[14] The deleterious effect of Cr is normally not observed at the higher aluminum levels in the group C specimens[3,14] and little, if any, detrimental influence of the higher chromium concentration of C2 was detected (Fig. 4). Compared with the results shown in Fig. 3, the weight gains and rates in Fig. 4 are low; differences among the curves are not statistically significant.

The present results show that iron-aluminide weld overlays have the potential to be effective corrosion-resistant coatings in high-temperature sulfidizing environments provided the appropriate combinations of filler metal, process parameters, and substrate are used to produce adequate aluminum concentrations and minimal chromium contents. In the present study, the spread in aluminum concentration between the group O and C specimens is too large to precisely define the clad composition necessary to achieve low corrosion rates. The higher aluminum concentrations of the group C specimens would provide a margin of safety with respect to sulfidation resistance, particularly in view of enrichment of the weld overlay in substrate elements (for example, chromium and nickel) that are deleterious to sulfidation resistance. Furthermore, excess aluminum would delay any onset of breakaway oxidation caused by aluminum depletion.[9] However, weld deposits containing high aluminum concentrations are much more sensitive to hydrogen-induced cracking when exposed to moist air, even after stress relief. In this regard, it must be noted that, as only the coatings themselves were tested in the corrosive environment, the present study was focused on the thermodynamic stability and reaction kinetics of the weld deposits and did not examine the effects of extended defects. The actual protectiveness of a particular layer will also depend on the ability of these layers to provide a physical barrier that doesn't delaminate or allow corrosion of the substrate by ingress of reactive species via cracks or other defects. These aspects will be investigated through exposure of clad substrates to the particular corrosive environment.

EFFECT OF CHLORINE ON THE OXIDATION-SULFIDATION OF IRON ALUMINIDES AT 450 AND 550°C

In some fossil energy applications, iron aluminides will have to show corrosion resistance to product gases that contain small concentrations of HCl in an oxidizing-sulfidizing atmosphere of relatively high p_{S_2} and low p_{O_2}. Because of this, the effect of HCl on the corrosion of FAS, FA129 (Fe-28% Al-5% Cr-0.5% Nb- 0.2% C), and FAP (Fe-16% Al-

5% Cr-1.1% Mo - 0.1% Zr - 0.1% C) in a simulated coal gasification environment has been studied in collaboration with the National Physical Laboratory (NPL) in the United Kingdom. The sulfur and oxygen fugacities of the gas were, respectively, 5×10^{-8} and 1×10^{-26} at 450°C and 2×10^{-6} and 2×10^{-22} at 550°C. Two levels of HCl additions, 1000 and 3283 ppm, were examined. General details of the experiments and initial results (for 1000 ppm HCl) have been described previously.[9] A FeCrAlY alloy was included in the exposures for comparison.

Gravimetric results for exposures in the mixed gas with 3283 ppm of HCl are shown in Fig. 5. As with the results for mixed gas with 1000 ppm HCl,[9] weight changes of FAP were substantially higher than those of the other three alloys and, at 550°C, FAS and FA129 performed somewhat better than the FeCrAlY. Differences in corrosion susceptibility are also shown in Fig. 6, which contains representative cross sections of exposed aluminides. Thin, presumably alumina, scales formed on FAS and FA129 (Fig. 6a and b) and provided adequate protection. Penetration along a few grain boundaries was noted. Such attack has not been noticed for sulfidation of iron aluminides at higher temperatures in the absence of HCl, but the present observations of such were limited to a small fraction of the exposed surface area. In contrast, FAP (Fig. 6c) exhibited significantly thicker scales that included sulfides. The reaction product on the FeCrAlY was thinner than that on FAP, but thicker than those found on FAS and FA129, which is consistent with the gravimetric data for the 550°C exposures in the environments with HCl at concentrations of 1000 ppm (ref. 9) and 3283 ppm (Fig. 5).

In studies conducted in a similar type of mixed-gas at 800°C, but without HCl additions, both higher chromium levels ($\geq$ 2%) and lower aluminum concentrations ($<$ ~18%) contributed to reduced resistance to corrosion.[3,14,16] In the case of the present exposures, a concentration of 5% Cr in Fe_3Al (FA129), which reduces sulfidation resistance at higher temperatures, did not have a significant effect at 450 and 550°C in the presence of HCl. Additionally, the substantial chromium concentration (~20%) of the FeCrAlY, which has a dramatic deleterious effect in the aforementioned high-temperature sulfidizing environment,[3,14,16] appears to have only a minor influence in the mixed gas + HCl; the corrosion susceptibility of this alloy was similar to that of FAS and FA129 at 450°C and only moderately worse at 550°C. On the other hand, the lower aluminum concentration of FAP (16%) appears to have been a major factor in its relatively poor performance under these conditions, as well as at higher temperatures.[3,16]

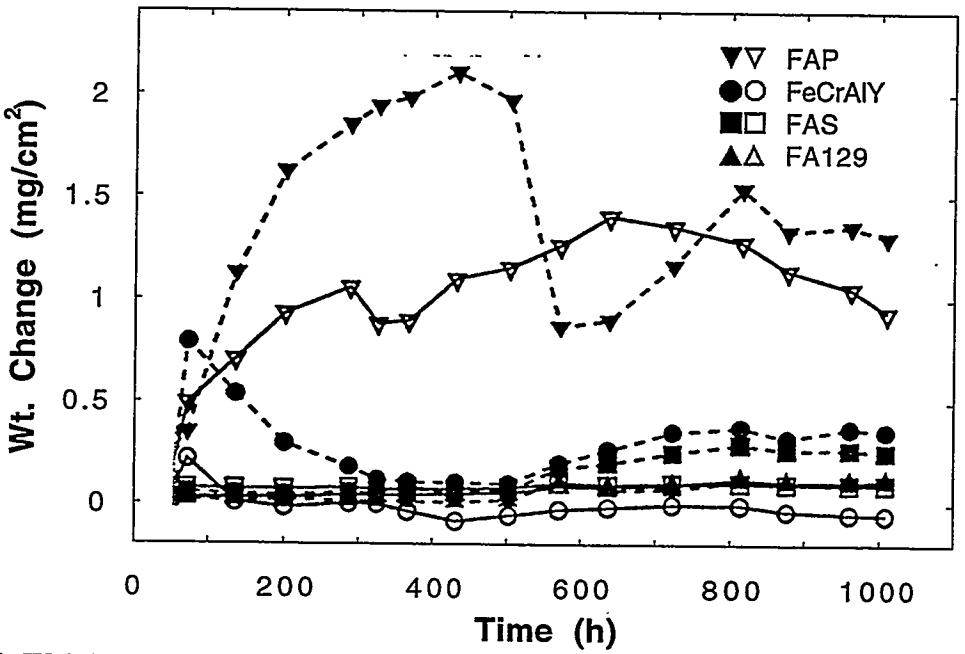

Fig. 5. Weight changes vs. time for exposures in a simulated coal-gasification environment containing 3283 ppm HCl at 550°C.

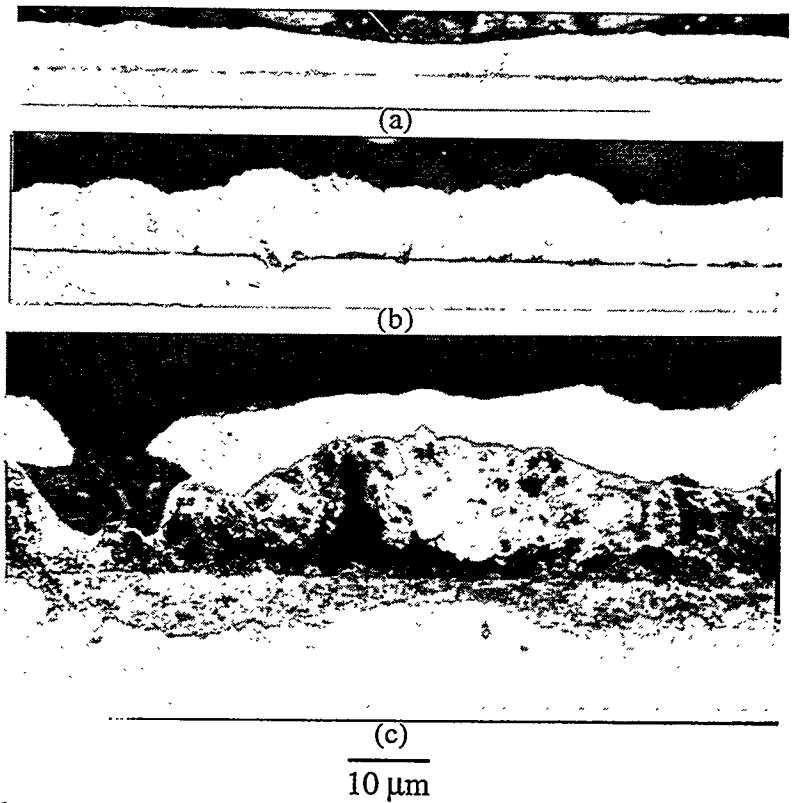

Fig. 6 Polished cross sections of iron aluminides exposed in a simulated coal-gasification environment containing 3283 ppm HCl at 550°C for 1007 h. The specimens were coated with copper prior to sectioning (visible as bright topcoat). (a) FAS (b) FA129 (c) FAP

SUMMARY AND CONCLUSIONS

Oxide-dispersed Fe - 28% Al - 2% Cr alloys doped with Y_2O_3, CeO_2, and La_2O_3 were prepared and cyclically oxidized at 1200°C. Yttria improved scale adhesion relative to the undoped alloy, but was not as effective as zirconia in an FeCrAl alloy. Both CeO_2 and La_2O_3 were detrimental to oxidation behavior.

Specimens of weld-overlay iron-aluminide coatings were exposed to H_2S-H_2-H_2O-Ar at 800°C. The investigation focused only on the weld overlay material and, as such, involved the characterization of the thermodynamic and kinetic stabilities of these coatings rather than their ability to physically separate the corrosive species from susceptible substrate material. Under conditions that produced coatings with sufficiently high aluminum concentrations, corrosion resistance equivalent to the best bulk iron aluminides was found.

Three iron aluminides and a standard FeCrAlY alloy were exposed at 450 and 550°C in an oxidizing/sulfidizing environment containing varying amounts of HCl at the National Physical Laboratory in the United Kingdom. Two 28% Al - 5% Cr alloys, FA129 and FAL, were more resistant than FeCrAlY at 550°C and Fe - 16% Al - 5% Cr (FAP) at both temperatures. For FA129 and FAL, there was little evidence to suggest any accelerating effect of HCl up to a concentration of about 3300 ppm.

ACKNOWLEDGMENTS

The authors thank M. Howell for experimental support and J. R. DiStefano, G. M. Goodwin, and C. G. McKamey for their reviews of the manuscript. This research was sponsored by the Fossil Energy Advanced Research and Technology Development (AR&TD) Materials Program, U S. Department of Energy, under contract DE-AC05-84OR21400 with Martin Marietta Energy Systems, Inc. B. A. Pint is supported by the U S. Department of Energy Distinguished Postdoctoral Research Program administered by the Oak Ridge Institute for Science and Education.

REFERENCES

1. C. G. McKamey, J. H. DeVan, P. F. Tortorelli, and V. K. Sikka, J. Mater. Res. **6**, 1779 (1991).
2. P. Tomaszewicz and G. R. Wallwork, Rev. High Temp. Materials **4**, 75 (1978) 75-105.
3. P. F. Tortorelli and J. H. DeVan, pp. 257-70 in Processing, Properties, and Applications of Iron Aluminides, J. H. Schneibel and M. A. Crimp (eds.), The Minerals, Metals, and Materials Society, Warrendale, PA, 1994.
4. I. G. Wright, C. G. McKamey, and B. A. Pint, "ODS Iron Aluminides," these proceedings.
5. W. J. Quadakkers, K. Schmidt, H. Grubmeier, and E. Wallura, Mater. High. Temperature **10**, 23 (1992).

6. H. T. Michels, Metall. Trans. A **9A**, 873 (1978)

7. B. A. Pint and L. W. Hobbs, pp. 987-92 in High-Temperature Ordered Intermetallic Alloys VI, J. A. Horton, I. Baker, S. Hanada, R. D. Noebe, and D. S. Schwartz (eds.), The Materials Research Society, Pittsburgh, PA, 1995.

8. B. A. Pint, K. B. Alexander, and P. F. Tortorelli, "The Effect of Various Oxide Dispersions on the Oxidation Resistance of Fe_3Al," pp. 1315-20 in High-Temperature Ordered Intermetallic Alloys VI, J. A. Horton, I. Baker, S. Hanada, R. D. Noebe, and D. S. Schwartz (eds.), The Materials Research Society, Pittsburgh, PA, 1995.

9. J. H. DeVan, P. F. Tortorelli, and M. J. Bennett, pp. 309-20 in *Proc. Eighth Annual Conf. Fossil Energy Materials*, N. C. Cole and R. R. Judkins (comp.), CONF-9405143, U. S. Department of Energy, August 1994.

10. B. A. Pint, Oxid. Met. **44**, (1995) in press.

11. G. M. Goodwin, P. J. Masiasz, C. G. McKamey, J. H. DeVan, and V. K. Sikka, pp. 205-10 in *Proc. Eighth Annual Conf. Fossil Energy Materials*, N. C. Cole and R. R. Judkins (comp.), U. S. Department of Energy, 1994.

12. G. M. Goodwin, "Weld Overlay Cladding With Iron Aluminides," these proceedings

13. J. H. DeVan, H. S. Hsu, and M. Howell, Oak Ridge National Laboratory report, ORNL/TM-11176, May 1989.

14. J. H. DeVan, pp. 107-115 in Oxidation of High-Temperature Intermetallics, T. Grobstein and J. Doychak (eds.), The Minerals, Metals, and Materials Society, 1989.

15. P. F. Tortorelli, J. H. DeVan, G. M. Goodwin, and M. Howell, accepted for publication in High-Temperature Coatings I, N. B. Dahotre, J. Hampikian, and J. J. Stiglich (eds.), The Minerals, Metals, and Materials Society, Warrendale, PA, 1994.

16. J. H. DeVan and P. F. Tortorelli, Corros. Sci. **35**, 1065 (1993).

EFFECT OF SURFACE CONDITION ON THE AQUEOUS CORROSION BEHAVIOR OF IRON ALUMINIDES

R. A. Buchanan and R. L. Perrin

Department of Materials Science and Engineering
University of Tennessee
Knoxville, TN 37996-2200

ABSTRACT

The effects of retained high-temperature surface oxides, produced during thermomechanical processing and/or heat treatment, on the aqueous-corrosion characteristics of Fe-Al-based alloys were evaluated by electrochemical methods. Cyclic anodic polarization evaluations were conducted at room temperature in a mild acid-chloride solution (pH = 4, 200 ppm Cl^-) on the Fe_3Al-based iron aluminides, FA-84 (Fe-28Al-2Cr-0.05B, at. %), FA-129 (Fe-28Al-5Cr-0.5Nb-0.2C, at. %), and FAL-Mo (Fe-28Al-5Cr-1Mo-0.04B-0.08Zr, at. %), on the FeAl-based iron aluminide, FA-385 (Fe-35.65Al-0.20Mo-0.05Zr-0.11C, at. %), and on the disordered low-aluminum Fe-Al alloy, FAPY (Fe-16.1Al-5.4Cr-1.1Mo-0.1C, at. %). The surface conditions evaluated were: as-received (i.e., with the retained high-temperature oxides), mechanically cleaned (ground through 600-grit SiC paper), and chemically cleaned (10% HNO_3, 2% HF, at 43 °C). The principal electrochemical parameter of interest was the critical pitting potential, with lower values indicating less resistance to chloride-induced localized corrosion. For all materials evaluated, the critical pitting potential was found to be significantly lower in the as-received condition than in the mechanically-cleaned and chemically-cleaned conditions. Mechanisms responsible for the detrimental high-temperature-oxide effect are under study.

INTRODUCTION

The overall objective of this project is to study the effects of retained high-temperature surface oxides, produced during thermomechanical processing and/or heat treatment, on the aqueous-corrosion and environmental-embrittlement characteristics of several Fe_3Al-based iron aluminides, an FeAl-based iron aluminide, and a low-aluminum Fe-Al alloy. Previous aqueous-corrosion studies of these materials by the present authors and colleagues have examined specimens only with cleaned surfaces (i.e., mechanically ground or polished surfaces).[1-4] The high-temperature surface oxides of the present study are not likely to have the same chemistry nor the same morphology (e.g., thermal cracking) as the passive films formed naturally on a clean surface in an aqueous environment. It was hypothesized that the presence of the high-temperature oxide could decrease the resistance to localized corrosion, which, in turn, could increase the probability of hydrogen production during aqueous corrosion processes, leading to

enhanced environmental embrittlement. To address these issues, the project involves cyclic-anodic-polarization testing to evaluate aqueous-corrosion behavior and U-bend stress-corrosion-cracking testing to evaluate environmental-embrittlement behavior.

To date, most of the anodic polarization testing has been completed, utilizing a mild acid-chloride electrolyte at room temperature. These results are herein reported. Upon completion of this phase of the research, the focus will shift to evaluations of the high-temperature-oxide effects on stress-corrosion cracking properties.

In the mild acid-chloride solution, which was designed to simulate aggressive atmospheric-corrosion, the alloys of this study are susceptible, in varying degrees, to pitting corrosion. An excellent method for evaluating the relative pitting-corrosion susceptibility involves producing and analyzing cyclic anodic polarization curves. A schematic illustration of such a curve is shown in Figure 1, where certain electrochemical parameters are identified. To produce the curve, the corrosion sample first is allowed to stabilize in the electrolyte such that a steady-state, open-circuit, corrosion potential, E_{corr}, is established. Next, with a potentiostatic circuit, the potential of the sample, E, is forced in the positive direction at a given rate while the current density, i, is continuously measured. After the potential has moved away from E_{corr} by a relatively small amount ($\approx$ 50 mV), the current density is directly proportional to the corrosion rate. The potential scan is continued in the positive direction until a predetermined reversing current density, i_r, is reached. At this point, the potential scan direction is reversed, moving in the negative direction, and continued until a very low current density is achieved. In Figure 1, the nearly vertical region in the up-scan portion of the curve, characterized by an average passive current density, i_p, is reflective of passivation, where the material has developed a thin protective oxide/hydroxide passive film, and, therefore, corrodes at a very low rate over a range of potentials. At the critical pitting potential, E_{pit}, pitting corrosion initiates, with a sharp increase in current density. The pitting corrosion accelerates to i_r, and continues during the down-scan portion of the curve until the protection (or repassivation) potential, E_p, is reached (which corresponds to the cross-over point for the up-scan and down-scan curves). With reference to Figure 1, two of the parameters often used to characterize relative resistance to pitting corrosion are: (1) the magnitude of E_{pit}, with higher values corresponding to greater pitting resistance, and (2) the difference between E_{pit} and E_{corr}, i.e., (E_{pit} - E_{corr}), with higher values corresponding to greater pitting resistance.

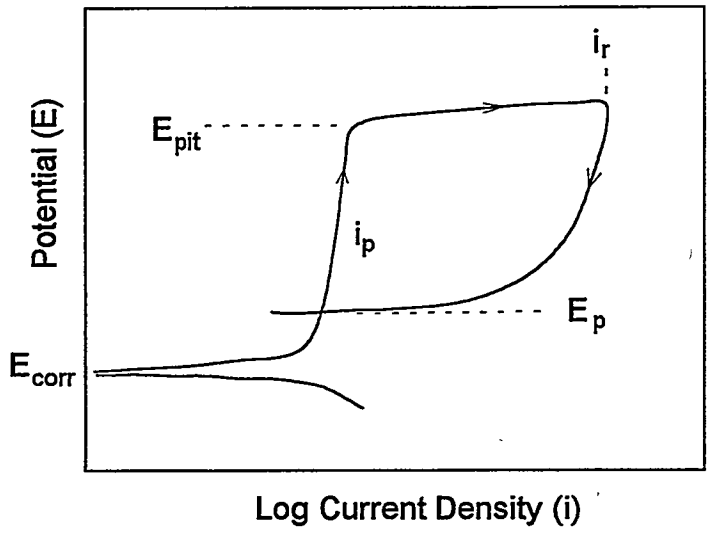

Fig. 1. Schematic illustration of cyclic anodic polarization behavior.

EXPERIMENTAL PROCEDURES

Cyclic anodic polarization tests were conducted at room temperature in a mild acid-chloride solution (pH = 4, 200 ppm Cl^-) on the following materials: the Fe_3Al-based iron aluminides, FA-84 (Fe-28Al-2Cr-0.05B, at. %), FA-129 (Fe-28Al-5Cr-0.5Nb-0.2C, at. %), and FAL-Mo (Fe-28Al-5Cr-1Mo-0.04B-0.08Zr, at. %), a disordered low-aluminum Fe-Al alloy, FAPY (Fe-16.1Al-5.4Cr-1.1Mo-0.1C, at. %), and an FeAl-based iron aluminide, FA-385 (Fe-35.65Al-0.20Mo-0.05Zr-0.11C, at. %). The FA-84, FA-129, FAL-Mo, and FAPY materials, in as-processed sheet form, were kindly supplied by Dr. Vinod Sikka of the Oak Ridge National Laboratory (ORNL); the FA-385 material, in rod form with a cladding, was kindly supplied by Dr. Philip Maziasz of ORNL.

For the FA-84, FA-129, FAL-Mo, and FAPY materials, the surface conditions evaluated were as follows: (1) as-processed (i.e., with the retained high-temperature oxides characteristic of the prior thermomechanical processing methods), (2) mechanically cleaned (ground through 600-grit SiC paper to remove all high-temperature oxides), and (3) chemically cleaned (immersed in a 10% HNO_3, 2% HF solution, at 43 °C, until all high-temperature oxides were removed (approximately 30 minutes), then immersed in 10% HNO_3 at 43 °C for one hour as a passivation treatment). Because of the form of the as-received FA-385 material (rods with protective claddings), it did not

have the high-temperature oxides. To create the high-temperature-oxide surface condition, the FA-385 samples were annealed in air at 750 °C for one hour, then air cooled. This condition will be referred to as the "heat treated" condition, not as the as-processed condition. The mechanically-cleaned and chemically-cleaned conditions were accomplished in the same manner as described for the other materials.

Cyclic anodic polarization tests were performed with a standard polarization cell and an EG&G Model 273 potentiostat. Each sample was mounted in epoxy, attached and electrically connected to a sample holder, and placed in a polarization cell containing the mild acid-chloride electrolyte. Stabilization was allowed to occur for at least one hour, after which E_{corr} was measured. The cyclic polarization curve was then generated at a scan rate of 600 mV/h. The reversing current density was 1000 $\mu A/cm^2$.

RESULTS AND DISCUSSION

The cyclic anodic polarization behaviors of FA-84 (28Al-2Cr) in the as-processed and mechanically-cleaned surface conditions are shown in Figure 2. The as-processed condition, relative to the mechanically-cleaned condition, produced a slightly lower pitting potential (E_{pit}), a lower average passive current density (i_p), and a much higher corrosion potential (E_{corr}). The lower E_{pit} value and the lower (E_{pit} - E_{corr}) value for the as-processed (high-temperature oxide) surface condition both indicated reduced resistance to pitting corrosion.

As seen in Figure 3 for the FA-129 (28Al-5Cr) alloy, the as-processed surface condition performed poorly with respect to both the mechanically-cleaned and chemically-cleaned surface conditions. The as-processed surface condition showed almost no tendency for passivation. For the as-processed surface, the pitting potential was significantly lower, and the corrosion potential higher, than for the other two conditions which involved removal of the high-temperature oxide. Again, the lower E_{pit} value and the lower (E_{pit} - E_{corr}) value for the as-processed surface condition both indicated reduced resistance to pitting corrosion.

As seen in Figure 4 for the FAL-Mo (28Al-5Cr-1Mo) alloy, the pitting potential, E_{pit}, for the as-processed surface condition was significantly lower than E_{pit} values for the mechanically-cleaned and chemically-cleaned surfaces. Also, the range of the passive current density, i_p, was rather small for the as-processed surface condition. It also is noted that the high-temperature oxide on the as-processed surface did not produce a stable i_p, i.e., current-density fluctuations

were obvious. The mechanically and chemically cleaned conditions each had certain advantages. The mechanically-cleaned surface had a slightly higher E_{pit} and a lower E_{corr}. However, the chemically cleaned surface had a significantly lower i_p. The lower i_p suggested that there was either a thickening of the passive film or possibly a Cr enrichment of the passive film caused by the chemical cleaning process.

The cyclic anodic polarization behaviors of the disordered alloy, FAPY (16Al-5Cr-1Mo), in the as-processed and mechanically-cleaned surface conditions are shown in Figure 5. Once again, the as-processed surface performed poorly in comparison to the mechanically-cleaned surface. The as-processed surface condition produced a much lower E_{pit}, with little indication of a passive current density, i_p, and a much higher E_{corr} value.

As seen in Figure 6 for the FeAl-based iron aluminide, FA-385 (36Al-0.2Mo), the heat-treated high-temperature-oxide surface condition produced a much lower E_{pit}, a much lower i_p, and a higher E_{corr} value than the mechanically-cleaned surface condition. The lower E_{pit} value and the lower (E_{pit} - E_{corr}) value for the high-temperature-oxide surface condition both indicated reduced resistance to pitting corrosion.

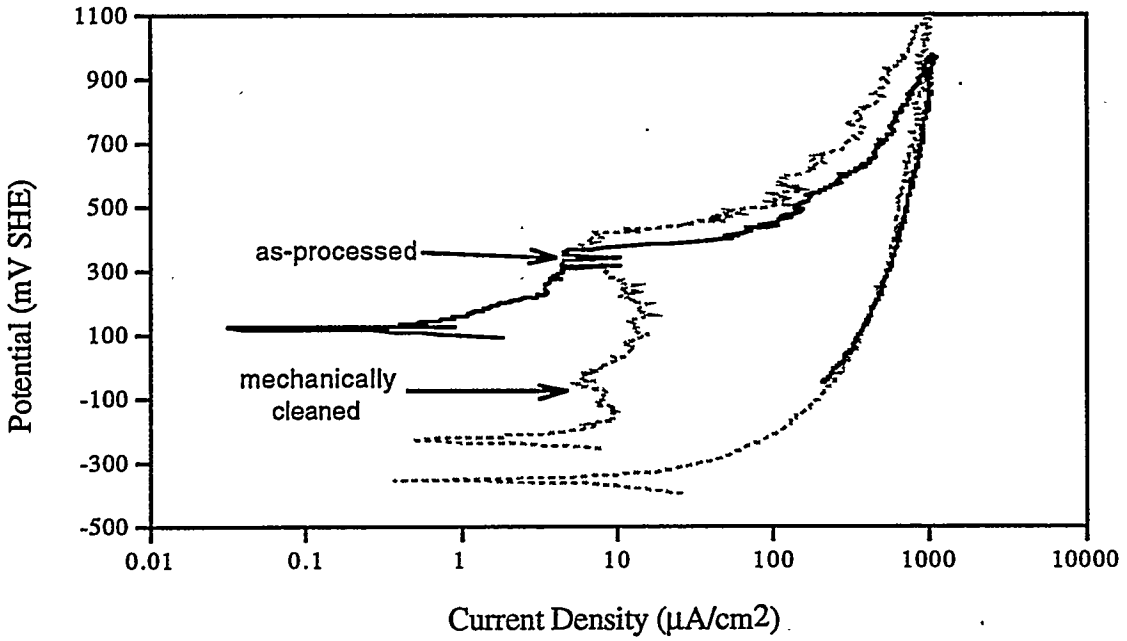

Fig. 2. Cyclic anodic polarization behaviors of FA-84 with as-processed and mechanically-cleaned surfaces.

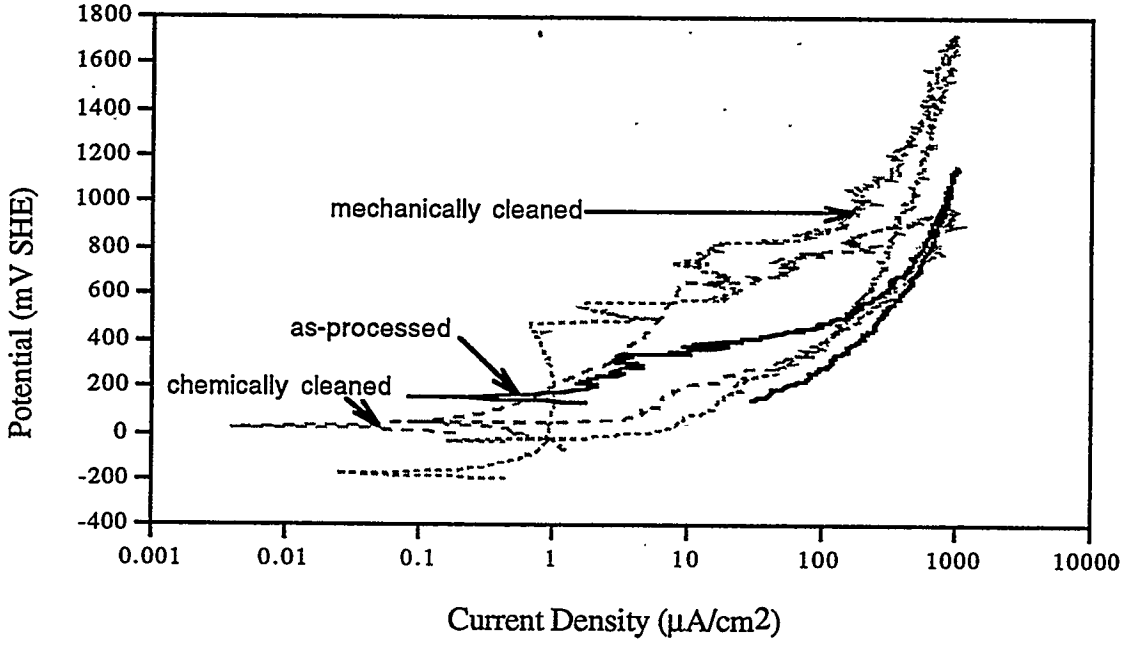

Fig 3. Cyclic anodic polarization behaviors of FA-129 with as-processed, mechanically-cleaned, and chemically-cleaned surfaces.

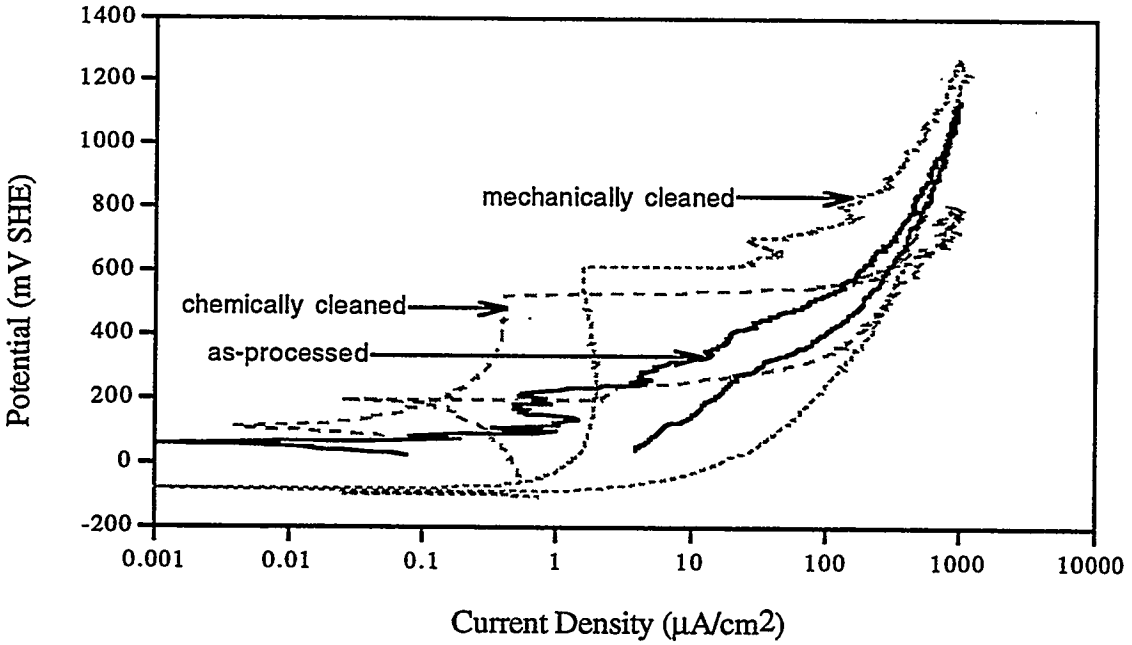

Fig 4. Cyclic anodic polarization behaviors of FAL-Mo with as-processed, mechanically-cleaned, and chemically-cleaned surfaces.

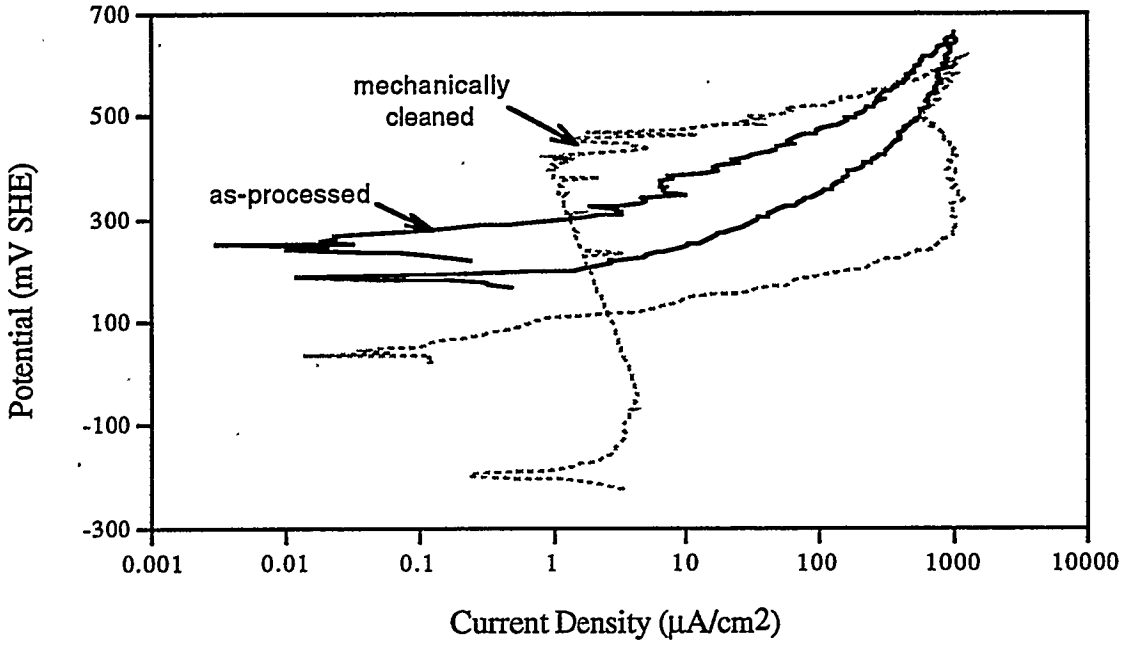

Fig 5. Cyclic anodic polarization behaviors of FAPY with as-processed and mechanically-cleaned surfaces.

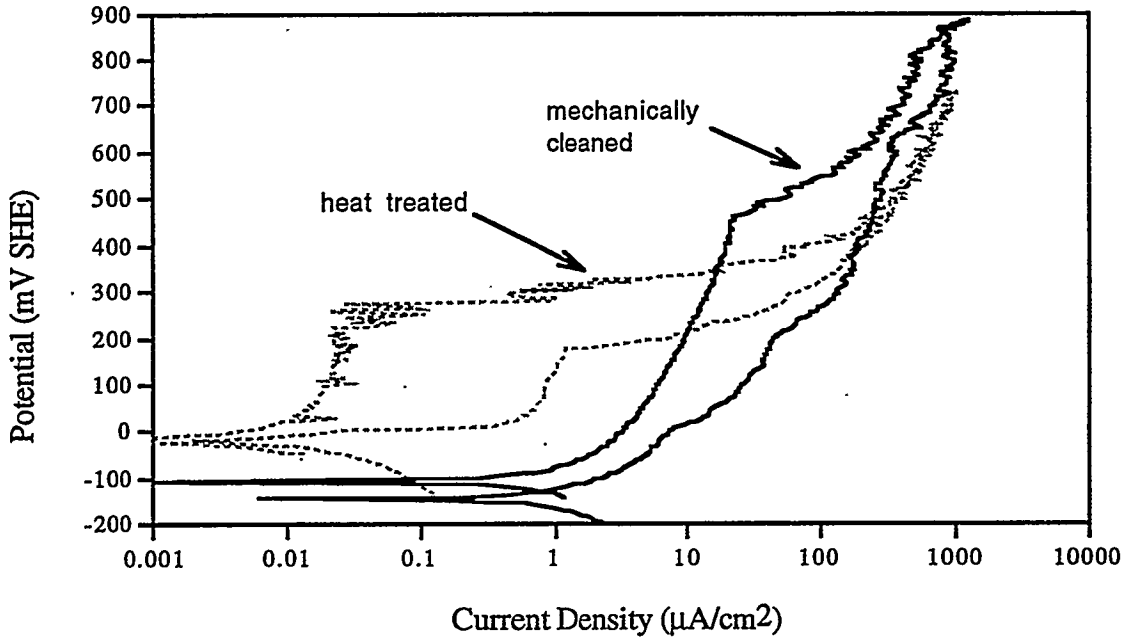

Fig 6. Cyclic anodic polarization behaviors of FA-385 with heat-treated and mechanically-cleaned surfaces.

To provide comparisons of selected results for all materials and surface conditions evaluated, bar graphs of critical pitting potentials, E_{pit}, and the difference between critical pitting and corrosion potentials, (E_{pit} - E_{corr}), are shown in Figures 7 and 8, respectively. It is apparent for all materials that both E_{pit} and (E_{pit} - E_{corr}) were significantly lower for the high-temperature-oxide surfaces, indicating significantly reduced resistance to localized corrosion for these surfaces.

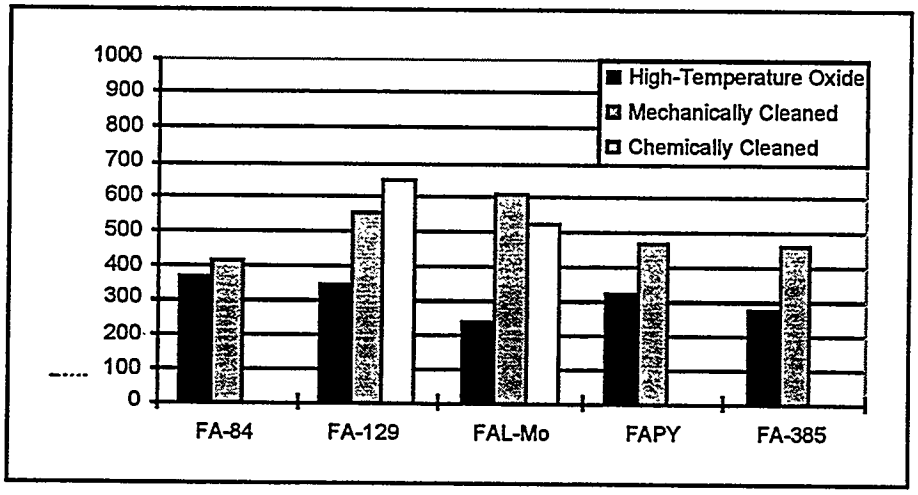

Fig. 7. Critical pitting potential versus material and surface condition.

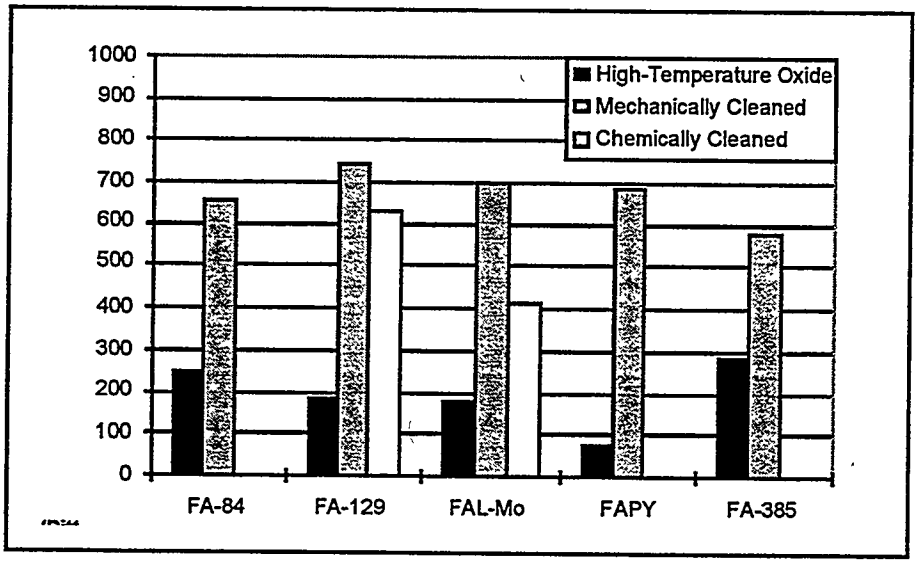

Fig. 8. Difference between pitting and corrosion potentials versus material and surface condition.

Another observation that did not manifest itself directly in the polarization behavior was the appearance of the surfaces of the samples after chemical cleaning. The high-temperature-oxide surfaces of FA-84 and FA-129 were cleaned rather easily in the 10% HNO_3, 2% HF solution but also could be cleaned in a solution containing only 10% HNO_3. However, the oxide surfaces of FAL-Mo and FAPY were slow to clean in the 10% HNO_3, 2% HF solution, and could not be cleaned at all in the 10% HNO_3 solution. Furthermore, after chemical cleaning, the FA-129 and FA-84 samples had shiny smooth surfaces, whereas the FAL-Mo and FAPY samples had shiny rough surfaces. For the FAL-Mo and FAPY samples, the attack of the 10% HNO_3, 2% HF solution was more prominent in areas of exposed base material, i.e., cut faces or where the oxide had flaked off. The difficulties experienced in removal of the high-temperature oxides apparently can be attributed to the presence of Mo in the FAL-Mo and FAPY alloys, which is also partly responsible for the greater aqueous-corrosion resistance exhibited by these alloys.

CONCLUSIONS

Electrochemical aqueous-corrosion studies showed that retained high-temperature surface oxides on iron aluminides (FA-84, FA-129, FAL-Mo, and FA-385) and a related alloy (FAPY), produced during thermomechanical and/or heat treatment processing, caused major reductions in corrosion resistance in an electrolyte designed to simulate aggressive atmospheric corrosion. Removal of the oxides by mechanical grinding, or, more practically, by chemical cleaning restored the corrosion resistance. A standard picking solution employed for stainless steels, nitric plus hydrofluoric acid, worked well for the iron aluminides not containing Mo (FA-84 and FA-129), producing a clean, smooth surface. However, for the Mo-containing materials (FAL-Mo and FAPY), although this solution was effective in removing the oxide, it produced an unacceptably rough surface. Improved chemical cleaning procedures are currently being investigated.

REFERENCES

1. R. A. Buchanan and J. G. Kim, "Fe_3Al-Type Iron Aluminides: Aqueous Corrosion Properties in a Range of Electrolytes and Slow-Strain-Rate Ductilites During Aqueous Corrosion," Final Report, U. S. Dept. of Energy, Fossil Energy AR & TD Materials Program, ORNL/Sub/88-07685CT92/02, National Technical Information Service, Springfield, VA, August, 1992.

2. J. G. Kim and R. A. Buchanan, "Aqueous Corrosion Properties and Slow-Strain-Rate Ductilities of Fe_3Al-Based and Lean-Aluminum Iron Aluminides," Final Report, U. S. Dept.

of Energy, Fossil Energy AR & TD Materials Program, ORNL/Sub/88-07685CT92/03, National Technical Information Service, Springfield, VA, August, 1993.

3. J. G. Kim and R. A. Buchanan, "Pitting and Crevice Corrosion of Iron Aluminides in a Mild Acid-Chloride Solution," Corrosion, Vol. 50, No. 9, pp. 658-668, Sept., 1994.

4. J. G. Kim and R. A. Buchanan, "Localized Corrosion and Stress Corrosion Cracking Characteristics of a Low-Aluminum-Content Iron Aluminum Alloy," Final Report, U. S. Dept. of Energy, Fossil Energy AR & TD Materials Program, ORNL/Sub/88-07685CT92/04, National Technical Information Service, Springfield, VA, October, 1994.